

Peculiar Features in the Cosmic Microwave Background Radiation

Patrick Dineen

Thesis submitted to the University of Nottingham
for the degree of Doctor of Philosophy, May 2005

At times one remains faithful to a cause only because its opponents do not cease to be insipid.

— Friedrich Nietzsche

Supervisor: Prof. Peter Coles

Examiners: Prof. Ed Copeland
Dr. Pedro Ferreira

Contents

Abstract	4
1 Standard framework	5
1.1 Big bang models	5
1.2 The cosmic microwave background	10
2 Characterizing early Universe fluctuations	15
2.1 Density fluctuations	15
2.2 CMB temperature fluctuations	18
2.3 Fluctuations on a sphere: the spherical harmonics	22
2.3.1 Correlated l -modes	23
2.3.2 Correlated m -modes	25
2.3.3 Correlations in inverted images	27
3 Non-Gaussian fluctuations in the CMB	28
3.1 Introduction	28
3.2 Testing for phase correlations	29
3.2.1 Kuiper's statistic	29
3.2.2 Rotation of coordinate system	30
3.2.3 Implementation	34
3.3 Application to sky maps	35
3.3.1 Toy models	35
3.3.2 Quadratic non-Gaussian maps	38
3.3.3 COBE-DMR data	40
3.3.4 WMAP 1-yr data	41

3.4	Conclusions	46
4	Non-random phases in non-trivial topologies	49
4.1	Introduction	49
4.2	Non-trivial topology	50
4.3	Testing for phase correlations	52
4.4	Results and discussion	54
4.5	Conclusions	59
5	Foreground contamination in CMB maps	60
5.1	Introduction	60
5.2	Faraday rotation and foregrounds	62
5.3	Distribution of rotation measures	64
5.4	Correlating rotation measures with sky maps	67
5.5	Application to sky maps	68
5.5.1	Foreground maps	68
5.5.2	COBE–DMR data	71
5.5.3	WMAP 1-yr data	72
5.6	Discussion and conclusions	75
6	Faraday rotation template	77
6.1	Introduction	77
6.2	Large-scale magnetic fields	79
6.3	Rotation measure catalogues	81
6.4	Generating a new basis	82
6.5	All-sky RM maps and their interpretation	85
6.6	Correlations with CMB maps	90
6.7	Conclusions	92
7	Problems and future extensions	94
	Bibliography	98
	Acknowledgements	109

Abstract

In this thesis, I develop statistics capable of detecting peculiar features in current observations of the cosmic microwave background (CMB) radiation. Such tools scrutinise the very foundations of standard cosmological models. Evidence of peculiar features in the CMB may require a reassessment of these building blocks. More likely, any features may be artefacts of some non-cosmological signal. Nevertheless, whether the origin of these strange attributes is primordial or local, their discovery would be instructive. Existing statistical tools focus on the amplitude of the spherical harmonic coefficients, I look instead at their phases. The method I form checks for the uniformity of the distribution of phase angles using a non-parametric descriptor, which is known as Kuiper's statistic. The method is applied to the COBE-DMR and WMAP sky maps, and departures from uniformity are found in both. The results probably reflect Galactic contamination or the known variation of signal-to-noise across the sky rather than primordial non-Gaussianity. Next, the statistic is adjusted to probe the topology of the universe. The new method exploits the existence of correlations in the phases of the CMB temperature pattern associated with matched pairs of circles seen in the CMB in universes with non-trivial topologies. After this, I turn our attention to the issue of Galactic foreground signals. A diagnostic of foreground contamination is developed based around the Faraday rotation measures (RM) of extragalactic sources. Statistically significant correlations of RM with the preliminary WMAP individual frequency maps are found. These correlations remain significant in CMB-only maps. Later, I use catalogues of rotation measures to construct a template of the Galactic sky. The RM maps may be used as templates for CMB foreground analysis. This idea is illustrated with a cross-correlation analysis between the WMAP data and our maps. I find a significant cross-correlation, again indicating the presence of significant residual contamination. Problems and future developments are discussed at the end.

Chapter 1

Standard framework

1.1 Big bang models

We are entering an era of “precision cosmology” in which our basic models of the universe are being refined. Our picture of the universe has evolved remarkably over the past century; from a view limited to our Galaxy to a cosmos with billions of similar structures. Today, cosmology appears to be concerned with improving estimates of parameters that describe our cosmological models rather than searching for alternatives. Recent observations of the large scale structure (eg. 2dFGRS; Percival *et al.*, 2001) and the Wilkinson Microwave Anisotropy Probe (WMAP; Bennett *et al.*, 2003a) observations of the cosmic microwave background (CMB), appear to confirm our key ideas on structure formation. However, there is the suggestion that our confidence may be misplaced. The WMAP observations, for example, have thrown up a number of unusual features (Chiang *et al.*, 2003; Efstathiou, 2003; Naselsky, Doroshkevich & Verkhodanov, 2003; Chiang & Naselsky, 2004; Eriksen *et al.*, 2004b; Land & Magueijo, 2004; McEwen *et al.*, 2004). It appears a good time to stand back from the established paradigm and test the core assumptions intrinsic to our view of the universe.

Standard Big Bang cosmological models are founded upon the Cosmological Principle. This principle states that we live in a universe that is statistically homogeneous and isotropic. Homogeneity implies that the universe appears the same to all observers. An isotropic universe looks the same in all directions. Observations of the CMB indicate

that the latter is the case, however, homogeneity is harder to prove.

Construction of cosmological models requires an understanding of the nature of the forces at the largest scales. The principal force on these scales is gravity and our best description of this force is Einstein's theory of general relativity. General relativity relates the distribution of matter to the geometry of space–time (given by the metric $g_{\mu\nu}$). Therefore, we need a metric that adheres to the cosmological principle. All homogeneous and isotropic space–times can be described in terms of the Robertson–Walker metric

$$ds^2 = g_{\mu\nu} dx^\mu dx^\nu = c^2 dt^2 - a^2(t) \left[\frac{dr^2}{1 - \kappa r^2} + r^2(d\theta^2 + \sin^2 \theta d\phi^2) \right], \quad (1.1)$$

where r , θ and ϕ are the spherical polar coordinates, t is the proper time, $a(t)$ is the cosmic scale factor, and κ is the spatial curvature scaled to take the values 0 or ± 1 . The proper time t is simply a measure of time calculated from the local density of an observer that is the same for all observers due to the homogeneity of the universe. The scale factor $a(t)$ describes the overall expansion or contraction of the universe.

The dynamics of the universe can then be determined by Einstein's field equations which relate the geometrical properties of the space–time, via the metric tensor $g_{\mu\nu}$, to the contents of the universe summarised in the energy–momentum tensor $T_{\mu\nu}$. The equations are written as

$$R_{\mu\nu} - \frac{1}{2}g_{\mu\nu}R = \frac{8\pi G}{c^4}T_{\mu\nu}, \quad (1.2)$$

where $R_{\mu\nu}$ and R are the Ricci tensor and the Ricci scalar, respectively. G is Newton's gravitational constant. For a perfect fluid, with pressure p and energy density ρc^2 , the energy–momentum tensor is

$$T_{\mu\nu} = (p + \rho c^2)U_\mu U_\nu - pg_{\mu\nu}, \quad (1.3)$$

where U_α is the fluid–four velocity. The Robertson–Walker metric requires $T_{\mu\nu}$ to take this form. Einstein's equations can then be simplified assuming the Robertson–Walker metric to

$$3 \left(\frac{\dot{a}}{a} \right)^2 = 8\pi G\rho - \frac{3\kappa c^2}{a^2}, \quad (1.4)$$

$$\frac{\ddot{a}}{a} = -\frac{4\pi G}{3} \left(\rho + 3\frac{p}{c^2} \right), \quad (1.5)$$

and

$$\frac{d}{dt}(\rho a^3) + \frac{p}{c^2} \frac{d}{dt}(a^3) = 0. \quad (1.6)$$

Equation (1.6) is not independent of the other two equations. These three equations are collectively known as the Friedman equations. The Friedman equations can be calculated from Newtonian arguments, which at first sounds surprising, however Einstein's equations are designed to reduce to Newton's law when the gravitational field is weak. The Friedman equations will allow us to construct cosmological models if the contents of the universe can be assumed to be an ideal fluid. This is quite a realistic approximation as long as the mean free path of any collision is much less than scales of importance. Now, all we need to specify is the equation of state for our fluid ($p = wpc^2$).

To get an insight into the significance of the Friedman equations, we shall look at two scenarios: the matter-only and radiation-only universes (with $\kappa = 0$). In the matter case we set $w=0$ as the rest mass of each particle is much larger than the particle's thermal energy and so the pressure is zero. Therefore, Equation (1.6) implies $\rho \propto a^{-3}$. Substituting this into Equation (1.4) leads to $a \propto t^{2/3}$. On the other hand, radiation or relativistic particles have a value of $w=1/3$ and consequently we find $\rho \propto a^{-4}$ and $a \propto t^{1/2}$. Our universe contains both matter and radiation, however, this illustrates the basis of more complex models. So far, we have neglected the cosmological constant Λ which can be incorporated into Einstein's equations. Λ has acquired renewed interest due to inflationary models (see later) and the results from distant Type Ia supernovae that suggest a non-zero value of Λ (Perlmutter *et al.*, 1999; Knop *et al.*, 2003).

There are a number of key cosmological parameters that determine the long-term history of the universe. Firstly, there is the Hubble parameter $H(t)$. In 1929, Hubble observed that all galaxies are receding from us by an amount related linearly to the distance the galaxies are away from us. This concept is enshrined in Hubble's law as

$$v = Hr = \left(\frac{\dot{a}}{a} \right) r, \quad (1.7)$$

where v is the velocity of the galaxy and r is the proper distance to the galaxy. Homogeneous and isotropic expansion naturally reproduce Hubble's law.

The expansion of the universe allows us to introduce a useful measure of the distance to an object. The redshift z is defined as the shift in frequency ν of spectral lines towards the red end of the spectrum due to the recession of a source resulting from the expansion of the universe. This can be understood by looking at the Robertson–Walker

metric. The interval ds travelled by a photon is always zero. From this, we can derive

$$\frac{dt_o}{dt_e} = \frac{\nu_e}{\nu_o} = 1 + z, \quad (1.8)$$

where the subscripts e and o indicate the emitted and observed radiation, and z is the redshift of the source. The redshift of an object can be obtained without assumptions about the underlying cosmology. Importantly, we can relate z to the cosmic scale factor using Equation (1.8) to get

$$1 + z = \frac{a_o}{a}, \quad (1.9)$$

and therefore we can use z as a distance measure.

The second key parameter is the density parameter which is defined as

$$\Omega_x = \frac{8\pi G \rho_x}{3H^2} = \frac{\rho_x}{\rho_{\text{crit}}}, \quad (1.10)$$

where x signifies a constituent of the universe (matter, radiation or Λ). The density parameter is the ratio of the actual density to some critical value ρ_{crit} . The sum of these components is labelled Ω_{tot} . If $\Omega_{\text{tot}}=1$, we have a flat universe with $\kappa=0$ that continues to expand. This scenario is favoured by inflationary models. $\Omega_{\text{tot}} > 1$ corresponds to $\kappa=1$ and results in a 'Big Crunch' where the universe recollapses. $\Omega_{\text{tot}} < 1$ corresponds to $\kappa=-1$ and a continual expansion.

The deceleration parameter is defined as

$$q = -\frac{\ddot{a}a}{\dot{a}^2}. \quad (1.11)$$

The parameter measures the rate at which the expansion of the universe is slowing down and will be positive if gravity is the sole force acting on large scales.

The key parameters mentioned govern the dynamics of the universe. It is one of the major aims of observational cosmology to precisely pin down these numbers. The key project of the Hubble Space Telescope (HST) was to calculate the present-day value of the Hubble parameter using secondary indicators (supernovae, Tully–Fisher, and surface brightness fluctuations). The value of the parameter was found to be $H(t_o) = 72 \pm 8 \text{ km s}^{-1} \text{Mpc}^{-1}$ (Freedman *et al.*, 2001). The deceleration parameter has been constrained using high-redshift Type Ia supernovae. The light curves from these remnants are important cosmological probes. The data provide strong evidence for an accelerating universe ($q < 0$) and is inconsistent with a $\Omega_\Lambda = 0$ flat universe

(Perlmutter *et al.*, 1999). In fact, the data suggests a value of $\Omega_\Lambda \sim 0.7$. The CMB has the potential to thoroughly determine these parameters. The 1st year results from the WMAP satellite, by itself, gives a value for the matter density of $\Omega_m h^2 = 0.12 \pm 0.02$ and for the density of baryons of $\Omega_b h^2 = 0.024 \pm 0.001$ (Spergel *et al.*, 2003), where h is $H(t_o)/100$. When the WMAP data is combined with other small scale CMB measurements, the matter power-spectrum from large-scale structure surveys and the Lyman- α forest, we obtain values of $\Omega_m h^2 = 0.133 \pm 0.006$ and $\Omega_b h^2 = 0.0226 \pm 0.0008$ (Spergel *et al.*, 2003). Finally, combining the WMAP data with either the HST results, large-scale structure surveys or Type Ia supernovae results implies $\Omega_{\text{tot}} = 1.02 \pm 0.02$ (Bennett *et al.*, 2003a). Consequently, we have an image of our universe which is flat and composed of $\Omega_m = 0.3$ and $\Omega_\Lambda = 0.7$; this is dubbed the *concordance model*.

In the concordance model, we find that 30% of the universe is composed of matter yet only 10% is of a baryonic form. Is our estimate of Ω_b wrong? The primordial deuterium abundance is sensitive to the baryon density and measurements confirm the CMB results with $\Omega_b h^2 = 0.020 \pm 0.002$ (Burles, Nollett & Turner, 2001). Galaxy rotation curves also suggest the presence of substantial halos of non-luminous material surrounding galaxies. This missing matter is labelled dark matter. The current favoured explanation is massive particles with low thermal velocities produced in the big bang. These cold dark matter (CDM) particles do not participate in nuclear reactions and interact purely through gravity.

This picture allows us to develop a history of the very early universe. Naturally, we expect the universe to be hotter and denser in the past. In this fireball phase, we expect a series of creation-annihilation reactions between particles to govern until

$$k_B T \sim m_p c^2, \quad (1.12)$$

where k_B is the Boltzmann constant and m_p is the mass of the particle. As long as the temperature is higher than this, two photons will create a particle-antiparticle pair. However, when the temperature drops below, the pairs can no longer be created and the pairs rapidly annihilate. The high temperatures in the past will also lead to the unification of the fundamental forces. Importantly for this thesis, as the universe cools we expect there to be a period where there is a plasma of baryons and photons in thermal equilibrium. As the universe cools, the matter becomes transparent to radiation; this topic is the expanded upon in Section 1.2. The relic radiation is a powerful signature of the big bang model.

The big bang model accounts for three important cosmological observations: the expansion of the universe; the existence of a relic radiation background; and the abundances of light atomic nuclei which were created in the first few minutes of the big bang. However, the big bang model is not a complete theory; it does not specify the values of the key parameters or describe the era before planck-time. Moreover, cosmologists are left with a number unexplained features: the origin of the baryon asymmetry; the nature of dark matter; the flatness of the universe; the 'excessive' degree of homogeneity and isotropy (the horizon problem); missing relic particles; and the origin of the primordial density perturbations. The final four of these issues have been potentially overcome by the addition of a new idea by Guth (1981) called inflation. Inflationary models involve the early universe going through a period of accelerated expansion. The time of this expansion is chosen to maintain the successes of the big bang model, that is to say, nucleosynthesis occurs after the inflationary period. Inflation permits a solution to the horizon problem because a uniform region that appear to be unable to have been in causal contact in the past would have been thermalised before inflation. Today, we know the universe is very flat ($\Omega_{\text{tot}} \sim 1$), but the universe had been flatter still in the past. The inflationary phase leaves the universe in such a state. Also, as long as inflation happens after the phase transitions producing the defects, these relic particles will be diluted by the increase in the scale factor during inflation. Potentially the most significant aspect of inflation is that it allows a possible solution to the origin of the structure we see today. During the inflationary period, quantum fluctuations on microscopic scales will lead to present-day large scale fluctuations due to the accelerated expansion. Generically, inflationary models predict a Harrison–Zel'dovich spectrum (i.e. a scale invariant spectrum) of fluctuations. These primordial fluctuations are expected to constitute a Gaussian random field. This class of field is discussed in chapters 2 and 3. Clearly, if inflation is the real solution then we need to test these predictions. In chapter 3, we hopefully fulfil this commitment by proposing a statistical test to probe the nature of the primordial field.

1.2 The cosmic microwave background

Our present understanding is that the universe began roughly 15 billion years ago as a hot, dense environment with a nearly uniform sea of radiation. The baryons were in

a plasma form until 300,000 years after the Big Bang ($z \sim 1100$). At this point, the universe had cooled sufficiently for protons to capture free-electrons and form neutral hydrogen. Prior to this, due to the high temperature, matter is completely ionised. Compton scattering couples the photons to the electrons and the electron are coupled to baryons by electromagnetic interactions. As the protons recombine with electrons, at 3,000 K, the universe becomes transparent. The radiation is said to decouple, and freely propagates through the universe until reaching us. Before decoupling, the radiation and matter are in thermal equilibrium and the lack of interactions thereafter results in the radiation having a black-body spectrum. The temperature of the radiation drops according to $T = (1 + z)T_0$ due to the expansion of the universe. Consequently, the present day temperature of this relic radiation is roughly 2.7 K and should be observable in the microwave region of the sky. The radiation should be uniform in all directions of the sky and originate from the last-scattering-surface.

The relic radiation, which we refer to as the CMB, was probably first predicted to exist by Gamow (1948). The CMB's discovery by Penzias & Wilson (1965) was one of the successes of hot big bang models. The temperature of the CMB was measured by the COBE–FIRAS instrument as 2.728 ± 0.004 K (Fixsen *et al.*, 1996) and found to have a perfect black-body spectrum. Equally importantly, in 1992 the first primordial temperature fluctuations were detected by the COBE–DMR instrument (Smoot *et al.*, 1992). These fluctuation have been sought since the discovery of the CMB. The temperature anisotropies are translations of the primordial matter fluctuations. Crucially, the temperature anisotropies are small $\mathcal{O}(10^{-5})$ due to radiation pressure and have evolved linearly. Therefore, we can easily trace the temperature anisotropies back to their primordial form unlike the case for the matter distribution. We shall now summarise the main sources of the temperature anisotropies; for a detailed review see Hu & Dodelson (2002). The anisotropies can be categorised according to their source. Primary anisotropies are generated at, or prior, to decoupling. Secondary anisotropies are imprinted on the CMB photons as they traverse from the last-scattering-surface to our observatories. All the anisotropies are characterized by the power they induce at particular scales which is usually illustrated by the angular power spectrum.

The dominant observed anisotropy is the kinetic dipole arising from the Doppler shift of the photon due to the motion of the emitter and observer. This dipole is much larger than the other CMB anisotropies and was first measured by Smoot, Gorenstein

& Muller (1977). The dipole principally reflects the motion of the Local Group of galaxies.

The primary anisotropies that dominate at large scales (super-horizon sizes) are caused by the Sachs–Wolfe effect (Sachs & Wolfe, 1967). This effect represents the gravitational redshift of the photon due to the difference in gravitational potential between the location of emission and observation. At these scales, the initial perturbations cannot be effected by causal process and thus these anisotropies are directly related to the initial matter power spectrum. These large scales were first probed by the COBE–DMR instrument.

On intermediate scale ($0.1^\circ < \theta < 2^\circ$) the anisotropies are dominated by the acoustic peaks. These peaks in power are the result of acoustic oscillations of the photon–baryon fluid within the sound horizon. The first acoustic peak corresponds to the scale where the primordial density inhomogeneities are just reaching a maximum amplitude at the surface of last scattering. Further acoustic peaks correspond to scales that are reaching antinodes of oscillation. These peaks encode a wealth of information about the geometry, contents and evolution of the universe both before and after recombination. For example, the positions of these peaks are determined by the geometry of the universe. A physical scale subtends a smaller angle in an open universes ($\kappa = -1$) compared to the Euclidean case ($\kappa = 0$). The peaks are consequently observed at smaller scales for the open case than in the flat case. The amplitude of these acoustic peaks depends on a combination of the baryon fraction, matter density and Hubble parameter. Clearly, accurate measurements of these peaks will help constrain a number of cosmological models. The first peak has been measured by a number of ground based and balloon–borne instruments and recently instruments on board the WMAP satellite measured the first and second peaks (Bennett *et al.*, 2003a).

At small scales the inhomogeneities in the photons are damped due to mechanisms that decrease either the matter or radiation inhomogeneities. Photons defusing out of overdense regions drag baryons and thus lead to damping (Silk, 1968). Free–streaming of collisionless particles (such as neutrinos) from high to low density regions will also cause damping. On top of this, small scales are damped because decoupling is not instantaneous and therefore the last–scattering–surface has a finite thickness. Nevertheless, these processes are again sensitive to cosmological parameters making measurements of these scales worthwhile.

Secondary anisotropies reveal details of the evolution of the universe after decoupling. They can be categorised into gravitational or rescattering effects. In the former case we have examples such as the Integrated Sachs Wolf Effect (ISW). If a photon falls into a potential well which varies temporally, then the photon's energy will be shifted when it climbs out of the well. On the other hand, gravity can deflect the path of the photon without adjusting its energy (i.e. gravitational lensing). The second category relates to the reionisation of the universe. When the universe reionises, free-electrons are produced that will scatter the photons and potentially wash out the primary anisotropies. An important example of this is the thermal Sunyaev–Zel'dovich (SZ) effect (Sunyaev & Zeldovich, 1970). Photons are scattered by hot electrons in the intracluster gas of clusters of galaxies, producing distortions in the black–body spectrum of the CMB.

So far we have only mentioned the (scalar) CMB temperature field. However, the CMB is polarised and the (vector) polarisation field potentially harbours more information. In CMB measurements, two scalar fields, E and B , are used to describe the polarisation field. The polarisation field directly probes the time of last–scattering. At last–scattering, if the radiation field has a local quadrupole then the scattering of photons off electrons will result in linearly polarised radiation. The polarisation fraction is small because only those photons that last–scatter in an optically thin region possess a local quadrupole. The standard assumption is that the polarisation signal is 10% of the level of the temperature anisotropies i.e. $\mathcal{O}(10^{-6})$. Consequently, it is a significant experimental challenge to measure this signal, nevertheless, measurements were recently achieved by the DASI experiment (Kovac *et al.*, 2002). The power spectrum of the polarisation anisotropies and cross–correlation between the temperature field will lead to a sharpening of cosmological constraints. The most dramatic results lie on the largest angular scales where the field probes primordial gravitational waves and the reionization epoch (de Oliveira-Costa, 2004). For comprehensive reviews of CMB polarisation see Hu & White (1997) and Kosowsky (1999).

Evidently, the CMB is an impressive tool for exploring models of our universe. It is our most distant and cleanest probe of the early universe. Yet it also yields information on the nearby universe. Through CMB observations, cosmological parameters can be determined and models ruled out. Equally, the very foundations of these models can be scrutinised. Evidence of peculiar features in the CMB may require a reassessment of these building blocks. More likely, peculiar features may be artefacts of some

non-cosmological signal. Nevertheless, whether the origin of these strange attributes is primordial or local, their discovery would be instructive. In this thesis, I develop statistics to detect unusual characteristics in current CMB observations. In chapters 2 and 3, I establish a statistic that seeks signs of non-Gaussianity in the temperature field. The method is based on the phases of the spherical harmonic coefficients. In chapter 4, the statistic is adjusted to probe the connectivity of the universe. I turn our attention to foreground contamination in the chapters 5 and 6. I develop a diagnostic of foreground contamination in chapter 5 based around the Faraday rotation of light from extragalactic sources. In chapter 6, these rotation measures are used to construct a template of the Galactic sky. Conclusions are drawn at the end of each chapter. Problems and future developments are discussed in chapter 7.

Chapter 2

Characterizing early Universe fluctuations

2.1 Density fluctuations

Today, we observe a rich variety of complex structures in the Universe from filaments to sheets to clusters of galaxies. Standard cosmological models assume these structures grew from small initial perturbations through gravitational instability. The initial perturbations are thought to be seeded during a period of inflation (Guth, 1981; Albrecht & Steinhardt, 1982; Linde, 1982). These primordial perturbations are the result of amplification of zero-point quantum fluctuations to classical scales during the inflationary period (Guth & Pi, 1982; Hawking, 1982; Starobinsky, 1982). In most inflationary scenarios the resultant primordial density field is taken to be a statistically homogeneous and isotropic Gaussian random field (Adler, 1981; Bardeen *et al.*, 1986). Such a field has both physical and mathematical attractions; see later. However, there are alternative possibilities that lead to a field with non-Gaussian statistics. Versions of inflation involving multiple scalar fields or those with non-vacuum initial states lead to a non-Gaussian spectrum. Other potential candidates for seeding the primordial field also lead to non-Gaussian possibilities. Topological defects arise from symmetries being broken as the early Universe cools (like ice forming in rapidly cooling freezing water). The topological defect scenario includes models based on cosmic strings, textures and monopoles (Kibble, 1976; Vilenkin & Shellard, 1994). The development of the de-

fects involves nonlinear physics which leads to a non-Gaussian pattern of fluctuations. Another alternative possibility is the explosion scenario (Ostriker & Cowie, 1981) in which explosions from early massive stars cause shocks that sweep away material and leaves a non-Gaussian distribution of matter.

The density field is usually described in terms of the dimensionless density contrast, $\delta(\mathbf{x})$ which is defined as

$$\delta(\mathbf{x}) = \frac{\rho(\mathbf{x}) - \bar{\rho}}{\bar{\rho}}, \quad (2.1)$$

where $\bar{\rho}$ is the global mean density. Analysis of such a field is aided by an expansion of the density contrast in Fourier series, in which $\delta(\mathbf{x})$ is treated as a superposition of plane waves with amplitudes $\tilde{\delta}(\mathbf{k})$:

$$\delta(\mathbf{x}) = \sum \tilde{\delta}(\mathbf{k}) \exp(i\mathbf{k} \cdot \mathbf{x}). \quad (2.2)$$

The Fourier transform $\tilde{\delta}(\mathbf{k})$ is complex and therefore possesses both an amplitude $|\tilde{\delta}(\mathbf{k})|$ and a phase ϕ_k . If the primordial density field is an homogeneous and isotropic Gaussian random field then the amplitudes are drawn from a Rayleigh distribution and ϕ_k should be uniformly random on the interval $[0, 2\pi]$. The field is fully described by second-order statistics; the two-point correlation function $\xi(r)$ in real space or the power spectrum $P(k)$ in Fourier space. The two-point correlation function is obtained from the variance of the density field

$$\langle \delta(\mathbf{x}_1) \delta(\mathbf{x}_2) \rangle = \xi(|\mathbf{x}_1 - \mathbf{x}_2|) = \xi(r), \quad (2.3)$$

where averages are taken over all spatial positions. Similarly, the covariance of $\tilde{\delta}(\mathbf{k})$ leads to the power spectrum

$$\langle \tilde{\delta}(\mathbf{k}_1) \tilde{\delta}(\mathbf{k}_2) \rangle = P(k) \delta_D(\mathbf{k}_1 + \mathbf{k}_2), \quad (2.4)$$

where δ_D is the Dirac delta function. This basic idea of structure formation has survived numerous observational challenges, to such an extent that many regard the future of cosmology as being largely concerned with refining estimates of parameters of this model rather than searching for alternatives. However, at this point it may be worth stepping back, and testing some of the underlining assumptions: seeking evidence of non-Gaussianity.

Even if the primordial density field is indeed Gaussian, the later stages of gravitational clustering induces nonlinearity. The density fluctuations slowly evolve into non-Gaussian structures such as pancakes and filaments. Finding suitable descriptors that

define the properties and morphology of these evolved structures is an on-going task. Second-order statistics describe only part of the information on the density field. A full hierarchy of higher-order correlation functions in real space or polyspectra in Fourier space are required to fully describe the field (see Peebles, 1980). In an analogous manner to $\xi(r)$, it is possible to define spatial correlation functions for $n > 2$ points. For example, the three-point correlation function $\zeta(r, s, t)$ is defined as

$$\langle \delta(\mathbf{x}_1)\delta(\mathbf{x}_2)\delta(\mathbf{x}_3) \rangle = \zeta(r, s, t), \quad (2.5)$$

where the mean is taken over all points defining the triangle with sides r , s and t . The generalisation of Equation (2.5) to $n > 3$ is trivial. Fourier transforms of the n -point correlation functions are referred to as polyspectra. The equivalent of the 3-point correlation function is the bispectrum B , where

$$\langle \tilde{\delta}(\mathbf{k}_1)\tilde{\delta}(\mathbf{k}_2)\tilde{\delta}(\mathbf{k}_3) \rangle = B(\mathbf{k}_1, \mathbf{k}_2, \mathbf{k}_3)\delta_D(\mathbf{k}_1 + \mathbf{k}_2 + \mathbf{k}_3). \quad (2.6)$$

Work has focused on the three-point correlation function and bispectrum, however, the use of higher order statistics is usually impractical. Hence, alternative statistics that contain some information on the higher order statistics have been sought. Complementary statistics include the void probability function (White, 1979), the genus statistic (Gott, Dickinson & Melott, 1986) and other Minkowski functionals (Mecke, Buchert & Wagner, 1994), percolation analysis (Dekel & West, 1985) and phase analysis (eg. Ryden & Gramann, 1991). It is in this last area that we shall later focus with regard to CMB anisotropies.

The phases of the Fourier components contain crucial information on the spatial pattern of the density fluctuations. The nonlinearity associated with the growth of structure generates non-random phases. In the early stages of structure formation, the situation can be compared to linear waves on the surface of deep water. Like these waves, the Fourier components of the density field evolve independently and the phases are random. However, as the structures grow, the situation is more analogous to breaking waves in shallow water. The components interact in nonlinear ways; mode-mode interactions lead to coupled phases. The question is, how does this phase coupling manifest itself?

Developing useful statistics from the behaviour of phases in gravitational systems has been a challenging task. The problem has been demanding due to the phases being

circular measures. Sugino & Suto (1991) examined the one-point phase distribution in nonlinear density fields. The distribution was found to be uniform in even the most extreme cases of non-Gaussianity. Therefore, early attempts to exploit the information encoded in the phases focused on the evolution of the individual phases (Ryden & Gramann, 1991; Soda & Suto, 1992; Jain & Bertschinger, 1996, 1998). This was done through a mixture of numerical simulations and perturbation theory. Scherrer, Melott & Shandarin (1991) were the first to examine the relationship between the phases of different Fourier modes. The authors presented a quantitative measure of phase correlations based on the locations of the maxima of the Fourier components. Other authors have since connected phase correlations with clustering dynamics and morphology (Chiang & Coles, 2000; Chiang, 2001; Chiang, Coles & Naselsky, 2002; Watts, Coles & Melott, 2003). In Coles & Chiang (2000), a technique was presented that enabled the phase information to be visualised using colour coding. The technique allowed readers to see how phase coupling evolved with the growth of structure. Besides this, the relationships between phase correlations and more traditional measures of non-Gaussianity (Matsubara, 2003; Watts & Coles, 2003; Hikage, Matsubara & Suto, 2004), such as the bispectrum, have been sought. For example, Matsubara (2003) found a relation between the distribution of a specific form of associated phases and the hierarchy of polyspectra in perturbation theory.

2.2 CMB temperature fluctuations

The development of statistics that seek and quantify non-Gaussianity in cosmology is not restricted to density field studies. Non-Gaussian signals are sought in CMB anisotropies, gravitational lensing, and a number of other cosmic field studies. In this thesis, we shall later explore the issue of non-Gaussianity in the CMB. It should be noted that the question of non-Gaussianity in the CMB is intertwined with the same question concerning the initial density perturbations. The inhomogeneity in the matter distribution is translated to the background radiation photons through Thomson scattering. After last scattering the majority of these photons arrive at our observatories unperturbed. If the primordial matter distribution is Gaussian then so too is the primary temperature pattern. Thus, the CMB anisotropies provides us with a clean tool to discriminate between initial field models described in the previous section. However, be-

fore we can test this assumption we need to ensure we are looking at the last-scattering surface. Most secondary anisotropies are nonlinear in nature and hence lead to non-Gaussian signals. Lensing and the Sunyaev–Zel’dovich effect should both be able to be isolated through their non-Gaussian effects. Moreover, Galactic foregrounds and experimental systematic errors will leave non-Gaussian imprints in the CMB measurements. Thus, the development of non-Gaussian statistics that can isolate these effects is imperative. The demand for such tracers will only intensify: increased sensitivity and polarisation measurements will require better control of secondary effects and foregrounds.

The temperature fluctuations in the the CMB at any point in the celestial sphere can be expressed in spherical harmonics as

$$\Delta(\theta, \phi) = \frac{(T(\theta, \phi) - \bar{T})}{\bar{T}} = \sum_{l=1}^{\infty} \sum_{m=-l}^{m=+l} a_{l,m} Y_{l,m}(\theta, \phi), \quad (2.7)$$

where the $a_{l,m}$ can be written

$$a_{l,m} = |a_{l,m}| \exp[i\phi_{l,m}]. \quad (2.8)$$

The $a_{l,m}$ are complex and are characterized by two numbers l and m . These take the values $l=0, 1, 2, \dots$ and $m=l, l-1, l-2, \dots, -l+2, -l+1, -l$. Therefore, for every given l there are $(2l+1)$ values of m and hence the same number of $\phi_{l,m}$. The spherical harmonics are orthonormal on a complete sphere. However, not all the coefficients are independent for different values of m . The following relationship are seen in a set of $a_{l,m}$:

1. If $m = 0$, then $\Im(a_{l,m}) = 0$.
2. If m is odd, then $\Re(a_{l,m}) = -\Re(a_{l,-m})$ and $\Im(a_{l,m}) = \Im(a_{l,-m})$.
3. If m is even, then $\Re(a_{l,m}) = \Re(a_{l,-m})$ and $\Im(a_{l,m}) = -\Im(a_{l,-m})$.

Therefore, when studying the phases of an image or anything else, these relationships have to be taken into account.

In orthodox cosmologies the primary temperature fluctuations constitute a statistically homogeneous and isotropic Gaussian random field. If true, then all the statistical information from the last-scattering surface is encoded in the angular power spectrum C_l . The angular power spectrum is constructed in a similar fashion to the power spectrum

in Fourier space, that is to say

$$\langle a_{l',m'}^* a_{l,m} \rangle = C_l \delta_{l,l'} \delta_{m,m'}. \quad (2.9)$$

The phases $\phi_{l,m}$ of a Gaussian random field should be uniformly random on the interval $[0, 2\pi]$. A large number of methods to test this belief have been proposed in the literature. The skewness and the kurtosis of the temperature field have been studied (Luo & Schramm, 1993a). Gaussianity dictates that all odd n -point correlation functions are zero and all even n -point correlation functions can be related to the 2-point correlation function. The 3-point correlation function (Luo & Schramm, 1993b; Kogut *et al.*, 1996) and its harmonic analogue, the bispectrum (Luo, 1994; Heavens, 1998; Ferreira, Magueijo & Gorski, 1998), have both been studied extensively. Statistical tests have been developed to explain properties of excursion sets, these include the topology of the temperature contours (Coles, 1988; Gott *et al.*, 1990; Kogut *et al.*, 1996), Minkowski functionals (Schmalzing & Gorski, 1998; Winitzki & Kosowsky, 1998) and peak statistics (Bond & Efstathiou, 1987; Vittorio & Juszkiewicz, 1987; Kogut *et al.*, 1996). Estimators based on Fourier statistics have been proposed (Ferreira & Magueijo, 1997a; Lewin, Albrecht & Magueijo, 1999). Also, statistics have been developed based on wavelet techniques (Pando, Valls-Gabaud & Fang, 1998; Aghanim & Forni, 1999; Hobson, Jones & Lasenby, 1999). We shall investigate the phases of the spherical harmonic coefficients where presently the literature is rather sparse.

The phases of the $a_{l,m}$ contain crucial information that determines the morphology of a spherical image. To demonstrate this Figure 2.1 shows the results of swapping the phases of two images whilst maintaining the original values of $|a_{l,m}|$. Figures 2.1a and 2.1b are images of the Earth¹ and the WMAP ILC² map, respectively (both with the dipole removed). Below the image of the Earth is an image with the ILC's $|a_{l,m}|$ and Earth's $\phi_{l,m}$ (Figure 2.1c). Clearly, the structure of Earth is visible in the image. Figure 2.1d is the reverse image of this: Earth's $|a_{l,m}|$ and ILC's $\phi_{l,m}$. Interestingly, the dark hole in the centre of the ILC image is still maintained in this image. Overall, the large-scale features of the ILC map are mimicked. The reason for the retention of the large-scale structure is that the method acts like a low-pass filter. The vast majority

¹Land and sea floor elevations obtained from the ETOPO5 5-minute gridded elevation data set (Edwards, 1989)

²CMB-only image produced by Bennett *et al.* (2003a) using 1st-yr data from the WMAP satellite. The details of the construction of the map are given in Section 3.3.4

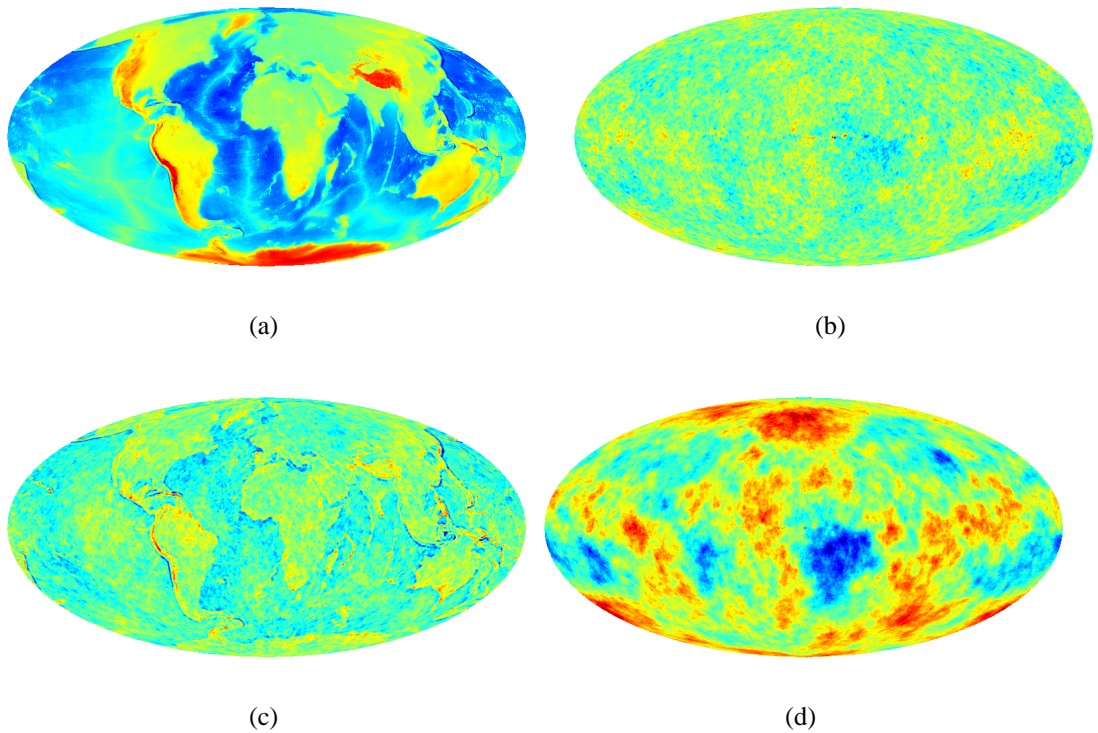


Figure 2.1: (a: top left) Image of Earth, (b: top right) WMAP ILC image, (c: bottom left) image constructed from Earth's $\phi_{l,m}$ and ILC's $|a_{l,m}|$, and (d: bottom right) image constructed from ILC's $\phi_{l,m}$ and Earth's $|a_{l,m}|$.

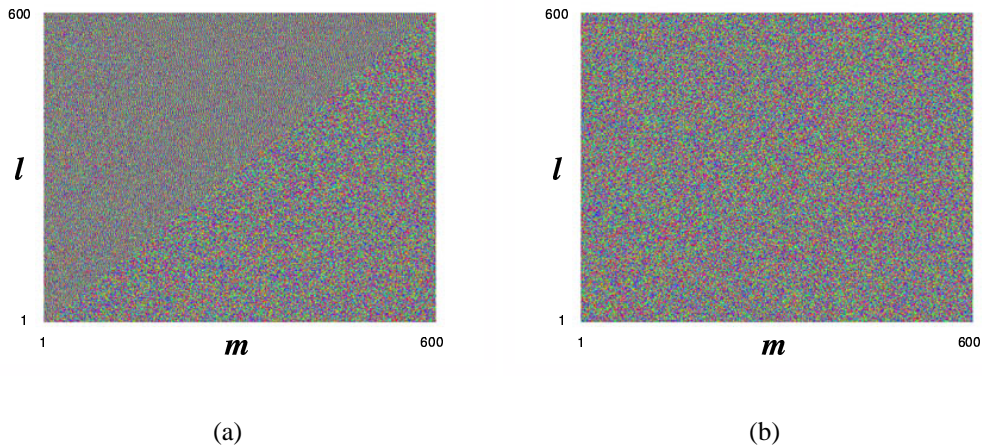


Figure 2.2: (a: left) Phases from WMAP V -band (b: right) and from the WMAP ILC map.

of power in the image of Earth is concentrated at the largest scales and thus it is these features in the ILC that we see in Figure 2.1d.

Before moving onto the development of a phase statistic to probe CMB data, it is worth highlighting how the phases information alters as CMB data is processed. Recently, phase information has been used to produce a clean image of the CMB from WMAP data (Naselsky *et al.*, 2003). Coles & Chiang (2000) presented, in the context of structure formation, a technique to visualise the development of phase coupling by using colour coding. We shall use the method to illustrate the structure in the phases from CMB observations. Their technique makes use of the Hue–Saturation–Brightness (HSB) colour scheme. Hue distinguishes between basic colours. Saturation determines the purity of a colour; i.e. the amount of white mixed in the colour. And finally, brightness signifies the overall intensity of the pixel on a grey-scale. In Coles & Chiang (2000), the phase information is represented by the hue parameter. Critically, the hue parameter is a circular variable like the phases. The phases, ranging from $-\pi$ to π , are trivially converted to the range of the hue parameter [0,1]. A value of $\phi_{l,m} = -\pi$ equates to a hue value of 0 that is equivalent to bright red. The prime hues (red, blue and green) are $2\pi/3$ apart (at $-\pi$, $-\pi/3$, $\pi/3$). The complementary tones (yellow, cyan and magneta) are at $-2\pi/3$, 0, $2\pi/3$, respectively. Due to the circular nature of the hue parameter, red represents both a phase of π and $-\pi$. We use the technique to represent the phases of two CMB data sets up to $l=600$ (with both the saturation and brightness parameters set to 1). In Figure 2.2a the phases from the WMAP V-band are shown. Figure 2.2b shows the phases from the WMAP ILC map that purports to be a clean image of the CMB signal. The top triangle in both images shows phases from the data and the bottom triangle shows a random set of phases. In Figure 2.2a there is clearly structure in the phases; your eyes are able to draw lines connecting parts of image. However, in Figure 2.2b there is no obvious difference between the random phase pattern and that of the ILC phases. Whilst the V-band still contains Galactic foreground contamination, the ILC map appears to have these foregrounds subtracted. Consequently, the phases are potentially a good diagnostic of foreground contamination.

2.3 Fluctuations on a sphere: the spherical harmonics

For analysis of data distributed on a sphere, it is natural to expand over the spherical harmonics. However, the nature of the structure formed by the individual modes

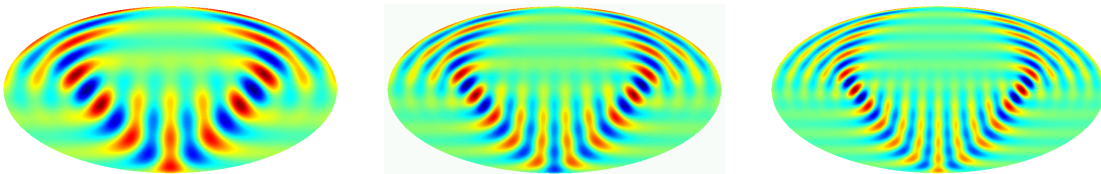


Figure 2.3: The effect of the l -mode. (*left*) $l=10$, (*middle*) $l=15$, (*right*) $l=20$.

is rather complex. If correlations across particular modes are observed, what does it mean? Clearly, correlations across a particular l -mode indicate that a structure is being formed that is intrinsic to this scale. The significance of correlations across certain m -modes is less apparent. Moreover, more complicated correlations can be envisaged. Therefore, to get a handle on the meaning of the correlations across the spherical harmonic modes we look at some simple examples of correlated modes. In these examples, not only are the phases correlated but also the amplitudes. Red corresponds to maxima, blue corresponds to minima and green to the zero-level. However it is worth bearing in mind that a green section in a particular part of the sky does not mean none of the modes form structure there. Instead, it could mean that the various modes are cancelling each other out.

Hopefully, the examples will lead to some insight into the results obtained in the following chapters where correlations are sought across l -modes and m -modes. Furthermore, in chapter 6, we will construct combinations of spherical harmonic modes that are orthogonal to an unevenly distributed sample of rotation measures in order to generate a Faraday rotation template.

2.3.1 Correlated l -modes

In Figure 2.3 images are constructed with $a_{l,m}$ set to 1.0 for all modes at scales of $l=10, 15$ and 20 . The number of spots increases as the scale is increased. Moreover, the value of l corresponds to the number of maxima/minima. Therefore, we can think of l as determining the wavelength of the waves spanning the sphere that construct the image (like in Fourier analysis).

Images of the individual m -modes for the scale of $l=10$ (again with $a_{l,m}=1.0$) are shown in Figure 2.4. These modes combine to form the $l=10$ image in Figure 2.3. The image for $m=0$ appears quite different than the other modes; the mode mainly

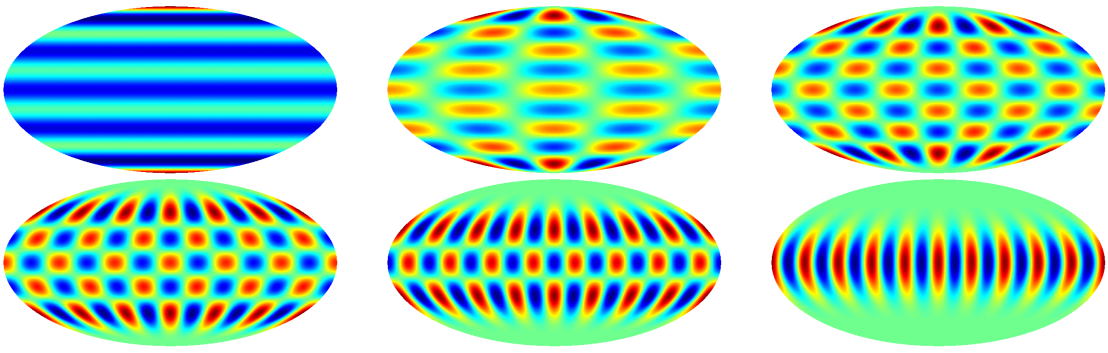


Figure 2.4: Individual modes for $l=10$. (top left) $m=0$, (top middle) $m=2$, (top right) $m=4$, (bottom left) $m=6$, (bottom middle) $m=8$, (bottom right) $m=10$.

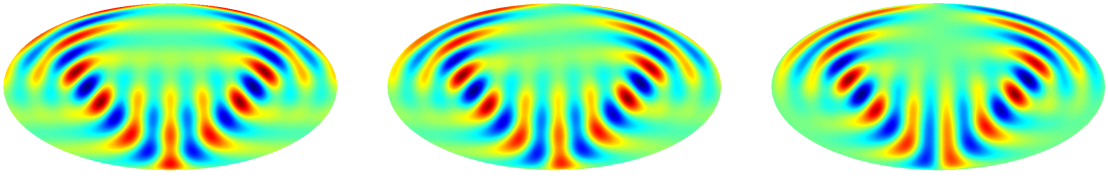


Figure 2.5: The role of phases. (left) $\phi=0$, (middle) $\phi=\pi/2$, (right) $\phi=\pi$.

constructs details in the polar regions. As m is increased, the structure focuses on a smaller band across the sky (but still at the scale of $l=10$). The number of horizontal bands is equal to $(l+1-m)$ bar $m=0$.

It seems now would be an appropriate point to look at the role of the phases. Again, $l=10$ scale is probed. The amplitudes of all the m -modes are set to 1.0 and we look at the scale with all the phases set first to 0, then to $\pi/2$ and π . The images are shown in Figure 2.5. It is clear that the main band is rotated. The maxima in the centre of the image for $\phi=0$ shifts slightly to the right in the image for $\phi=\pi/2$. For $\phi=\pi$, there is neither a maxima or a minima in the centre of the image. Therefore, the phases align maxima for particular scales so that structure is formed at a particular point in an image.

For the remainder of this subsection, the effect of combining different modes for a particular scale is investigated. All the images have $l=16$ and ϕ set to $2\pi/3$. In Figure 2.6, the maximum mode m_{\max} is varied whilst the minimum m_{\min} maintained at 0. All modes from m_{\min} to m_{\max} , inclusive, are used to construct the image. In Figure 2.6, the main band becomes more circular as m_{\max} is increased. The reverse situation is displayed in Figure 2.7: m_{\min} is varied whilst the m_{\max} is maintained at a value of

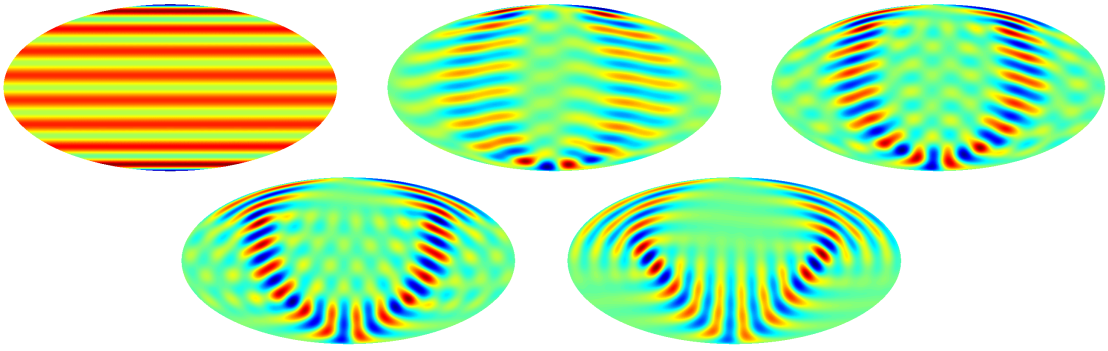


Figure 2.6: Combining modes at $l=16$. (top left) $m_{\max}=0$, (top middle) $m_{\max}=4$, (top right) $m_{\max}=8$, (bottom left) $m_{\max}=12$, (bottom right) $m_{\max}=16$.

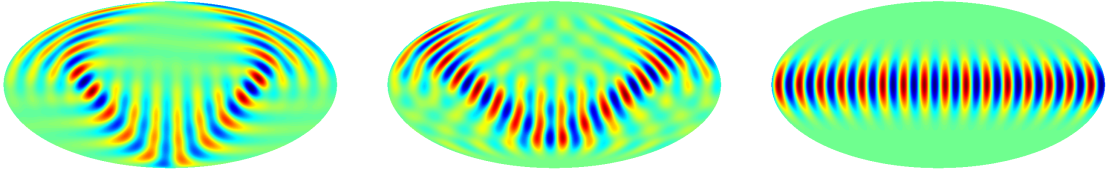


Figure 2.7: Combining modes at $l=16$. (left) $m_{\min}=0$, (middle) $m_{\min}=8$, (right) $m_{\min}=16$.

16. The band is ring-like with $m_{\min}=0$, but, the band straightens as m_{\min} increases. Eventually, the band is straight when $m_{\min}=m_{\max}$.

2.3.2 Correlated m -modes

The previous subsection established the trends seen in correlations across a particular scale. In this subsection, the effect of modes correlating across different scales is investigated. In the what follows the $m=10$ mode is studied with the phases all set to $2\pi/3$. The mode from scales l_{\min} to l_{\max} are combined to form the images seen in Figures 2.8 and 2.9. In Figure 2.8, l_{\min} is varied whilst l_{\max} is fixed at $l=30$. In all the images, there are ten maxima across each band. When $l_{\min}=l_{\max}$, we have just one mode and the pattern expected, from the discussion on Figure 2.4, is seen. As l_{\min} decreases the uppermost band gets sharper (with a vertical pattern of maxima followed by minima). This trend is seen down to roughly $l_{\min}=20$, after which, decreasing l_{\min} leads to the upper band spreading with now a vertical stripe pattern of either maxima or minima. In Figure 2.9, l_{\max} is varied whilst l_{\min} is fixed at $l=10$. Increasing l_{\max} leads to the sole band moving up the image (from the centre when $l_{\max}=10$).

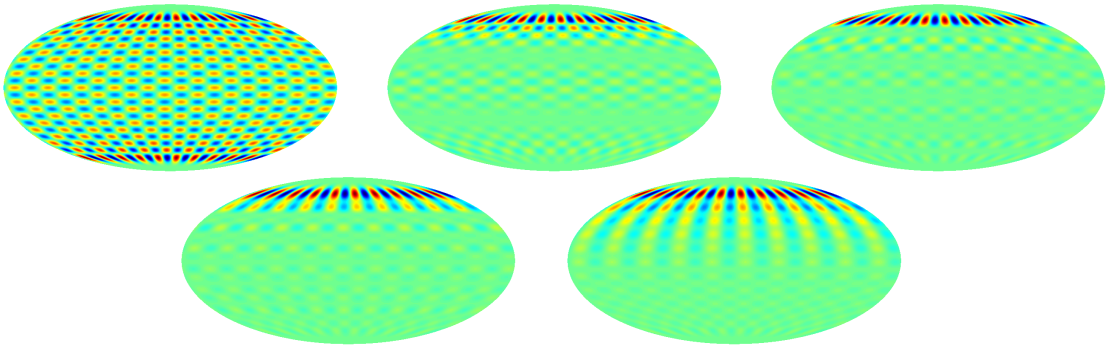


Figure 2.8: Combining $m=10$ modes from different scales. (top left) $l_{\min}=30$, (top middle) $l_{\min}=25$, (top right) $l_{\min}=20$ (bottom left) $l_{\min}=15$ (bottom right) $l_{\min}=10$.

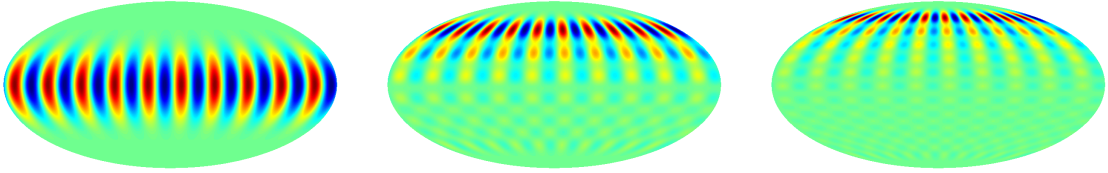


Figure 2.9: Combining $m=10$ modes from different scales. (left) $l_{\max}=10$, (middle) $l_{\max}=20$, (right) $l_{\max}=30$.

Finally, we study the effect of varying m and maintaining the range from $l_{\min}=m$ to $l_{\max}=10$. This is shown in Figure 2.10. It is clear that the value of m , not only determines the number of maxima/minima, but, also effects the height of the main band. The height of the band increases with decreasing value of m . Trivially, one can think of the reduction in the number of spots, from the decrease in m , as causing the band to rise in order to fit the required number across the image.

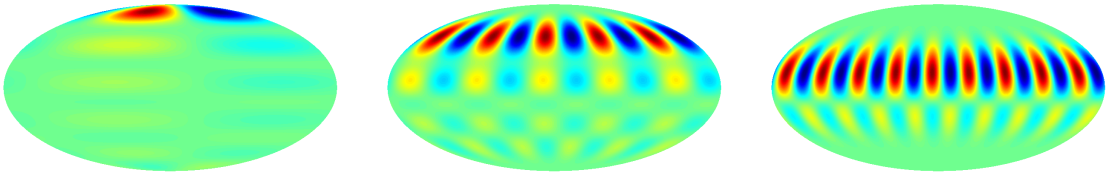


Figure 2.10: Cross-scale correlations for varying m . (left) $m=1$, (middle) $m=5$, (right) $m=9$.

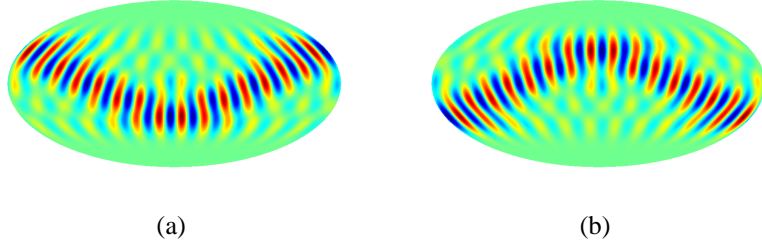


Figure 2.11: (a: left) Original image (b: right) Inverted image

l	m	$\Re(a_{l,m})$	$\Im(a_{l,m})$	$\phi_{l,m}$
16	12	-0.5	-0.87	$4\pi/3$
16	13	0.5	0.87	$\pi/3$
16	14	-0.5	-0.87	$4\pi/3$
16	15	0.5	0.87	$\pi/3$
16	16	-0.5	-0.87	$4\pi/3$

Table 2.1: Non-zero $a_{l,m}$ obtained from the inverted image

2.3.3 Correlations in inverted images

Looking at the images in this section, it is apparent that when a band is straight it is always located in the northern hemisphere. Also, when a band is curved, it is always \cup -shaped rather than \cap -shaped. So how do we get a band in the southern hemisphere or a \cap -shaped band? In Figure 2.11a, there is an image where the only non-zero modes are from $m=12$ to 16 at $l=16$. The modes are set to $\exp i2\pi/3$ i.e. they have a real component of -0.5 and an imaginary component of 0.867. This image was inverted and is displayed in Figure 2.11b. The $a_{l,m}$ were extracted from this inverted image and the non-zero values are displayed in Table 2.1. In order to obtain this \cap -shaped band, even m -modes have negative values of $\Im(a_{l,m})$ corresponding to the original image. Whereas, odd m -modes have negative values of $\Re(a_{l,m})$. This relationship can be further studied by inverting other images with bands in the northern hemisphere and \cup -shaped bands. It becomes apparent that this relationship between the modes of the original and inverted images held for even l . However, the opposite is true for odd values of l : even m -modes had $-\Re(a_{l,m})$ of the original image and odd m -modes had $-\Im(a_{l,m})$ of the original image. Importantly, the production of these structures will manifest themselves as correlated phases which will be useful in later chapters.

Chapter 3

Non-Gaussian fluctuations in the Cosmic Microwave Background radiation

3.1 Introduction

In this chapter, the issue of non-Gaussianity in CMB temperature maps is explored. As stated in the previous chapter, non-Gaussian tracers play a crucial role in characterizing the initial density field. These statistics also play a key function in outlining secondary anisotropies and foreground contaminants in the CMB. This chapter is devoted to the development of a method that utilises the phase information in order to hunt for signs of non-Gaussianity. Unfortunately, there are a wealth of possible correlations within the phases that cannot be comprehensively studied. We focus on phase correlations at a particular scale. Indeed, not only are the phases themselves examined, but also, the phase difference between consecutive modes. The phase difference $D_m(l)$ is defined as

$$D_m(l) = \phi_{l,m+1} - \phi_{l,m}. \quad (3.1)$$

We chose the phase differences not only for their simplicity, but also, because conceptually similar quantities have been found to be very informative in structure formation studies. Chiang & Coles (2000) found the phase difference between consecutive modes in Fourier space to be a useful tracer of the dynamics of nonlinear structure formation.

The quantity defined in Equation (3.1), like the phases, should be uniformly random across the range $[0, 2\pi]$ for a homogeneous Gaussian random field.

The layout of the chapter is as follows. I outline in the next section a procedure that can detect signs of non-randomness in the phases of the spherical harmonic coefficients. In Section 3.3, the method is applied to four types of sky maps: two classes of models and two observational data sets. The conclusions are presented in Section 3.4.

3.2 Testing for phase correlations

3.2.1 Kuiper's statistic

The approach taken in this chapter and ones that follow, is to assume that a set of phases $\phi_{l,m}$ is available. We calculate the phases from a set of spherical harmonic coefficients $a_{l,m}$ obtained from either real or simulated data. The phase differences, as described in the previous section, can then be calculated from the phases. Therefore, let us assume that there are n generic angles. Under the standard statistical assumption, these angles should be random, apart from the constraints described in Section 2.2. We wish to test whether a given set of angles is consistent with being drawn from uniform distribution on the unit circle. This is not quite as simple as it seems. A number of tests require an assumption about the underlying distribution of the angles, such as a bias in a particular direction; see Fisher (1993). Fortunately, there is a fully non-parametric method available known as Kuiper's statistic (Kuiper, 1960). First, the angles are sorted into ascending order, to give the set $\theta_1, \dots, \theta_n$. It does not matter whether the angles are defined to lie in $[0, 2\pi]$, $[-\pi, +\pi]$ or any other range. Each angle θ_i is divided by 2π to give a set of variables X_i , where $i = 1 \dots n$. From the set of X_i , two values S_n^+ and S_n^- are derived where

$$S_n^+ = \max \left\{ \frac{1}{n} - X_1, \frac{2}{n} - X_2, \dots, 1 - X_n \right\} \quad (3.2)$$

and

$$S_n^- = \max \left\{ X_1, X_2 - \frac{1}{n}, \dots, X_n - \frac{n-1}{n} \right\}. \quad (3.3)$$

Kuiper's statistic, V , is then defined as

$$V = (S_n^+ + S_n^-) \cdot \left(\sqrt{n} + 0.155 + \frac{0.24}{\sqrt{n}} \right). \quad (3.4)$$

Anomalously large values of V indicate a distribution that is more clumped than a uniformly random distribution, while low values mean that angles are more regular. The test statistic is normalized by the number of data points, n , in such a way that standard tables can be constructed to determine significance levels for any departure from uniformity; see Fisher (1993). However, it is more convenient to determine the significance of a result from comparisons with Monte Carlo (MC) simulations where the phases are random.

There are further advantages to using Monte Carlo simulations. The issue of conjugate phases discussed in Section 2.2, can be handled by building them into the Monte Carlo generator. More importantly, incomplete sky coverage can be incorporated into the generation. Observations are often hindered by Galactic foreground contamination, leading to a Galactic cut. This cut can introduce phase correlations. However, applying the same cut to the MC skies, can overcome this problem. One would then need to determine whether V from an observed sky is consistent with having been drawn from the set of values of V generated over the Monte Carlo ensemble.

3.2.2 Rotation of coordinate system

When analysing the spherical harmonic coefficients, the orientation the data is presented in needs to be taken into account. Both the COBE–DMR and WMAP results were presented with the z –axis set perpendicular to the Galactic plane. The choice of coordinate system influences the values of the $a_{l,m}$ and thus the $\phi_{l,m}$. A measured sky can generate an infinite number of different sets of $\phi_{l,m}$ since the phases are not rotationally invariant. An apparently non-random set of phases may be the result of a chance alignment of a feature in the sky with the coordinate axes. It is clear that this aspect of the phases may influence the results of any statistical test. Rotating the coordinate system will lead to stronger conclusions about the nature of the CMB data that is not unique to one orientation. In order to overcome this problem, one can arbitrarily rotate the coordinate system and recalculate the $\phi_{l,m}$. A new value of the statistic will be obtained and, after a number of rotations, a distribution of V can be generated. The process can be applied to both real and Monte Carlo skies. The distributions corresponding to the real and MC skies can then be compared. A similar approach is taken by Hansen, Marinucci & Vittorio (2003). Alternatively, one could compile a grid of

orientations uniformly covering the sky and calculate the distribution of V from these coordinate systems. However, the first method allows the stability of a result to be checked by repeating the process and ensuring a similar result is obtained. Therefore, the first method is incorporated into the practical procedure presented later.

An arbitrary rotation of a coordinate system about the origin can be specified by three real parameters. Rotations of coordinate systems are most usefully described in terms of the Euler angles α , β and γ . The rotation of the coordinate system $S\{x, y, z\} \rightarrow S'\{x', y', z'\}$ can be performed by three successive rotations about the coordinate axes (Varshalovich, Moskalev & Khersonskii, 1988, hereafter VMK). The new coordinate system is obtained by executing these three rotations about two of the three mutually perpendicular axes. Two methods can describe this

- (a) A rotation of the z -axis through an angle α
- (b) A rotation of the new y -axis through an angle β
- (c) A rotation of the new z -axis through an angle γ

or

- (a) A rotation of the z -axis through an angle γ
- (b) A rotation of the initial y -axis through an angle β
- (c) A rotation of the initial z -axis through an angle α

where $0 \leq \alpha < 2\pi$, $0 \leq \beta \leq \pi$ and $0 \leq \gamma < 2\pi$. α and γ are drawn from uniform distributions, whereas, β is drawn from a $\sin(\theta)d\theta$ distribution. It can be shown that the relative orientations of the initial and final axes are the same for both methods (Edmonds, 1960).

The effect the rotations have on a coordinate vector \mathbf{r} are described by three matrices

$$\mathbf{r}' = \begin{bmatrix} x' \\ y' \\ z' \end{bmatrix} = \begin{bmatrix} \cos \gamma & \sin \gamma & 0 \\ -\sin \gamma & \cos \gamma & 0 \\ 0 & 0 & 1 \end{bmatrix} \begin{bmatrix} \cos \beta & 0 & -\sin \beta \\ 0 & 1 & 0 \\ \sin \beta & 0 & \cos \beta \end{bmatrix} \begin{bmatrix} \cos \alpha & \sin \alpha & 0 \\ -\sin \alpha & \cos \alpha & 0 \\ 0 & 0 & 1 \end{bmatrix} \begin{bmatrix} x \\ y \\ z \end{bmatrix} \quad (3.5)$$

or

$$\mathbf{r}' = \mathbf{D}(0, 0, \gamma)\mathbf{D}(0, \beta, 0)\mathbf{D}(\alpha, 0, 0)\mathbf{r} \equiv \mathbf{D}(\alpha, \beta, \gamma)\mathbf{r} \quad (3.6)$$

where \mathbf{D} corresponds to a rotation operator. On the other hand, a scalar field f is unchanged by a change of the frame of reference

$$f'(\mathbf{r}') = f(\mathbf{r}). \quad (3.7)$$

A procedure is required to evaluate the values of the $a_{l,m}$ in a rotated coordinate frame. The Wigner D -function $D_{m,m'}^l(\alpha, \beta, \gamma)$ provides us with such a mechanism (VMK). The Wigner D -function realizes transformations of the covariant component (i.e. m) of any rank l tensor under coordinate rotation. The arguments α , β and γ are Euler angles that specify the rotation. If we consider a tensor $u_{l,m}(\theta, \phi)$ and apply the rotation operator then

$$\hat{D}(\alpha, \beta, \gamma)u_{l,m}(\theta, \phi) = \sum_m D_{m,m'}^l(\alpha, \beta, \gamma)u_{l,m}(\theta, \phi) = u'_{l,m'}(\theta', \phi'). \quad (3.8)$$

Similarly, the operator can act on the spherical harmonics $Y_{l,m}(\theta, \phi)$. From equation (3.7), we see

$$\frac{\Delta T}{T}(\theta, \phi) = \frac{\Delta T'}{T}(\theta', \phi'). \quad (3.9)$$

Thus, the rotated $a_{l,m}$ can be calculated from

$$\frac{\Delta T'}{T}(\theta', \phi') = \sum_l \sum_{m'} a'_{l,m'} Y'_{l,m'}(\theta', \phi') \quad (3.10)$$

$$= \sum_l \sum_{m'} a'_{l,m'} \sum_m D_{m,m'}^l(\alpha, \beta, \gamma) Y_{l,m}(\theta, \phi) \quad (3.11)$$

$$= \sum_l \sum_m a_{l,m} Y_{l,m}(\theta, \phi) \quad (3.12)$$

if

$$a_{l,m} = \sum_{m'} a'_{l,m'} D_{m,m'}^l(\alpha, \beta, \gamma). \quad (3.13)$$

From Equation (3.13), it is clear that in order to calculate the rotated $a_{l,m}$ the value of the Wigner D -function has to be calculated for a particular l (given α , β and γ). The Wigner D -function is complex and its calculation can be made simpler if it is expressed as

$$D_{m,m'}^l(\alpha, \beta, \gamma) = e^{-im\alpha} d_{m,m'}^l(\beta) e^{-im'\gamma}, \quad (3.14)$$

where $d_{m,m'}^l(\beta)$ is real and equivalent to $D_{m,m'}^l(0, \beta, 0)$. The computational task is now to generate the $d_{m,m'}^l(\beta)$. Methods for generating $d_{m,m'}^l(\beta)$ are given in VMK, however, the iteration formulae require a division through by $\sin \beta$ and when β is

small computational problems arise. Wright & Earl (2002) suggest using an alternative method that is based on Edmonds (1960) definition using spin matrices σ . The $d_{m,m'}^l(\beta)$ can be calculated using the following definition

$$\begin{aligned} d_{m,m'}^l(\beta) = & \left[\frac{(l+m')!(l-m')!}{(l+m)!(l-m)!} \right]^{1/2} \\ & \cdot \sum_{\sigma=0}^n \binom{l+m}{l-m'-\sigma} \binom{l-m}{\sigma} (-1)^{l-m'-\sigma} \\ & \cdot \left(\cos \frac{\beta}{2} \right)^{2\sigma+m'+m} \left(\sin \frac{\beta}{2} \right)^{2l-2\sigma-m'-m}, \end{aligned} \quad (3.15)$$

where the n is taken as the the smallest of $l - m$ and $l - m'$. VMK also reveal the following symmetry properties of $d_{m,m'}^l(\beta)$ that can aid in reducing the computational time for generating them

$$d_{m,m'}^l(\beta) = (-1)^{m-m'} d_{-m,-m'}^l(\beta) \quad (3.16)$$

$$d_{m,m'}^l(\beta) = (-1)^{m-m'} d_{m,m'}^l(\beta) \quad (3.17)$$

$$d_{m,m'}^l(\beta) = d_{-m',-m}^l(\beta). \quad (3.18)$$

These relations help map $d_{m,m'}^l(\beta)$ into different region of harmonic space.

In order to test the generation procedure of the Wigner D -function the following relations for particular values of the Euler angles were sought

$$D_{m,m'}^l(0, 0, 0) = \delta_{m,m'} \quad (3.19)$$

$$D_{m,m'}^l(\alpha, 0, \beta) = \delta_{m,m'} e^{-m(\alpha+\gamma)} \quad (3.20)$$

$$D_{m,m'}^l(\alpha, \pm 2k\pi, \gamma) = \delta_{m,m'} (-1)^{2kl} e^{-m(\alpha+\gamma)}, \quad (3.21)$$

where k is an integer. Again, these relationships were taken from VMK. VMK also contained tables giving the explicit form of $d_{m,m'}^l(\beta)$ for $l=1 - 5$; the form of $d_{m,m'}^l(\beta)$ for $l=1$ is given in Table 3.1. Note that the explicit form for $l=1$ highlights the relationships displayed in Equations (3.16–3.18). Therefore, to further test the generation of the $d_{m,m'}^l(\beta)$ values for $d_{m,m'}^1(\beta)$ and $d_{m,m'}^2(\beta)$ were calculated by hand for various β . The generated values were found to follow the relations and the explicit values calculated by hand.

The Wigner D -function represents the matrix elements of the rotation operator $\hat{D}(\alpha, \beta, \gamma)$. Therefore, applying the function to the $a_{l,m}$ should purely rotate the frame of reference

$m \backslash m'$	1	0	-1
1	$\frac{1+\cos\beta}{2}$	$\frac{-\sin\beta}{\sqrt{2}}$	$\frac{1-\cos\beta}{2}$
0	$\frac{\sin\beta}{\sqrt{2}}$	$\cos\beta$	$\frac{-\sin\beta}{\sqrt{2}}$
-1	$\frac{1-\cos\beta}{2}$	$\frac{\sin\beta}{\sqrt{2}}$	$\frac{1+\cos\beta}{2}$

Table 3.1: Explicit form of $d_{m,m'}^l(\beta)$ for $l=1$.

and leave the length for a particular mode unaltered. If we define the length as

$$|A_l| = \sqrt{\sum_m a_{l,m}}, \quad (3.22)$$

then

$$|A_l| = |A'_l| = |A''_l| = \text{constant}. \quad (3.23)$$

This allows the rotation code to be tested for any values of $l > 5$ and for $\alpha, \gamma \neq 0$.

3.2.3 Implementation

To begin with, a set of $a_{l,m}$ (whether from a real, model or Monte Carlo sky) need to be extracted or generated. This set of $a_{l,m}$ can be used to produce a rotated set of $a_{l,m}$ when the Wigner D -function is employed in the manner outlined in the previous subsection. Random values of α, β and γ are chosen. From this new rotated set of $a_{l,m}$, two subsets of the phases are studied (for a given scale): the phases $\phi_m(l)$ themselves and the phase differences $D_m(l)$ between consecutive modes. Kuiper's statistic V_{cmb} is calculated for both subsets. After a number of rotations, a distribution of V_{cmb} is formed from the original set of $a_{l,m}$. This distribution is then split into equally-spaced bins. 3000 rotations and 100 bins spaced between $V=0$ to 2.5 were necessary to achieve stable results.

In order to get a handle on the significance of a distribution of V_{cmb} , the data set was compared to 1000 Monte Carlo simulations with phases randomly drawn from an uniform distribution $[0, 2\pi]$. The same procedure was applied to the MC sets of $a_{l,m}$ to produce a binned distributions of V_{MC} . An average distribution of V_{MC} was formed from the distributions corresponding to the MC simulations. A χ^2 test was then applied to the distributions from the original data and the MC average. That is to say, we

calculated

$$\chi^2 = \sum_i \frac{(f_i - \bar{f}_i)^2}{\bar{f}_i}, \quad (3.24)$$

where the summation is over all the bins and \bar{f}_i is the number expected in the i th bin from the overall average distribution. The larger the value of χ_{cmb}^2 the less likely the distribution functions were drawn from the same parent distribution. The distribution of V_{cmb} was assumed to be compatible with a distribution drawn from a sky with random phases, if the value of χ_{cmb}^2 was less than 95% of χ_{MC}^2

So what scales are studied in the following section? We applied the method to only low values of l . There is no difficulty in principle in extending this method to very high spherical harmonics, but the computational generation of Wigner D -function scales by $\sim l^2$ so the application was limited to $l=20$. Furthermore, only even values of l were assessed in order to keep the analysis computationally manageable and also because these were the only modes available to me from the COBE-DMR data (Section 3.3.3). Besides this, the analysis is suited to a small number of independent data points: correlations between certain phases are not hidden by a large number of random phases. On the same note, but as an aside, the method was applied to the whole sample of phases and phase differences ($l=1-20$) for all the sky maps analysed in the next Section, without results. This was true even when stark signals were seen when scanning across individual scales, as we will discuss in the next section.

3.3 Application to sky maps

3.3.1 Toy models

As a first check on the suitability of the method for detecting evidence of non-Gaussianity in CMB sky maps, sets of spherical harmonic coefficients were created with phases drawn from non-uniform distributions. Three types of distributions were used to test the method: (i) the phases were coupled (ii) the phases were drawn from a cardioid distribution and (iii) the phases were drawn from a wrapped Cauchy distribution; see Fisher (1993). The fake sets of coefficients were created in a manner that insured that the orthonormality of the coefficients was preserved as outlined in Section 2.2.

The first non-uniform distribution of phases is constructed using the following rela-

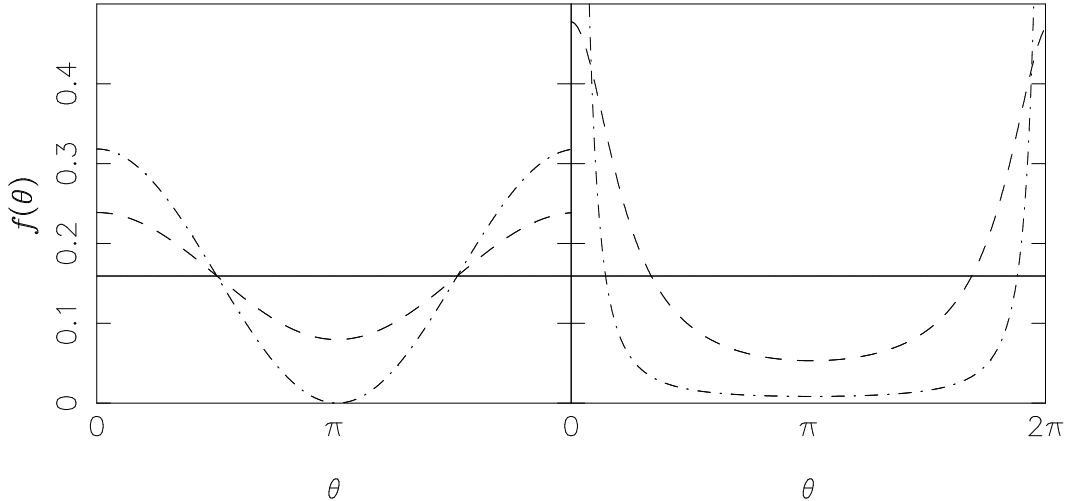


Figure 3.1: Probability density functions for (*left*) cardioid and (*right*) wrapped Cauchy distributions. The solid line, dashed line, and dot-dashed line correspond to $\rho=0, 0.25, 0.5$ and $\rho=0, 0.5, 0.9$ for the cardioid and wrapped Cauchy distributions respectively.

tionship

$$\phi_{l,m} = \phi_{l,m-1} + k \quad (3.25)$$

where $\phi_{l,-l}$ is a random number chosen between 0 and 2π . The results of the simulation with $k=1$ are shown in panel (i) of Tables 3.2 and 3.3. The sky is taken to be non-Gaussian if χ^2_{sky} is larger than 95 % of χ^2_{MC} for a particular mode. The phase difference method should be particularly suited to detecting this kind of deviation from Gaussianity because the phase differences are all equal in this case; the distribution of phase differences is therefore highly concentrated rather than uniform. Nevertheless, the non-uniformity is so clear that it is evident from the phases themselves, even for low modes. On the other hand, assessing non-uniformity from the quadrupole mode $l=2$ on its own is difficult even in this case. This is due to the small number of independent variables available.

The cardioid distribution was chosen because studies of the non-linear regime in structure formation have shown phases rapidly move away from their initial values. They wrap around many multiples of 2π and the 'observed' phases appear random (Chiang & Coles, 2000; Watts, Coles & Melott, 2003). However, this evolution can be distinguished by the phases differences which appear to be drawn from a roughly cardioid distribution (Watts, Coles & Melott, 2003). The cardioid distribution has a probability density function given by

$$f(\theta) = \frac{1}{2\pi}[1 + 2\rho \cos(\theta)], \quad 0 \leq \theta < 2\pi, 0 \leq \rho \leq 1/2, \quad (3.26)$$

where ρ is the mean resultant length. As $\rho \rightarrow 0$ the distribution converges to a uniform distribution. The distribution is illustrated in Figure 3.1. The kurtosis of the distribution is given by

$$K = -\frac{\rho^4}{(1-\rho)^2}. \quad (3.27)$$

Sets of coefficients were produced from distributions with $\rho=0, 0.2, 0.4$ and 0.5 . The distributions themselves were generated using rejection methods. The results are given in panel (ii) of Tables 3.2 and 3.3. The results with $\rho=0$ are not shown: they indicate the coefficients are taken from a Gaussian random field, as expected. Furthermore, with $\rho=0.5$ the non-uniformity detected in the phases and phase differences for $l=20$ is not particularly significant, however, the kurtosis for this distribution is not especially large.

Phases were drawn from wrapped Cauchy distributions in order to test the method against skies with larger values of kurtosis. The wrapped Cauchy distribution has a probability density function given by

$$f(\theta) = \frac{1}{2\pi} \frac{1-\rho^2}{1+\rho^2-2\rho \cos(\theta)}, \quad 0 \leq \theta < 2\pi, 0 \leq \rho \leq 1 \quad (3.28)$$

The kurtosis is given by

$$K = \frac{(\rho^2 - \rho^4)}{(1-\rho)^2}. \quad (3.29)$$

As $\rho \rightarrow 0$ the distribution tends towards a uniform distribution. As $\rho \rightarrow 1$ the distribution tends towards a distribution concentrated at $\phi=0$. The distribution is shown in Figure 3.1. Fisher (1993) gives a method for simulating the distribution. Sets of coefficients were created for $\rho=0, 0.2, 0.4, 0.6, 0.8$ and 1 . The results are given in panel (iii) of Tables 3.2 and 3.3. Again, $\rho=0$ is not displayed, but was used to check the distribution simulation was correct because it should correspond to a uniformly random distribution. For $\rho \geq 0.6$ the coefficients are distinctly non-Gaussian. The results in the Table indicate that the method can pick out departures from uniformly random phase distributions, at 95% confidence level for $|K| \gtrsim 1$. Note also that the results from $\rho=1$ demonstrate that firm conclusions about the Gaussianity of the sky are difficult to draw using the quadrupole alone. Even for the highly non-Gaussian distribution with $K=\infty$, the statistic does not prove to be discriminatory. In summary, however, the tests on toy models do show that the method can pick out departures from the random phase hypothesis in CMB sky maps using low multipole modes.

K	i	ii			iii				
l		-0.003	-0.07	-0.25	0.06	0.37	1.44	5.76	∞
2	76	79	29	81	53	21	68	98	52
4	96	56	41	44	68	77	39	68	100
6	100	18	56	83	61	41	99	85	100
8	100	99	16	64	97	18	99	100	100
10	100	11	64	39	19	63	24	99	100
12	100	22	45	34	38	96	39	95	100
14	100	63	4	82	60	62	93	97	100
16	100	69	41	31	16	68	72	100	100
18	100	83	63	44	54	18	100	100	100
20	100	5	72	95	64	1	83	100	100

Table 3.2: $\phi_m(l)$ results for toy model skies

K	i	ii			iii				
l		-0.003	-0.07	-0.25	0.06	0.37	1.44	5.76	∞
2	67	81	63	90	52	46	37	98	35
4	97	68	41	12	79	89	28	69	100
6	100	18	66	87	25	4	98	95	100
8	100	98	69	8	74	87	99	100	100
10	100	34	66	12	44	32	65	99	100
12	100	37	80	71	58	7	55	72	100
14	100	22	29	85	79	40	28	65	100
16	100	48	78	88	43	78	89	99	100
18	100	8	5	23	84	19	100	100	100
20	100	85	55	99	53	27	32	99	100

Table 3.3: $D_m(l)$ results for toy model skies

3.3.2 Quadratic non-Gaussian maps

In order to further examine the performance of our statistic, it was applied to non-Gaussian models with stronger physical foundations. At large scales, the CMB is dominated by the Sachs–Wolfe (Sachs & Wolfe, 1967) effect so that the temperature fluctuations are proportional to fluctuations in the gravitational potential on the last scattering surface. Non-Gaussian CMB skies can be generated by introducing a non-linear term in the gravitational potential $\Phi(n)$

$$\Phi(n) = \Phi_L(n) + f_{nl}(\Phi_L^2(n) - \langle \Phi_L^2(n) \rangle) \quad (3.30)$$

l	$\phi_m(l)$					$D_m(l)$				
	a	b	c	d	e	a	b	c	d	e
2	35	40	46	46	47	38	38	45	40	34
4	81	83	81	83	79	78	76	76	78	78
6	49	31	52	53	76	46	44	43	37	41
8	19	43	14	41	1	68	63	67	65	63
10	97	97	97	98	97	96	96	96	96	96
12	49	38	1	1	59	13	24	14	3	7
14	61	77	33	31	35	3	10	77	8	10
16	4	77	87	92	39	57	66	67	59	65
18	97	94	94	96	97	92	92	91	94	93
20	64	58	7	51	36	30	19	18	30	23

Table 3.4: Results for COBE DMR data based on phases and phase differences between consecutive values of m at a fixed l . The method was applied to 5 realisations of the DMR sky in order to demonstrate the stability of the results.

where $\Phi_L(n)$ refers to the linear part of the potential, f_{nl} is the non-linear parameter controlling the amount of non-Gaussianity and the brackets indicate a volume average (Liguori, Matarrese & Moscardini, 2003). The method was applied to these types of skies with varying levels of non-Gaussianity controlled by the parameter f_{nl} .

The results for the most extreme form of non-Gaussianity ($f_{nl} = \infty$) are shown in panel (i) in Table 3.5. Note that the statistic is clearly unsuitable for detecting this form of non-Gaussianity. Even for this severe level of non-Gaussianity the method is incapable of finding any deviations of the phases or phase differences from the random phase hypothesis. The reason for this is that the very simple form of phase association sought by the statistic does not pick up very sensitively the quadratic correlations manifested by the model given in Equation (3.30); see Watts & Coles (2003). The reason for this failure is that the statistic is more sensitive to departures from statistical homogeneity over the whole sky. The models here are certainly non-Gaussian, but are statistically homogeneous over the whole sphere. Therefore, the statistic will be sensitive to forms of non-Gaussianity, such as blobs or edges, that occupy a large fraction of the sky. This characteristic of the statistic will be useful when interpreting real data.

3.3.3 COBE–DMR data

In the following subsections, the method will be applied to real data in order to see if any signs of non-random phases can be found in available CMB sky maps. In this subsection, the $a_{l,m}$ obtained from COBE–DMR data are studied. In the following subsection, the method is applied to $a_{l,m}$ obtained from five all-sky maps derived from WMAP data.

The DMR (Differential Microwave Radiometer) instrument on board the COBE satellite ushered in the era of precision cosmology by measuring primordial temperature fluctuations of order $\Delta T/T = 10^{-5}$ in the CMB. The DMR instrument comprised six differential microwave radiometers: two nearly independent channels, labelled A and B, at frequencies 31.5, 53 and 90 GHz. The data from all three frequencies have been used to calculate the $a_{l,m}$ corresponding to the CMB signal from regions outside the Galactic cut.

The results of the application of the method on the $a_{l,m}$ are displayed in Table 3.4. The method was applied to five realisations (rotations) of the DMR sky in order to examine whether the results were stable and consequently whether the conclusions were robust. In the table, it is clear that the large values of χ^2 do appear stable but for lower values (when the phases appear random) the probabilities depend strongly upon the realisation. However, we are only interested in significance levels that are larger than 95% and these appear stable for all realisations. The statistic indicates that both the phases and phase differences of $l=10$ mode appear non-random. For all 5 realisations, the χ^2 values are larger than 95% of the MC skies. The phases for $l=18$ also appear unusual, however, the confidence of this result depends on the realisation.

Non-Gaussian signatures in the COBE–DMR data have been reported in the literature before (Ferreira, Magueijo & Gorski, 1998; Pando, Valls-Gabaud & Fang, 1998). However, the origin of these signals is probably systematic errors in the data processing rather than cosmological; see Bromley & Tegmark (1999) for a discussion on the issue. Interestingly, the bispectrum statistic used by Ferreira, Magueijo & Gorski (1998) found the dominant non-Gaussian contribution near $l=16$. The statistic developed here detects a non-Gaussian signal at $l=10$. This illustrates that the two statistics are probing different aspects of the statistical nature of the temperature field. This demonstrates the value of complimentary tracers of non-Gaussianity.

l	$\phi_m(l)$						$D_m(l)$					
	i	ii	iii	iv	v	vi	i	ii	iii	iv	v	vi
2	13	15	4	43	51	81	92	31	11	17	66	44
4	46	11	25	36	32	93	59	38	33	42	35	93
6	32	94	96	94	97	96	2	91	95	93	96	94
8	89	73	17	19	14	35	61	23	11	34	2	34
10	37	49	13	11	47	46	29	47	7	8	43	22
12	74	82	81	87	98	96	84	85	52	71	79	94
14	55	85	95	96	82	87	34	95	98	98	90	95
16	12	100	100	90	96	88	41	99	99	97	97	79
18	48	77	57	87	25	3	22	52	92	89	64	40
20	64	20	59	50	17	76	70	49	23	30	63	16

Table 3.5: Results based on phases and phase differences between consecutive values of m at a fixed l . The results show the significance levels of detected departures from random phases for (i) the quadratic non-Gaussian map ($f_{nl} = \infty$), (ii) the ILC map, (iii) the cleaned TOH map , (iv) the Wiener filtered TOH map, (v) the Eriksen map and (vi) the Naselsky map.

3.3.4 WMAP 1-yr data

The WMAP instrument comprises 10 differencing assemblies (consisting of two radiometers each) measuring over 5 frequencies ($\sim 23, 33, 41, 61$ and 94 GHz). The WMAP team have released an internal linear combination (ILC) map that combined the five frequency band maps in such a way to maintain unit response to the signal CMB while minimising the foreground contamination. The construction of this map is described in detail in Bennett *et al.* (2003b). To further improve the result, the inner Galactic plane is divided into 11 separate regions and weights determined separately. This takes account of the spatial variations in the foreground properties. Thus, the final combined map does not rely on models of foreground emission and therefore any systematic or calibration errors of other experiments do not enter the problem. The final map covers the full-sky and should represent only the CMB signal, although it is not anticipated that foreground subtraction is perfect.

Following the release of the WMAP 1-yr data Tegmark, de Oliveira-Costa & Hamilton (2003, hereafter TOH) have produced a cleaned CMB map. They argued that their version contained less contamination outside the Galactic plane compared with the internal linear combination map produced by the WMAP team. The five band maps are combined with weights depending both on angular scale and on the distance from

the Galactic plane. The angular scale dependence allows for the way foregrounds are important on large scales whereas detector noise becomes important on smaller scales. TOH also produced a Wiener filtered map of the CMB that minimizes rms errors in the CMB. Features with a high signal-to-noise are left unaffected, whereas statistically less significant parts are suppressed. While their cleaned map contains residual Galactic fluctuations on very small angular scales probed only by the W -band, these fluctuations vanish in the filtered map.

Two more CMB-only sky maps have since been released; see Eriksen *et al.* (2004a) and Naselsky *et al.* (2003) for details. I shall refer to these two maps as the Eriksen and Naselsky maps, respectively. The Eriksen map is constructed in a similar manner to the WMAP ILC, but claims to have 12% less variance. This reduction is attributed to the removal of more noise. The generation of the Naselsky map is based on phase-analysis of Galactic foreground components. The underlying assumption is that the phases of the CMB signal, after foreground cleaning, should correlate as little as possible with those of the foregrounds. Unlike the other four maps, the sky is not dissected into smaller regions; the method is applied over the whole-sky.

The five all-sky maps are available in HEALPix¹ format (Gorski, Hivon & Wandelt, 1999). The $a_{l,m}$ for each map were derived using the 'anafast' routine in the HEALPix package. The results are shown in panels (ii) to (vi) in Table 3.5. The results for the ILC map suggest there are departures from the random phase hypothesis for the phases of $l=16$ and the phase differences for $l=14$ and 16. The departure for $l=16$ appears very strong with the χ^2 value being larger than 995 of the values obtained for the MC skies.

The distributions of Kuiper's statistic for the phase differences from two modes are shown in Figure 3.2. The plot for $l=10$ (Figure 3.2a) illustrates that the distribution corresponding to the ILC fits in with the scatter of the random sample of MCs around the average distribution. Whereas, in the plot for $l=16$ (Figure 3.2b), the ILC distribution is undoubtedly different to that corresponding to the average distribution. It is also worth pointing out that, in Figure 3.2a, there is a larger scatter in the shape of the distributions corresponding to the MCs for $l=10$. This is not by chance, instead, it is due to the smaller number of independent data points for $l=10$. Consequently, it is harder to unearth signs of non-uniformity in the lower multipoles. As a result, more

¹<http://www.eso.org/science/healpix/>

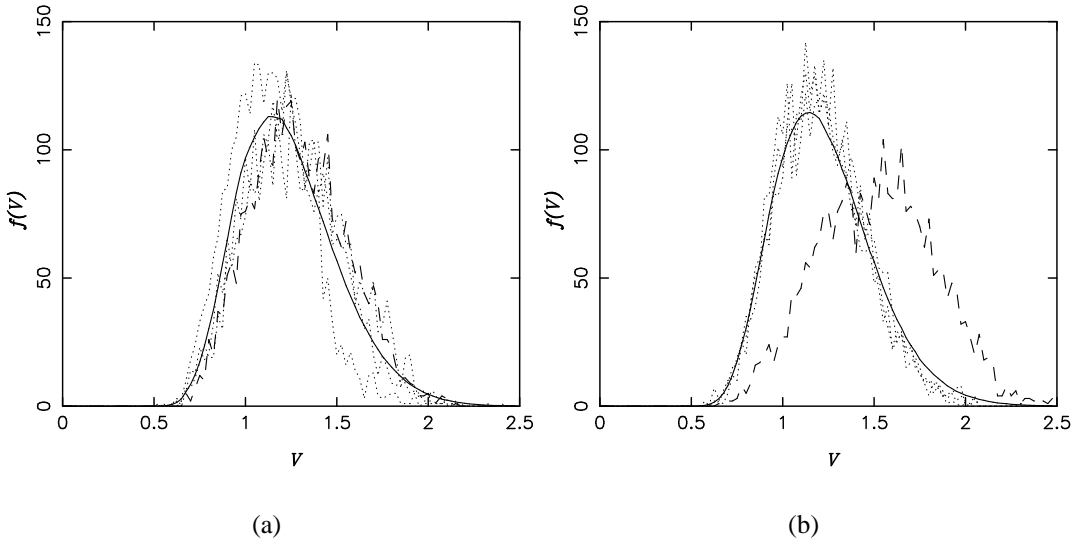


Figure 3.2: Distribution of Kuiper's statistic for the phase differences. The straight line, dotted lines and dashed line correspond to distributions of the average of the 1000 MC skies, three randomly chosen MC skies and the ILC, respectively. (a: left) $l=10$ and (b: right) $l=16$.

weight should be attached to detections in the higher multipoles as any detection is less likely to be a statistical fluke.

To investigate the $l=16$ mode further, the temperature pattern on the sky was reconstructed solely using the spherical harmonic modes for $l=16$ with their appropriate $a_{l,m}$ and compared this with a map with the same power spectrum but with random phases (Figure 3.3). The result confirms that the method is very sensitive to departures from statistical homogeneity. The $l=16$ modes are clearly forming a more structured pattern than the random-phase counterpart. The alignment of these modes with the Galactic plane is striking.

The morphological appearance of these fluctuations as a band across the Galactic plane may be indicative of residual foreground still present in the CMB map after foreground removal. This is the most likely explanation for the alignment of features relative to the Galactic coordinate system. The scanning strategy was such that the ecliptic poles and rings around the poles were observed the greatest number of times (Bennett *et al.*, 2003a). Thus, noise and problems associated with data processing is unlikely to form such a feature. Further evidence for foreground contamination is provided by signs of cross-correlations of the phases of CMB maps with various foreground components (Naselsky, Doroshkevich & Verkhodanov, 2003; Chiang & Naselsky, 2004). Alter-

natively, the structure may be the consequence of the angular scale $l=16$ relating to the width of the zones used to model the Galactic plane in the generation of the ILC. In any case, one should certainly avoid jumping to the conclusion that this represents anything primordial. The ILC is constructed from preliminary data and has complex variations in signal-to-noise across the sky. Nevertheless, the ILC result shows that the method is useful for testing realistic observational data for departures from the standard cosmological statistics.

The two maps produced by Tegmark, de Oliveira-Costa & Hamilton (2003) also suggest that the phases for the $l=16$ scale are non-random. The cleaned map shows departures from the random phase hypothesis at greater than 95% confidence for the phases and phase differences of $l=6, 14$ and 16 . The Wiener filtered map finds departures for the phases corresponding to $l=14$ and phase differences in $l=14$ and 16 . Both the cleaned and the Wiener filtered maps of TOH display similar band patterns to that observed in the $l=16$ map for the ILC. The Wiener filtered TOH map is shown for comparison in Figure 3.3.

The Eriksen map displays similar signs of non-uniformity in the phases as those in the ILC and the two TOH maps. The phases and phases differences for $l=6$ and 16 are picked out by the statistic. On the other hand, the Naselsky map shows the weakest signs of non-uniformity in the phase differences, with just the $l=14$ highlighted by the statistic. There is no indication of anything unusual in both the phases and the phase differences at $l=16$. Unlike the other maps, the Naselsky map is processed over the whole sphere. This may add weight to the belief that the structure seen in Figure 3.3 is the result of the division of the sky during the map-making process. Then again, the lack of phase correlations at $l=16$ may instead be an indication that the foreground components are better handled in the generation of this map.

So far I have focused mainly on the $l=16$ mode, however, the results for $l=6$ appear also to be hinting at something unusual. Signs of non-random phases in the mode are seen in three of the maps, whilst results from the other two maps have significance levels slightly under the 95% threshold. Eriksen *et al.* (2004a) noted the peculiar nature of this mode when investigating the planarity of low multipoles in the ILC and Eriksen maps. The mode was found to be more planar than 98% of their MC simulations. Their investigation was prompted by the planar nature and alignment of the quadrupole and octopole (Tegmark, de Oliveira-Costa & Hamilton, 2003; de Oliveira-Costa *et al.*,

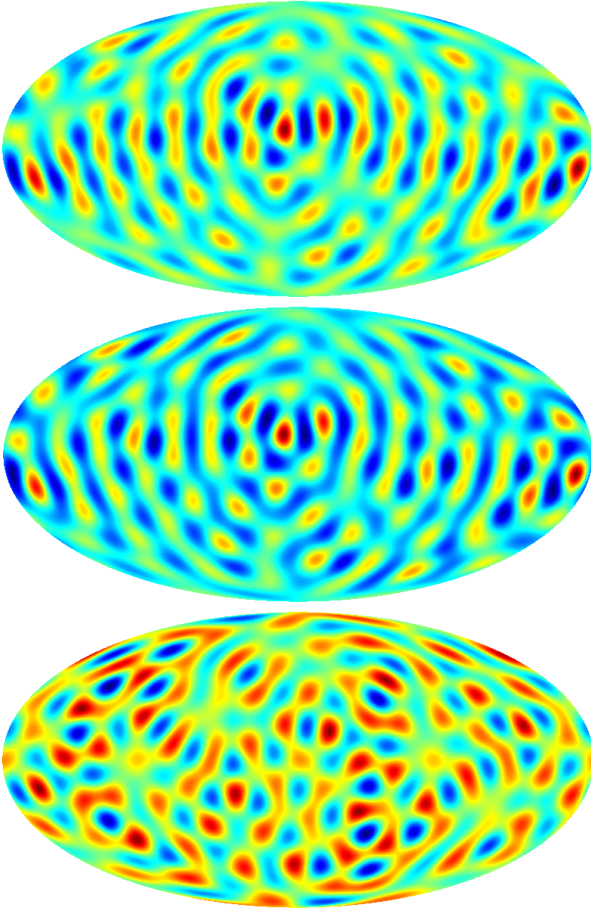


Figure 3.3: (*Top*) Internal linear combination map constructed with $a_{l,m}$ for $l=16$ only. (*Middle*) The TOH Wiener–filtered map with $a_{l,m}$ for $l=16$ only. (*Bottom*) A random-phase realisation of the map including modes with $l=16$ only.

2004b). In such a scenario, the phases in both modes will be correlated to form this flat structure. Unfortunately, as stated before, the statistic is not suitable for studying the quadrupole and the odd modes were excluded in this analysis, so nothing further can be added to this debate.

For the remainder of this section, I will focus on the ILC modes at $l=16$. Specifically, the individual $a_{l,m}$ at this scale will be scrutinised in the hope of determining the modes that are responsible for the structure seen in Figure 3.3. In Figure 3.4, the individual modes are plotted. It appears that not only are the phases non-random but the $|a_{l,m}|$ are also unusual. The magnitude of the $m=15$ and 16 modes are noticeably larger than the other modes. The abnormal nature of the phases is highlighted by the absence of any modes in the bottom right quadrant. It also appears that individual modes can be paired up with another mode that has a similar magnitude and a phase separation

of $\pm\pi$. This is certainly true for the $m=15$ and 16 modes (marked by a square and a circle, respectively). These two modes are investigated further in Figure 3.5. The top set of realisations have $|a_{l,m}|$ taken from the ILC and random phases. The amplitudes are certainly unusual, forming a flat structure (reverse- s -shaped). When all modes bar the $m=15$ and 16 have ILC phases, the middle set of realisations in Figure 3.5, the reverse- s -shaped structure is still seen. However, when these two modes have the ILC phases and the rest of the modes have random phases, the morphology seen in Figure 3.3 is observed. These two modes are crucial to the formation of this rather flat \cap -shaped bar. In the light of the discussion in Section 2.3, this is rather unsurprising. The discussion regarding Figure 2.7 demonstrates that increasing m_{\min} whilst m_{\max} is set to l , leads to a flattening in the \cup -shaped band. Therefore, setting m_{\min} to 15 and m_{\max} to 16 should lead to an almost flat \cup -shaped structure. This structure should be very similar to an upside-down image of Figure 3.3. Indeed, from Section 2.3.3, we see that the reverse of an image can be formed by consecutive phases being separated by $\pm\pi$. The arrangement of the modes in the ILC fits very well with this picture. The $m=15$ and $m=16$ modes are double the magnitude of 13 of the remaining 15 modes (including $m=0$), so the effect of the other modes can be ignored. Moreover, the phases of this pair are separated by $\pm\pi$.

The preceding paragraph demonstrates how the individual modes effect the geometry of the structure at $l=16$. Unfortunately, the nature of these modes offers no further insight into the reason for the structures existence. Whether the structure is due to foreground contamination or not is still debatable. Nevertheless, the potential of the statistic is illustrated. Phase correlations do exist at this scale and these correlations ultimately effect the morphology of the observed structure.

3.4 Conclusions

In this chapter, we developed a new technique that seeks departures from the standard assumption that the CMB represents a homogeneous Gaussian random field. If true, then the phases of the spherical harmonic coefficients should be uniformly random on the interval $[0,2\pi]$. Specifically, we examined the phases and phase differences across even modes from $l=2-20$. A key component of the technique was Kuiper's statistic which can be used to look for evidence of non-uniformity in circular data.

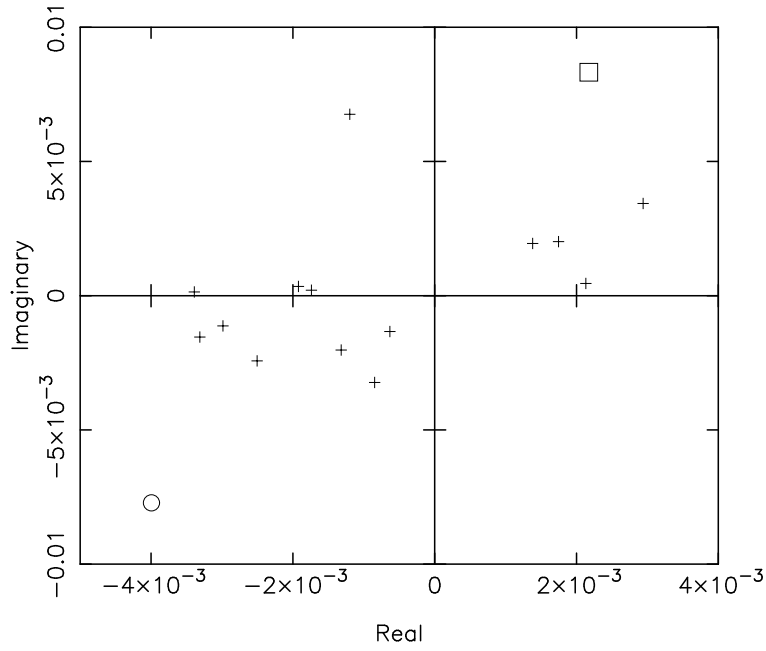


Figure 3.4: The $a_{l,m}$ of the ILC at $l=16$. Crosses signify $m=1-14$, whilst $m=15$ and 16 are marked by a square and a circle respectively

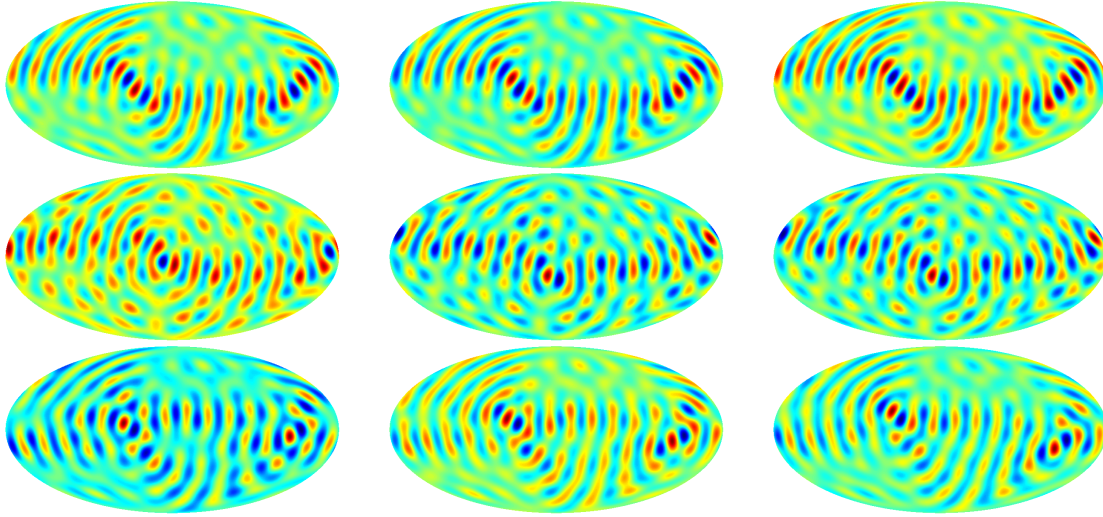


Figure 3.5: The role of individual phases of the ILC at $l=16$. (Top) Realisations with $|a_{16,m}|$ from the ILC and random ϕ_m . (Middle) Realisations with $|a_{16,m}|$ and ϕ_{1-14} from the ILC and random $\phi_{15,16}$. (Bottom) Realisations with $|a_{16,m}|$ and $\phi_{15,16}$ from the ILC and random ϕ_{1-14} .

Firstly, the strengths and limitations of the technique were explored by applying it to two types of model skies. The method successfully picked out skies with non-uniform phases of the sort discussed in Watts, Coles & Melott (2003). However, models with

quadratic non-Gaussian fluctuations were undetectable with the method. These types of skies are non-Gaussian but statistically homogeneous, indicating that the method is better suited to finding features that occupy a substantial part of the sky.

We next looked at data from the COBE–DMR instrument. The scale of $l=10$ was found to have a non-uniform distribution of phases at high confidence. This scale differed to the scale of $l=16$ previously reported as showing signs of non-Gaussianity using the bispectrum (Ferreira, Magueijo & Gorski, 1998). Clearly, different aspects of the DMR data are being highlighted by the bispectrum and our method. This indicates that the pair of statistics are complimentary non-Gaussian tracers.

We then investigated all-sky maps derived from the WMAP 1st-year data. The WMAP team's ILC map had strong signs of non-random phases at $l=16$. The modes at this scale are forming a band-like structure across the Galactic plane. Two modes in particular ($m=15$ and 16) were found to be fundamental in determining the structure's shape. The alignment of the structure with the Galactic region suggests that it may be due to foreground contamination. This is consistent with other independent claims of foreground contamination (Chiang *et al.*, 2003; Naselsky, Doroshkevich & Verkhodanov, 2003; Chiang & Naselsky, 2004; Eriksen *et al.*, 2004b). On the other hand, the structure may be a relic of the partition of the sky during the map-making-process. Such a claim is made stronger by the fact that the one map without sky division, the Naselsky map, showed no signs of peculiar phases at this scale. Finally, the $l=6$ scale was found to have non-random phases, reinforcing recent claims that the scale is unusually planar (Eriksen *et al.*, 2004a).

The issue of foreground contamination will be returned to in chapters 5 and 6.

In this chapter, we have studied one of the simplest forms of phase associations. We will explore another form of phase association in the next chapter. Already, we have seen the technique is useful at pursuing departures from homogeneity in the CMB sky. Such a scenario should exist if the universe has a non-trivial topology. It is to this topic that we now turn our attention.

Chapter 4

Non-random phases in non-trivial topologies

4.1 Introduction

Overall, the 1st–year WMAP observations seem in good accord with the emerging standard cosmological model; a flat Λ –dominated universe seeded by scale–invariant adiabatic Gaussian fluctuations (Spergel *et al.*, 2003). However, at large scales there is an unexpected loss of CMB anisotropy power that was also seen in the COBE–DMR data (Bennett *et al.*, 2003a). One possible explanation is that we inhabit a universe that has a non–trivial topology. That is to say, our universe is in fact multi–connected and has a finite volume. If so, then power on scales exceeding the fundamental cell size will be suppressed. Our space may not be large enough to support long–wavelength fluctuations. A number of authors have tried to restrict the topology of the universe using the WMAP data (Luminet *et al.*, 2003; Uzan *et al.*, 2003; Cornish *et al.*, 2004; de Oliveira-Costa *et al.*, 2004b; Roukema *et al.*, 2004; Weeks *et al.*, 2004). In particular, Luminet *et al.* (2003) have shown that the Poincaré dodecahedral space ($\Omega_o \approx 1.013$) accounts for the measured power in the quadrupole and octopole better than an infinite (simply–connected) flat universe. The angular power spectrum, however, is not an effective way to characterise the peculiar form of the anisotropy manifest in small universes of this type (Levin, Scannapieco & Silk, 1998).

Whether we can determine the topology of the universe depends on its volume. If the

universe is small enough, we should be able to see right around it, since photons can travel across the whole universe. If so, then we may be able to identify ghost images of the same object in different directions in the sky or recognise the topology from signatures in clustering statistics. Luminet & Roukema (1999) provide a review of these methods. However, these methods are hindered by the need to identify good standard candles; objects that can be traced through different eras. This is not a problem when looking at the CMB for signatures of the topology. The CMB photons originate from the same epoch and from a very thin shell, the last scattering surface (LSS), which is the same when viewed from either side. If the physical dimensions of the universe are less than the diameter of the LSS then the sphere self intersects; the loci of self-intersections are circles (Cornish, Spergel & Starkman, 1998). We should therefore be able to match patterns of hot and cold spots around circles. This result holds no matter how complex the topology. A further advantage of using the CMB as an indicator is that the last scattering surface marks the edge of the visible universe, making it a powerful tool for looking for non-trivial topology.

In this chapter, we introduce a new method to search for evidence of a finite universe in all-sky CMB maps. The method is a simple extension of the statistic developed in chapter 3. Again, the technique is based on the properties of the phases of the coefficients obtained from a spherical harmonic expansion of all-sky maps, specifically we exploit phase correlations arising from matched pairs of circles. Whereas in chapter 3, we look solely at correlations between consecutive modes at a particular scale, in this chapter we also seek correlations across different scales. In the next section, I briefly introduce some basic ideas in topology and discuss the simulations with non-trivial topologies used later on. In Section 4.3, I sketch the procedure developed to detect phase correlations in the CMB. In Section 4.4, the results are discussed, after applying the method to the simulations and WMAP data. Conclusions are drawn in Section 4.5.

4.2 Non-trivial topology

Topology deals with connectivity. To a topologist, a coffee cup and a doughnut are equivalent, while a coffee cup and a bowl are distinct. In the cosmological setting, we are concerned with the connectivity of space: a manifold is described as simply-

connected if any closed path can be contracted to a point. The possibility that our universe maybe multi-connected was first suggested by Schwarzschild (1900), but has often been overlooked in favour of the simplicity offered by trivial topological spaces. Indeed there is a common misconception that the shape of the universe can be determined from Einstein's field equations, given a value of Ω_o . General Relativity only specifies the local curvature of space-time, so nothing in it forbids a (global) non-trivial topology. The Cosmological Principle merely restricts us to manifolds with constant curvature. Indeed, any detection of non-trivial topology could determine the sign of the spatial curvature since its characteristics differ for the cases of Euclidean, spherical and hyperbolic manifolds.

A 3-dimensional manifold can be described by identifying faces of a fundamental cell/polyhedron. The WMAP data suggests that the Universe is very nearly spatially flat, with $\Omega_o=1.02 \pm 0.02$ (Bennett *et al.*, 2003a). We therefore restrict our attention to non-trivial topologies with a flat geometry. The technique should nevertheless be applicable to spherical and hyperbolic spaces where matched circles are expected. There are 6 compact orientable flat models that can be constructed either by identifying the sides of a parallelepiped or a hexagonal prism.

- Model 1: The simplest one is the hypertorus (3-torus) which is obtained from a parallelepiped with pairs of opposite faces glued together. In other words this manifold is built out of a parallelepiped by identifying $x \rightarrow x + h$, $y \rightarrow y + b$ and $z \rightarrow z + c$.

The other three manifolds are variations of the hypertorus involving identifications on opposite faces of a twisted parallelepiped.

- Model 2: One of these has opposite faces identified with one pair rotated through π (the twist torus).
- Model 3: the second identifies opposite faces with one rotated by $\pi/2$ (the $\pi/2$ twisted torus).
- Model 4 : the third one is obtained by proceeding with the following identifications: $(x, y, z) \rightarrow (x + h, -y, -z)$ corresponding to translation along x and rotation around x by π ; next $(x, y, z) \rightarrow (-x, y + b, -(z + c))$ corresponding to translation along y and z followed by rotation around y by π ; and finally

$(x, y, z) \rightarrow -(x + h), -(y + b), z + c$ translation along x , y and z followed by rotation around z by π (the triple twist torus).

Two other topologies are built out of a hexagon by identifying the three pairs of opposite sides while in the z direction,

- Model 5: the faces are rotated relative to each other by $2\pi/3$ ($2\pi/3$ hexagon)
- Model 6: and by $\pi/3$ ($\pi/3$ hexagon).

The simulations presented here are based on those in Rocha *et al.* (2004): they have $\Omega_\Lambda=0$ and a Harrison–Zel'dovich Gaussian spectrum. The simulations reflect topologies with equal-sided physical dimensions that lead to a suppression of the quadrupole with respect to the high-order modes (Weeks *et al.*, 2004). We define a dimensionless topological scale j of a simulation as the ratio between the width of the fundamental cell and the horizon size.

These simulations include only those temperature fluctuations generated by the Sachs–Wolfe effect. Matched circles occur because we are looking at the same point on LSS from different directions. In order for this to be true, the temperature fluctuations need to be generated at the LSS which is true in this case, but the SW effect only dominates at large scales. We therefore again limit our investigation to $l \leq 20$. Even at these scales, however, there are three main factors that could confuse the statistic : (i) velocity perturbations generating anisotropies at the LSS; (ii) the integrated Sachs–Wolfe effect due to time varying potential wells crossed by the photons; and (iii) Galactic foreground contamination of CMB data.

4.3 Testing for phase correlations

In this section, the procedure for detecting non-random phases, described earlier in Sections 3.2.1–3.2.3, is briefly outlined with some amendments applicable to this chapter.

The temperature fluctuations in the CMB at any point in the celestial sphere can be expressed in spherical harmonics. In orthodox cosmologies the temperature fluctuations constitute a statistically homogeneous and isotropic Gaussian random field. In this case the phases $\phi_{l,m}$ are independent and uniformly random on the interval $[0, 2\pi]$ and the

variance of a_{lm} depends only upon l . Departures from orthodoxy lead to differences in behaviour of the $a_{l,m}$. For example, in anisotropic Gaussian fluctuations the variance of the $a_{l,m}$ depends on m (Ferreira & Magueijo, 1997b; Inoue & Sugiyama, 2003). In chapter 3, we developed a diagnostic of departures from the standard assumption that involves the randomness of phases. The main component of the technique involved using Kuiper's statistic from an available set of phase angles. First the angles are sorted into ascending order, to give the set $\{\theta_1, \dots, \theta_n\}$. Each angle θ_i is divided by 2π to give a set of variables X_i , where $i=1 \dots n$. From the set of X_i we derive two values S_n^+ and S_n^- (Equations (3.2) and (3.3)). Kuiper's statistic, V , is then defined in Equation (3.4) as

$$V = (S_n^+ + S_n^-) \cdot \left(\sqrt{n} + 0.155 + \frac{0.24}{\sqrt{n}} \right). \quad (4.1)$$

In order to remove any artifact arising from the choice of coordinate frame that the $a_{l,m}$ are measured in, V is calculated for randomly rotated coordinate systems. The rotated coefficients are found by employing the Wigner D function as described in Equation (3.13). That is to say,

$$a_{l,m} = \sum_{m'} a_{l,m'} D_{m,m'}^l(\alpha, \beta, \gamma), \quad (4.2)$$

where the Euler angles α, β, γ are randomly chosen. Consequently, a distribution of V is obtained from one set of angles. This distribution is compared, using a χ^2 test, with distributions obtained in a similar manner from 1,000 Monte Carlo sets of $\phi_{l,m}$ drawn from a uniformly random distribution. The probability $\mathcal{P}(\chi^2)$ of obtaining a lower value of χ^2 is calculated from the fraction of χ^2_{MC} that are less than the χ^2 obtained from the phases. A set of angles is assumed to be non-random if $\mathcal{P}(\chi^2) \geq 0.95$.

The random-phase hypothesis can be further scrutinised by investigating subsets of the phases. These subsets should also be uniformly random on the interval $[0, 2\pi]$. In this chapter, we look at two subsets: (i) the phase differences for fixed values of m ($\phi_{l+1,m} - \phi_{l,m}$) and (ii) the phase differences for fixed values of l ($\phi_{l,m+1} - \phi_{l,m}$) (even l -modes only). The latter subset was also studied in the previous chapter. Both subsets are of particular interest since Cornish *et al.* (2004) indicate that matched circles are associated with phase correlations. In their paper, the significance level for detection of matched circles in the WMAP data is calculated from 'scrambled' versions of the data. In the scrambled versions, phase correlations are removed by randomly exchanging the $a_{l,m}$ at fixed l . Also, as previously mentioned multi-connectedness breaks the global isotropy and sometimes the global homogeneity of the universe (except the case of

the projective space). This will induce correlations between the $a_{l,m}$ of different l and m . For instance, due to the symmetries of the hypertorus case, $\langle a_{l,m} a_{l',m'}^* \rangle \neq 0 \Rightarrow m - m' \equiv 0 \pmod{2}$ and $l - l' \equiv 0 \pmod{2}$ (Riazuelo *et al.*, 2004). These non-zero off-diagonal terms will induce phase correlations as detected in this study.

Overall, for a given temperature map, we obtain a value of $\mathcal{P}(\chi^2)$ for each mode; 18 values for subset (i) and 10 for subset (ii). To improve the presentation of the results, we combine $\mathcal{P}(\chi^2)$ for each subset in two ways. First, we count the number of modes with $\mathcal{P}(\chi^2) \geq 0.95$ and find the mode that displays the highest value. Secondly, we perform a Kolmogorov–Smirnov (K–S) test on the distribution of $\mathcal{P}(\chi^2)$ over the modes. If the phases are random, the set of $\mathcal{P}(\chi^2)$ should be uniform in the interval $[0, 1]$. To quantify the significance of the K–S value obtained, 10,000 MC sets of $\mathcal{P}(\chi^2)$ are generated and the probability of obtaining a lower K–S value is calculated. The reason for doing both these things is that one would expect one in twenty modes to yield a value of $\mathcal{P}(\chi^2) \geq 0.95$. The second approach gives a (very conservative) idea of the significance of the whole set of modes rather than each individual one.

4.4 Results and discussion

The simulations were generated in HEALPix format (Gorski, Hivon & Wandelt, 1999) with a resolution parameter $N_{\text{side}}=32$. The $a_{l,m}$ were derived using the 'anafast' routine in the HEALPix package. V was binned from 0–2.75 and 0–2.5 for subsets (i) and (ii), respectively. Subset (i) required 10,000 rotations in order to obtain stable results. To analyse one realisation took 18 minutes on 1,400 MHz CPU desktop. On the other hand, 3,000 rotations produced stable results for subset (ii), resulting in each analysis taking $2\frac{3}{4}$ minutes on the same desktop.

The six flat models listed in Section 4.2 were studied with $j=0.5$. In order to see the effect j had on the results, the hypertorus was explored in more detail. A further six simulations with $j < 2$ were scrutinised. Also, six simulations in which matched circles are not anticipated ($j \geq 2$) were studied. The results for subsets (i) and (ii) are shown in Tables 4.1 and 4.2 respectively. The tables show the number of modes with $\mathcal{P}(\chi^2) \geq 0.95$, the most non-random mode and the K–S fractional probabilities. For subset (i), the method was applied to five realisations (sets of rotations) of each simulation. The average values obtained from these realisations are shown in the tables.

<i>Map</i>	<i>Count (Mode)</i>	<i>K–S Probability</i>
Model 1 $j=0.5$	0.6	0.68
Model 2 $j=0.5$	1.2 (17)	0.35
Model 3 $j=0.5$	4.6 (4,5)	0.99
Model 4 $j=0.5$	0.6	0.22
Model 5 $j=0.5$	1.8 (14)	0.68
Model 6 $j=0.5$	0.2	0.42
Model 1 $j=0.4$	5.4 (1,4,9,12)	0.99
Model 1 $j=0.6$	0.4	0.63
Model 1 $j=0.8$	0.8	0.35
Model 1 $j=0.9$	0.0	0.56
Model 1 $j=1.0$	0.4	0.47
Model 1 $j=1.6$	3.8 (8,9,10)	0.77
Model 1 $j=2.0$	1.4 (16)	0.43
Model 1 $j=4.0$	0.0	0.66
Model 1 $j=5.0$	2.8 (12)	0.48
Model 1 $j=6.0$	0.0	0.62
Model 1 $j=8.0$	0.6	0.23
Model 1 $j=10.0$	2.1 (12)	0.88
ILC	1.2 (4)	0.55
TOH	0.6	0.28
Eriksen	2.0 (1,4)	0.33
Naselsky	2.2 (2,4)	0.50

Table 4.1: Phase correlations when scanning across fixed m . The column labelled *Count* shows the average number of modes exceeding 95 per cent significance. The column labelled *Mode* gives the mode(s) with greatest significance. The last column shows a rough measure of significance for all modes obtained using a K–S test as described in the text. 18 modes studied in total.

For subset (ii), only one realisation was necessary in order to obtain consistent results.

If the phases are random, the number of modes with $\mathcal{P}(\chi^2) \geq 0.95$ should be 0.9 for subset (i) and 0.5 for subset (ii). From Table 4.1 it is clear that we are finding correlations when scanning across fixed m for most of the simulations (we shall refer to these as m –correlations). The average count for all the simulations displayed in the Table 4.1 is 2.5. The average value is significantly larger than the expected value of 0.9. This contrasts with the average value of 0.7, from Table 4.2, that is only slightly higher than the expected value. From the results, it is evident that no particular mode can be chosen to look for signs of non-randomness in the phases. This is unsurprising, as the correlations would manifest themselves across many modes, whose nature would depend on the location and size of the circles with respect to the observer.

Map	Count (Mode)	K-S Probability
Model 1 $j=0.5$	0	0.17
Model 2 $j=0.5$	1	0.66
Model 3 $j=0.5$	0	0.52
Model 4 $j=0.5$	1	0.45
Model 5 $j=0.5$	0	0.46
Model 6 $j=0.5$	2 (2,12)	0.13
Model 1 $j=0.4$	2 (8,20)	0.32
Model 1 $j=0.6$	0	0.21
Model 1 $j=0.8$	0	0.68
Model 1 $j=0.9$	1	0.97
Model 1 $j=1.0$	1	0.08
Model 1 $j=1.6$	0	0.09
Model 1 $j=2.0$	1	0.49
Model 1 $j=4.0$	1	0.47
Model 1 $j=5.0$	1	0.16
Model 1 $j=6.0$	1	0.54
Model 1 $j=8.0$	1	0.73
Model 1 $j=10.0$	0	0.43
ILC	2 (14,16)	0.50
TOH	3 (6,14,16)	0.77
Eriksen	2 (6,16)	0.80
Naselsky	1 (14)	0.81

Table 4.2: Phase correlations when scanning across fixed l . Columns are as in the previous table. 10 even modes studied in total.

The m -correlations are less obvious in terms of the K-S probabilities. However, this test is more general: it does not search specifically for large values of $\mathcal{P}(\chi^2)$, so it should be interpreted as a very crude measure of departure from uniformity. The K-S test tends to be more sensitive to deviations around the median value of the theoretical cumulative distribution. There are other tests, such as the Anderson–Darling statistic, that are weighted in a fashion that leaves the statistic more sensitive to the tails of the (cumulative) distribution. A variety of statistics that probe non-uniformity (including the Anderson–Darling statistic, χ^2 , Kuiper’s test, and various statistics that incorporate measures of the area below the cumulative distributions) were applied to the values of $\mathcal{P}(\chi^2)$. However, like the K-S test, these statistics all failed to detect any signs of non-uniformity in the distribution. It shows that the specific form of non-uniformity probed by the number count (a peak in the distribution at $\mathcal{P}(\chi^2) \geq 95$), is best suited to seeking the departures seen in the results. In fact this is rather unsurprising: there

Map	Count
Model 1	0.5 ± 0.2
Model 2	1.0 ± 0.9
Model 3	3.4 ± 3.4
Model 4	1.0 ± 0.7
Model 5	1.3 ± 0.8
Model 6	0.8 ± 0.5

Table 4.3: The variation in number count from simulation to simulation. The second column shows the average number of modes (along with the variation). We evaluated 6 simulations with $j=0.5$ for each model.

Map	Count
Model 2	1.6 ± 1.1
Model 3	3.2 ± 3.3
Model 4	1.0 ± 0.5
Model 5	1.0 ± 0.3
Model 6	0.9 ± 0.8

Table 4.4: The variation in number count due to a shift in the location of the observer. The second column shows the average number of modes (along with the variation). We evaluated 6 simulations with $j=0.5$ for each model.

is no information in the low values $\mathcal{P}(\chi^2)$ and applying statistics that encompass these values only dilute the power of the test. Consequently, as well as being a rather simple measure, the number count is also more robust.

The spread in the number count from one realisation to another is quite small (roughly ± 1 for larger values) and an exact value for each simulation can be obtained by increasing the number of realisations. To see if there is any worth in doing this, we looked at five further simulations for each model with $j=0.5$, the results of which are shown in Table 4.3. The standard deviation is very large, with a count of 1.0 being consistent with all the models. This indicates that it would be very difficult to use the method to distinguish between models or to determine the exact topological scale, you could merely indicate the most probable case. These results confirm that the hypertorus and the $\pi/3$ hexagon models, at this scale, do not display any m -correlations in the phases. However, the triple twist torus is detectable from m -correlations. This fact is less clear in Table 4.1, again indicating that the test results vary from simulation to simulation.

Looking at results for the hypertorus displayed in Table 4.1, it is hard to perceive any trend between the number count and the topological scale of the simulation. The m -

correlations are seen both with values of $j < 2$ and $j \geq 2$. Intuitively, one would expect phase correlations when matched circles are present ($j < 2$). In such cases, the number of repeated patterns (circles in the sky) increases with decreasing j , and hence we would expect an increase in number count with decreasing j . This is not seen in the results, although, this may be masked by the number count varying from simulation to simulation for fixed values of j . Applying the statistic to further simulations may reveal such a trend.

On the other hand, the high number count seen at $j \geq 2$ is less easy to explain. Unearthing signs of non-trivial topology beyond the horizon size, suggests the technique potentially is a powerful tool. Diagnostics that hunt for circles in the sky are limited to a maximum value of $j=2$. Our detections beyond the horizon size are by no means serendipitous. Phillips & Kogut (2004) compute the covariance matrix of the $a_{l,m}$ for the hypertorus at various topological scales. They find the off-diagonal terms, that incorporate the phase information, remain prominent even when the width of the fundamental cell is greater than the diameter of the LSS.

Apart from the hypertorus, each of the topologies addressed are not only anisotropic but also inhomogeneous. The question therefore arises whether the results are affected greatly by changes in the position of the observer. We generated simulations with the observer's position shifted within the fundamental cell. For models 2 to 6, five simulations with $j=0.5$ were generated with the observer position shifted by $(0.1x, 0.1x, 0.1x)$ where x is the width of the fundamental cell. The results are shown in Table 4.4. The number count for each model was found to be consistent with those of the centrally located observer displayed in Table 4.3.

A positive detection of m -correlations in CMB data would therefore be indicative of the universe having a non-trivial topology. In order to seek evidence of these correlations in the CMB data, we turned to four of the WMAP-derived maps that were investigated in Section 3.3.4. The temperature maps were all constructed in a manner that minimises foreground contamination and detector noise, leaving a pure CMB signal. The four maps correspond to those released by the WMAP team (Bennett *et al.*, 2003b), Tegmark, de Oliveira-Costa & Hamilton (2003), Naselsky *et al.* (2003), Eriksen *et al.* (2004a) and Naselsky *et al.* (2003). We shall refer to these as the ILC, TOH, Eriksen and Naselsky maps respectively. Again, the results are shown in Tables 4.1 and 4.2. The method was applied to five realisations of each CMB map for subset (i).

In three of the four maps, evidence was found for the sort of phase correlations seen in the simulations. However, all the maps, bar the Naselsky map, display l -correlations that were discussed in chapter 3 which can be explained, at least partially, by foreground contamination. If no m -correlations were seen then this would suggest there is no evidence for non-trivial topology, but a positive detection does leave open the possibility of a non-trivial topology.

4.5 Conclusions

In this chapter, a new method was presented for constraining the topology of the universe. The method relies on utilising phase correlations associated with matched pairs of circles in the CMB sky. We applied the method to various simulations with non-trivial topologies. The method fails to estimate the scale of features it detects and is not good at discriminating between different models. However, this can potentially be overcome by studying more simulations as the results were shown to vary from simulation to simulation. The method is simple, computationally fast and does deliver a clear signature: a positive detection of these m -correlations is clear evidence for non-trivial topology.

With this in mind, the method was applied to four CMB-only sky maps; we found evidence for m -correlations in three of them. However, it would be premature to conclude that there is evidence for non-trivial topology in any of the available CMB temperature map. The WMAP data is preliminary and has already been shown to have a number of unusual properties that are not yet fully understood (Chiang *et al.*, 2003; Eriksen *et al.*, 2004b). Indeed, Eriksen *et al.* (2004a) have pointed out that the techniques used in producing these maps result in a poor reconstruction of the cosmological phases which may interfere with the possibility of detecting correlations of the type discussed here. Nevertheless, with improved data, I believe the method will be a useful tool in determining the shape of the universe. Moreover, the method is based on only the simplest possible measure of randomness in the phase distribution. More sophisticated combinations may allow us to improve the method substantially, perhaps unearthing further signs of non-trivial topology beyond the horizon size.

Chapter 5

Faraday rotation as a diagnostic of Galactic foreground contamination of CMB maps

5.1 Introduction

The microwave sky is dominated by both the cosmic microwave background and foreground emissions. In order to obtain cosmological information from the CMB, it is necessary to separate the different contributions to the sky. Among the foregrounds that may affect CMB observations are Galactic dust, synchrotron and free–free emission, extragalactic point sources and the Sunyaev–Zel’dovich effect due to hot gases in galaxy clusters. Instruments that probe large scales, such as COBE–DMR, are most sensitive to diffuse foreground emission of our galaxy (Gawiser & Silk, 2000). Synchrotron emission associated with the motion of electrons in the Galactic magnetic field dominates at $\nu \lesssim 20$ GHz. Free–free emission is due to electron–ion collisions in the interstellar medium and dominates in the range ~ 25 –70 GHz. Galactic dust grains absorb UV and optical light from the interstellar radiation field and emit the energy in the far–infrared. This foreground dominates at $\nu \gtrsim 90$ GHz. CMB instruments can identify foregrounds by their spectral signatures across a range of frequencies and this leads to attempts at foreground subtraction. Foreground prediction and subtraction will be an important part of future CMB work, especially in polarisation studies where the

contamination is larger in proportion to the CMB signal than for the temperature field (Davies & Wilkinson, 1998; Sazhin, Sironi & Khovanskaya, 2002). It is clearly important to test that foreground modelling and subtraction has been carried out accurately, especially given the evidence that exists already for unusual features on the CMB Sky (e.g. Chiang *et al.*, 2003).

The DMR instrument on board the COBE satellite found primordial temperature fluctuations of order $\Delta T/T = 10^{-5}$ (Smoot *et al.*, 1992). These fluctuations were measured on angular scales larger than 7° . Measurements were made at 3 different frequencies (31.5, 53 and 90 GHz) corresponding to a window where the Galactic emissions are minimum and the CMB intensity peaks. The WMAP mission was designed to make reliable measurements of the CMB down to angular scales of several arcminutes (Bennett *et al.*, 2003b; Hinshaw *et al.*, 2003). The instrument mapped the full sky at five widely separated frequencies (from 23 GHz to 94 GHz). After foreground subtraction the maps produced from both instruments should reveal only cosmological information. However, we have already seen in chapters 3 and 4 that there exists the suspicion that data from these instruments is contaminated by foreground signals.

In this chapter, I show how it is possible to construct an independent probe of foregrounds using measurements of Faraday rotation along lines of sight to extragalactic objects. The layout of the chapter is as follows. In the next section, I give a brief overview of possible foreground contaminations of CMB maps, and explain how they might be correlated with Faraday rotation measures (RM) taken along random lines-of-sight. In Section 5.3, I carry out a simple and robust test to verify that there is a link between the strength of the sources and their location in the sky. In Section 5.4, I explain the non-parametric cross-correlation technique. In Section 5.5, the link is confirmed between the RM values and Galactic foregrounds by determining correlations between the RM catalogue and maps of various contributions, including the survey of Haslam *et al.* (1982) at 408 MHz, synchrotron maps compiled by the WMAP team, as well as dust and free-free maps. I also explore correlations between the RM-values and the temperature field values in the DMR and WMAP data at the location in the sky of the sources to see if there is any evidence of residual contamination in published maps. The conclusions are presented and discussed in Section 5.6.

5.2 Faraday rotation and foregrounds

Faraday rotation measures of extragalactic radio sources are direct tracers of the Galactic magnetic field. When plane-polarised radiation propagates through a plasma with a component of the magnetic field parallel to the direction of propagation, the plane of polarisation rotates through an angle ϕ given by

$$\phi = \mathcal{R}\lambda^2, \quad (5.1)$$

where the Faraday rotation measure is denoted by the symbol \mathcal{R} and measured in rad m⁻² where

$$\mathcal{R} = \frac{e^3}{2\pi m_e^2 c^4} \int n_e B_{\parallel} ds. \quad (5.2)$$

Note that B_{\parallel} is the component of the magnetic field along the line-of-sight direction. The observed RM of extragalactic sources is a linear sum of three components: the intrinsic RM of the source (often small); the value due to the intergalactic medium (usually negligible); and the RM from the interstellar medium of our Galaxy (Brotén, MacLeod & Vallee, 1988). The latter component is usually assumed to form the main contribution to the integral. If this is true, studies of the distribution and strength of RM values can be used to map the Galactic magnetic field (Vallee & Kronberg, 1975). Even if the intrinsic contribution were not small, it could be ignored if the magnetic fields in different radio sources were uncorrelated and therefore simply add noise to any measure of the Galactic field (Frick *et al.*, 2001). In a similar vein, the distributions of RM values have been used to measure local distortions of the magnetic field, such as loops and filaments, and attempts have also been made to determine the strength of intracluster magnetic fields (Kim, Tribble & Kronberg, 1991). In what follows we shall use RM values obtained from a catalogue of extragalactic sources compiled by Brotén, MacLeod & Vallee (1988, updated in 1991) not to attempt mapping the Galactic B -field but to look for statistical correlations over the whole sky.

There are various ways in which rotation measures of external galaxies could be diagnostic of foreground contamination. The most obvious at first sight is Galactic synchrotron. The *magnitudes* of rotation measures of extragalactic sources trace the Galactic magnetic field strength which, in turn, is correlated with the strength of synchrotron emission resulting from the acceleration of electrons in the Galactic magnetic field. The emission is dependent on both the energy spectrum of the electrons,

$N(E)dE$ and the strength of the magnetic field, B . For a power-law distribution of energies of the form

$$N(E)dE = \kappa E^{-\beta} dE, \quad (5.3)$$

the intensity spectrum of the emitted radiation takes the form

$$I(\nu) \propto \kappa B_{\perp}^{\alpha+1} \nu^{-\alpha}. \quad (5.4)$$

The normalisation constant κ is related to the overall number density of electrons, n_e . The intensity spectral index α is related to the index of the energy spectrum β via $\beta = 2\alpha + 1$, but α is expected to vary with both position and frequency (Lawson *et al.*, 1987). Radio surveys at frequencies below 2 GHz are dominated by synchrotron emission (Davies & Wilkinson, 1998) so these have been used to extrapolate this contribution to the higher frequencies at which CMB instruments operate. However, the only complete-sky survey is that of Haslam *et al.* (1982) at 408 MHz. Extrapolating from such a low frequency measurement is prone to problems with zero levels and scanning errors. Moreover, it is known that the spectral index α varies by $\Delta\alpha \simeq 0.5$ (Davies, Watson & Gutierrez, 1996) which could have a big effect on extrapolations over a large frequency range. If the DMR or WMAP data correlate with RM measurements then this may suggest that synchrotron emission has not been completely removed. Our approach is intended to be complementary to the standard extrapolation.

On the other hand, correlation with Galactic synchrotron is not the only possible diagnostic use of rotation measure data, and may indeed not be the most important. Note that, while the formulae for both rotation measure (Equation (5.2)) and synchrotron intensity (Equation (5.4)) both depend on B , the former depends on the line-of-sight component and the latter on the perpendicular component. If the magnetic field were disordered on a relatively small scale one might still expect correlations to exist between the two, but it is certainly possible to imagine field configurations that result in large synchrotron emission but no Faraday rotation (and vice-versa). On the other hand, although free-free emission does not rely upon the presence of a B -field, it does depend on the electron density as does the rotation measure. A correlation between RM and free-free emission is therefore possible even if the field configuration leads to a negligible correlation with synchrotron emission in the observer direction. Dust may likewise be indirectly correlated; this correlation may be further complicated if the dust is aligned in some way with the Galactic magnetic field.

It is not obvious *a priori* which of the potential contaminants would correlate best with the measured RM values nor what the meaning of any measured correlation would be. For example, free-free, synchrotron and dust emission all vary strongly with Galactic latitude. For this reason alone they are expected to correlate with each other. A cross-correlation with RM could therefore, on the face of it, simply be a Galactic latitude effect. On the other hand, such a cross-correlation could instead indicate more complex, smaller-scale spatial association between these foregrounds. We therefore adopt an entirely empirical approach to this question; we return to the issue of Galactic dependence later, in Section 5.5.

5.3 Distribution of rotation measures

Broten, MacLeod & Vallee (1988) present an all-sky catalogue of rotation measures for 674 extragalactic sources (i.e. galaxies or quasars). It is believed that very large RM values do not reflect the contribution of the Galactic magnetic field, but are instead due to the magnetic field in the source or are perhaps simply unreliable determinations of RM (Ruzmaikin & Sokoloff, 1979). The catalogue contained 39 sources where $|\mathcal{R}| > 300 \text{ rad m}^{-2}$; 25 of these are within the Galactic “cut” of the DMR data used in Section 5.5.2 and 27 are within the Kp2 mask region of the WMAP data used later in Section 5.5.3. While noting this complication, it was decided to use the complete sample for this study. The large-valued rotation measures would only be expected to dilute observed correlations if they were entirely intrinsic; further comments on this later are made in Section 5.5.

Our first point of investigation was to look at the distribution of rotation measures across the sky. If we have a set of points on the celestial sphere labelled with some particular characteristic that is independent of the direction on the sphere, any subsample selected using this characteristic should display the same behaviour as the sample as a whole. In particular, any measure of the spatial correlations of the subsample should have the same form as the complete sample (scaled to take into account the smaller sample size). Looking at the clustering characteristics of subsamples of the Faraday rotation measure catalogue can thus indicate whether the RM values for the sources are intrinsic or determined by their spatial positions.

If a point is chosen at random from an ensemble of points on a sphere, then the proba-

bility of finding it has a neighbour located in the solid angle $\delta\Omega$ separated by θ is

$$\delta P = n\delta\Omega[1 + w(\theta)], \quad (5.5)$$

where $w(\theta)$ is the two-point angular correlation function (Peebles, 1980) and n is the number of points per unit solid angle. The function $w(\theta)$ measures the excess probability of finding two points separated by θ above a random poisson distribution. Thus, whilst sitting on one point, the probability of finding a neighbouring point in the range θ to $\theta + \delta\theta$ is given by

$$\delta P = \frac{N-1}{4\pi r^2} \pi r^2 (\sin^2(\theta + \delta\theta) - \sin^2 \theta) [1 + w(\theta)] \quad (5.6)$$

$$\simeq \frac{N-1}{4\pi r^2} 2\pi r \sin \theta \cdot r \delta\theta [1 + w(\theta)] \quad (5.7)$$

$$= \frac{N-1}{2} \sin \theta [1 + w(\theta)] \delta\theta, \quad (5.8)$$

where r is the radius of the sphere and N is the total number of points in the sample. On the other hand, the probability of finding a point in the range θ to $\theta + \delta\theta$ when centred on any point in the sample is given by

$$\delta P = \eta(\theta) \delta\theta, \quad (5.9)$$

where $\eta(\theta)$ is the conditional distribution of neighbour distances. This is merely the summation over all points of the probabilities given by Equation (5.8) and therefore $\eta(\theta)$ and $w(\theta)$ can be related by

$$\eta(\theta) \delta\theta = N \cdot \frac{N-1}{2} \sin \theta [1 + w(\theta)] \delta\theta \quad (5.10)$$

$$\eta(\theta) = \frac{N(N-1)}{2} \sin \theta [1 + w(\theta)]. \quad (5.11)$$

Note that when Equations (5.8) and (5.9) are integrated over all angles they come to N and $N(N - 1)$ respectively.

Owing to the small size of the sample available for this analysis, a simple but robust statistic is needed. We chose the conditional distribution of neighbour distances, $\eta(\theta)$ defined in Equation (5.9). This has the advantage of being closely related to the angular two-point correlation function. The function $\eta(\theta)$ is straightforwardly calculated by determining the angle between the i th source and each remaining source, and repeating the process for every i . The resulting angles were placed in 100 bins of equal width leading to the distribution of $\eta(\theta)$.

The sample was divided into two sets; those with positive RM values (364 sources) and those with zero or negative values of RM (310 sources). We calculated $\eta(\theta)$ for two subsamples: those with positive rotation measures and those with negative ones, giving $\eta^+(\theta)$ and $\eta^-(\theta)$ respectively. The two distributions were compared through Monte Carlo simulations in which the locations of the sources in the sky were maintained, but the RM values were randomly reallocated to the position of the sources. This method ensures the underlying distribution of $\eta(\theta)$ for real and MC samples was the same, but any link between the RM values and spatial position would be severed in the MCs. We extract $\eta^+(\theta)$ and $\eta^-(\theta)$ from each simulation and constructed an average of distribution over 1000 simulations. Since the distributions are binned it is natural to compare MC distributions with the real data to the average distributions via a χ^2 test, using

$$\chi^2 = \sum_i \frac{[\eta(\theta_i) - \bar{\eta}(\theta_i)]^2}{\bar{\eta}(\theta_i)}, \quad (5.12)$$

where $\bar{\eta}(\theta)$ is the average distribution. The larger χ^2 is the less likely the distribution is drawn from the population represented by $\bar{\eta}(\theta)$. The χ^2 statistic obtained from the positive distributions for the MCs and Brotén *et al.* data were ranked (lowest value to highest). The same was done for the statistics obtained from the negative distributions. Thus, the higher the rank of the real data the more likely the rotation measures and positions are correlated.

The distribution $\eta^-(\theta)$ calculated from the Brotén *et al.* catalogue and sample Monte Carlo simulations are shown in Figure 5.1. The distributions of $\eta^+(\theta)$ are not shown, but they behave in a similar fashion. The χ^2 values obtained when comparing both subsamples distributions with the average MC distributions were larger than those obtained by all 1000 MC subsamples. Indeed, Figure 5.1 demonstrates that there are visible differences between the measured distribution and the MC simulations. This demonstrates that the real data show a significant correlation between the sign of rotation measure and the source's spatial location. This fits in with the idea that there is an asymmetry about the meridian about the Galactic centre; a dominance of negative rotation measures at $0^\circ < l^{\text{II}} < 180^\circ$ and positive RM at $180^\circ < l^{\text{II}} < 360^\circ$ (Vallee & Kronberg, 1975; Han *et al.*, 1997) (here we use l^{II} to denote Galactic longitude to avoid confusion with the angular scale l). Furthermore, the average distribution of both subsamples are identical in shape; the peaks and troughs correspond to the same angles. This reinforces the view that both distributions yield similar information. Overall

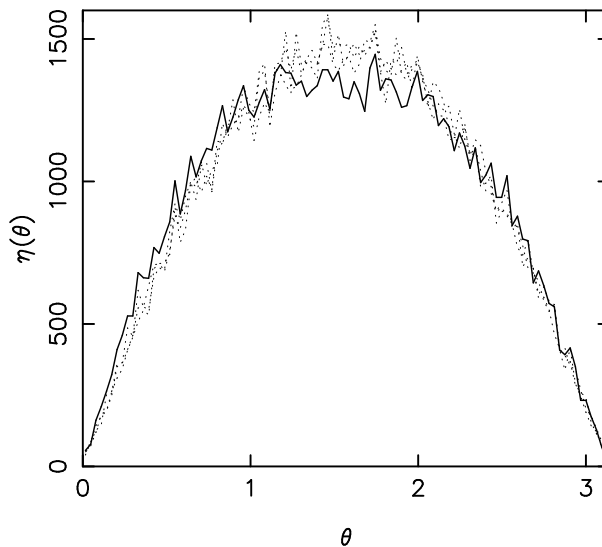


Figure 5.1: Distribution of $\eta(\theta)$ with θ for sources with negative rotation measures. The vertical axis is dimensionless and the horizontal axis is θ in radians. The solid line corresponds to the Broten *et al.* distribution, and the dotted lines show three randomly chosen MC distributions. Note the slight but statistically significant excess at small θ .

the results support the view that rotation measures trace the Galactic magnetic field at the angular location of the source, which is encouraging for this study.

5.4 Correlating rotation measures with sky maps

In order to look for correlation between the temperature measurements and the rotation measures at the locations of the sources we use a non-parametric measure of correlation. The temperature (T_i) at the location of source i and the rotation measure \mathcal{R}_i of source i are drawn from unknown probability distributions. However, if the value of each T_i is replaced by the value of its rank among all the other T_i then the resulting list of numbers will be drawn uniformly from integers between 1 and the sample size N (which is 674 for the whole sample). The same procedure is followed for the \mathcal{R}_i . We are interested in the magnitude of \mathcal{R} as this is determined by the magnetic field strength; the sign is irrelevant to the intensity of emission at that point. If measurements share the same value then they are assigned the mean of the ranks that they would have had if their values slightly differed. In all case the sum of all ranks should be $N(N + 1)/2$, where N is the number of sources.

The Spearman rank-order correlation coefficient is constructed as follows. If x_i is the

rank of T_i among the other T_i 's, and y_i 's is the rank of \mathcal{R}_i among the other \mathcal{R}_i . Then the Spearman rank–order correlation coefficient, r_s is then given by

$$r_s = \frac{\sum_i (x_i - \bar{x})(y_i - \bar{y})}{\sqrt{\sum_i (x_i - \bar{x})^2} \sqrt{\sum_i (y_i - \bar{y})^2}}. \quad (5.13)$$

A perfect positive correlation is represented by $r_s = 1$, whereas $r_s = -1$ is a perfect negative correlation. This is a better statistic than the usual product–moment correlation coefficient because there is no reason to suppose a linear relation between the two variables. In more general terms it is worth stressing that the non–parametric nature of the Spearman test renders it insensitive to highly skewed distributions. What it measures relates to the ordering of the measurements rather than their actual values so the shapes of marginal distributions of x and y are irrelevant.

In order to establish the significance of a non–zero r_s value obtained from comparing the two sets of measurements, the value was compared to those obtained through MC simulations. The simulations were designed such that the temperature field at a particular point was not linked to the rotation measures. However, the sources could not be simply placed randomly in any location the sky since the real data is clustered which may affect the significance level of any result. There are two ways this could have been simulated to take this into account: the rotation measures of the sources could be shuffled, or the coordinate frame of the source positions could be rotated. The former option was chosen as it is computationally faster. We performed 10,000 MCs and a value of r_s was obtained for each one. This allows us straightforwardly to establish the significance level of any measurement in terms of the fraction of simulated r_s values exceeded by the real measurement.

5.5 Application to sky maps

5.5.1 Foreground maps

The idea of using rotation measures to hunt for Galactic contamination in CMB data hinges on the assumption that foregrounds are related (directly or indirectly) with the Galactic magnetic field. As we explained above in Section 5.2, this assumption seems theoretically well–founded but not empirically proven. If the two sets of measurements were found to be uncorrelated, it could be that our understanding of the physics of

foreground emission needs adjusting or that the the main contribution to the integral in Equation (5.2) relates to the Galactic magnetic field might be incorrect. In order to verify that there is indeed a correlation between synchrotron emission and rotation measures we looked at a number of “foreground” maps.

To start with, we looked at 8 “pure” synchrotron maps: three of these are derived from the 408 MHz survey of Haslam *et al.* (1982) and 5 are produced by the WMAP team (Bennett *et al.*, 2003b); maps for the latter (and of the data we use later in this section) are available in HEALPix format (Gorski, Hivon & Wandelt, 1999) from the NASA archive at <http://lambda.gsfc.nasa.gov>. The WMAP maps have a resolution parameter of $N_{\text{side}} = 256$ corresponding to 786,432 pixels. The 408 MHz map has a resolution of 51 arcmin and has been reproduced in HEALPix format with $N_{\text{side}}=128$. We also looked at this survey smoothed to COBE resolution ($N_{\text{side}}=32$). The WMAP team produced their maps using a maximum entropy method (MEM) with the 408 MHz map furnishing a prior spatial distribution; the details of the method are described in Bennett *et al.* (2003b).

The first 8 rows of Table 5.1 summarise the results from these maps. The method identifies weak but highly significant correlations between the rotation measures and the 8 maps. The WMAP-derived maps yield particularly strong signals, with measured r_s values exceeding those in all 10,000 MCs except for the W -band derived case. These strongly significant correlations add weight to the belief of the WMAP team that they have produced synchrotron-only maps for the 5 frequencies. While the 408 MHz map is at such a low frequency that synchrotron emission completely dominates the sky, the WMAP maps are produced at frequencies where the CMB is significant. Furthermore, these maps have been produced by trying to model and remove other sources of contamination (dust and free-free). The r_s values decrease with frequency across the WMAP range. This is not entirely unexpected, because synchrotron emission (see Equation (5.4)) decreases with frequency. On the other hand simply boosting or suppressing the amplitude should not influence the non-parametric correlation if the spatial distribution did not change with frequency. This effect may therefore be an artifact of variations in α .

To explore the possible relationship between free-free radiation and RM values we used two maps: one by Finkbeiner (2003), which is a composite all-sky H α map using data from various surveys, and the other produced by the WMAP team at the K -band

Map	r_s	Correlation Probability
Synchrotron		
408 MHz (Unmasked)	0.267	1.00
408 MHz (COBE resolution)	0.277	1.00
408 MHz (Masked)	0.237	1.00
K -band derived	0.289	1.00
Ka -band derived	0.261	1.00
Q -band derived	0.196	1.00
V -band derived	0.168	1.00
W -band derived	0.094	0.99
Free-Free		
$H\alpha$ (Unmasked)	0.444	1.00
$H\alpha$ (Masked)	0.496	1.00
WMAP MEM (Unmasked)	0.427	1.00
Dust		
FDS model (Unmasked)	0.405	1.00
FDS model (Masked)	0.429	1.00
WMAP MEM (Unmasked)	0.247	1.00

Table 5.1: Significance of correlations of Galactic foreground synchrotron, free-free and dust maps described in the text with the Broten *et al.* Faraday rotation measures.

frequency using the MEM approach mentioned above. Perhaps surprisingly, the results in Table 5.1 demonstrate a stronger correlation between these maps and RM than there is in the synchrotron maps, suggesting that the correlation may relate to regions of where the Galactic magnetic field is largely constant or varies parallel to the line-of-sight but in which the electron density fluctuates. Free-free radiation will depend on the square of the electron density so fluctuations in n_e in a region with constant B may produce larger of correlations of RM of free-free emission than synchrotron.

As far as dust is concerned we again use two maps: one is a map constructed by the WMAP team at 94 GHz using models produced by Finkbeiner, Davis & Schlegel (1999) and the other is produced by the WMAP team using MEM at the W -band frequency. Once again the resulting correlations are significantly stronger than those displayed by the synchrotron maps.

One possible explanation of the free-free and dust results is that the cross-correlation with RM we are seeing is basically an effect of Galactic latitude. If all sources (and B) vary with Galactic latitude then they will correlate with each other. This is possible, but one piece of evidence against this explanation is that if we mask out low Galactic latitudes using the Kp2 mask advocated by Hinshaw *et al.* (2003), the results for synchrotron do not decrease dramatically while those for dust and free-free actually increase slightly.

As a final comment it is worth noting that we repeated the cross-correlation analysis of these maps, excluding the sources in the Brotén *et al.* catalogue that yield very large rotation measures, i.e. $\mathcal{R} > 300 \text{ rad m}^{-2}$. The resulting values of r_s were all slightly reduced by a maximum of about 0.04 in r_s . What is interesting about this result is that it shows that these sources probably do contain some information about the Galactic magnetic field because their RM measures are not entirely intrinsic. If these sources only added noise to the cross-correlation, as we suggested above that they might, then the result on the cross-correlation of excluding them would be random rather than systematic.

5.5.2 COBE–DMR data

The DMR instrument comprised six differential microwave radiometers: two nearly independent channels, labelled A and B, at frequencies 31.5, 53 and 90 GHz. We use data from the region $|b| > 20^\circ$ with custom cutouts near the Galactic centre (Banday *et al.*, 1997). There are 460 sources from the Brotén *et al.* catalogue in this region to compare with the DMR data. The dipole anisotropy of amplitude $\sim 3 \text{ mK}$ is largely removed in pre-map-making process (Banday *et al.*, 2003). We chose to look for correlations in 15 maps from the DMR data: the raw data from each of the six radiometers; the $(A+B)/2$ sum maps and $(A-B)/2$ difference maps for each frequency; and the $(A+B)/2$ sum maps after smoothing with a 7° beam up to $l=20$ using the ‘smoothing’ routine in the HEALPix package. The sum maps should represent the true CMB signal whereas the difference maps should measure the level of instrument noise. The COBE–DMR four year sky maps used for this analysis have a resolution parameter of $N_{\text{side}} = 32$ corresponding to 12,288 pixels in the HEALPix representation.

The results of looking for correlations between the DMR maps and the rotation mea-

<i>Map</i>	r_s	<i>Correlation Probability</i>
31.5 GHz channel A	0.039	0.80
31.5 GHz channel B	0.013	0.61
53.0 GHz channel A	-0.074	0.06
53.0 GHz channel B	-0.024	0.29
90.0 GHz channel A	0.062	0.91
90.0 GHz channel B	-0.031	0.26
31.5 GHz (A-B)/2	0.006	0.56
53.0 GHz (A-B)/2	-0.026	0.29
90.0 GHz (A-B)/2	0.059	0.90
31.5 GHz (A+B)/2	0.017	0.64
53.0 GHz (A+B)/2	-0.045	0.17
90.0 GHz (A+B)/2	0.045	0.83
31.5 GHz (A+B)/2 smoothed	0.056	0.89
53.0 GHz (A+B)/2 smoothed	0.002	0.51
90.0 GHz (A+B)/2 smoothed	-0.048	0.15

Table 5.2: Significance levels of correlations between the DMR maps described in the text and the Brotén *et al.* data.

sures are shown in table 5.2. The sum maps (corresponding to CMB + contaminants) should show the strongest signs of correlations if there are any to be seen. However, none of the maps show any evidence of correlation with the Brotén *et al.* catalogue. In order to see how stable the probability values are, the simulations were repeated for the 90 GHz (A+B)/2 smoothed map a further three times giving probabilities of 0.16, 0.15 and 0.15. This indicates that the probabilities and thus any conclusions drawn from them are valid. Although the main factor may well be the relatively low signal-to-noise in the COBE–DMR data, we can say that our method shows no evidence for any residual foreground component in these maps.

5.5.3 WMAP 1-yr data

The WMAP instrument comprises 10 differencing assemblies (consisting of two radiometers each) measuring over 5 frequencies ($\sim 23, 33, 41, 61$ and 94 GHz). The two lowest frequency bands (K and Ka) are primarily Galactic foreground monitors, while the highest three (Q , V and W) are primarily cosmological bands (Hinshaw

et al., 2003). For CMB analyses, it is necessary to mask out regions of strong foreground emission. Bennett *et al.* (2003b, B03) provide masks for excluding regions where the contamination level is large. The masks are based on the K -band measurements, where contamination is most severe. The masks, of differing levels of severity, are available from the NASA archive. The severity of the mask is a compromise between eliminating foregrounds and maximising sky area in analyses. We chose to use the Kp2 mask used by Hinshaw *et al.* (2003) to calculate cross-spectra from the three high frequency data leading to the angular power spectrum. The mask removes 15 % of pixels (including bright sources) leaving 338 Faraday sources to compare with the maps. There should be no correlations between the rotation measures and the high frequency maps, once the mask has been applied. If there are correlations, this would question whether the amplitude of the angular power spectrum is cosmological in origin.

The WMAP team have also released an internal linear combination (ILC) map that combined the five band maps in such a way to maintain unity response to the CMB whilst minimising foreground contamination. The construction of this map is briefly outlined in Section 3.3.4. Following the release of the WMAP 1 yr data Tegmark, de Oliveira-Costa & Hamilton (2003, TOH) have produced a cleaned CMB map as well as a Wiener filtered map of the CMB. Again, the details of these two maps are sketched in Section 3.3.4. All three maps cover the full-sky and should represent only the CMB signal.

In all, 13 maps derived from the WMAP data were used to seek correlation with the Broten *et al.* catalogue: the five band maps, the five band maps with the Kp2 region removed, the internal linear combination map, and the cleaned and Wiener maps of TOH.

The results of looking for correlations between the WMAP derived data and the rotation measures are shown in Table 5.3. The uncut frequency maps are all significantly correlated with the rotation measures, except the highest frequency map (W -band). This confirms the expected contamination of the data across these frequencies. The strength of correlation decreases with increasing frequency, which may be understood by looking at the contribution of all the foregrounds to the total sky signal across these bands. Combining the contributions of synchrotron, free-free and dust, with synchrotron given a weighting of 0.5 due to its weaker correlation, would reproduce

Map	r_s	Correlation Probability
K	0.292	1.00
Ka	0.189	1.00
Q	0.149	1.00
V	0.126	1.00
W	0.063	0.95
K (with mask)	0.296	1.00
Ka (with mask)	0.099	0.97
Q (with mask)	0.041	0.77
V (with mask)	0.049	0.81
W (with mask)	0.043	0.78
ILC	0.021	0.71
TOH cleaned map	0.059	0.93
TOH Wiener map	0.068	0.96

Table 5.3: Significance levels of cross-correlations derived from various maps originating from WMAP with the Brotén *et al.* catalogue.

this trend. Once the Kp2 mask has been applied, the correlations vanish for all but the K and Ka band map. The reason that a correlation is still found with the K band data is probably that the cut only excludes the very strongest signals so both bands are still heavily contaminated. This is probably not a problem for CMB analysis because these will be projected out in the likelihood analysis. Moreover, the results from the masked maps indicate that calculating the angular power spectrum from the 3 high frequency bands with the Kp2 cut is valid. The contamination from Galactic foregrounds correlated with Faraday rotation on these studies is therefore probably small. Finally, no correlations are found between the rotation measures and two of the CMB-only maps, suggesting that the levels of contamination are indeed low, as the authors claim. Nevertheless, the result from the Wiener filtered map of TOH suggests a correlation at 95% confidence level.

Finally, we mention that on the NASA archive there are maps from each high frequency assembly that are supposedly clean of foreground contaminants outside the Kp2 cut region. The results in Table 5.4 show there are indeed no significant residual correlations in these data when the Kp2 mask is applied.

Map	r_s	Correlation Probability
$Q1$ cleaned	0.005	0.53
$Q2$ cleaned	-0.075	0.08
$V1$ cleaned	-0.008	0.43
$V2$ cleaned	0.023	0.66
$W1$ cleaned	-0.048	0.19
$W2$ cleaned	0.009	0.56
$W3$ cleaned	-0.047	0.19
$W4$ cleaned	0.018	0.63

Table 5.4: Cross-correlations in the “clean maps” from each high frequency assembly

5.6 Discussion and conclusions

The aim of the chapter was to look for traces of Galactic contamination in the COBE–DMR 4 yr data and WMAP 1 yr data using correlations between the maps and the rotation measures of Brotén, MacLeod & Vallee (1988).

Firstly, the relationship between the spatial position and the RM values of the sources in the catalogue were studied by looking at the angular correlations of subsets drawn from it. The results clearly indicate a correlation, and confirm the basic view expressed by other authors on properties of the Galactic magnetic field. We then investigated the relationship between the rotation measure of a source and the synchrotron emission at the location of the source. Synchrotron maps derived from the 408 MHz survey of Haslam *et al.* (1982) and produced by the WMAP team were found to be correlated with RM values, showing that these do indeed provide some sort of probe of the Galactic magnetic field.

We found *stronger* positive correlations of RM values with both dust and free-free maps than for synchrotron. This is consistent with indirect association of the different sources, but is probably not simply a Galactic latitude effect because the correlation persists even when a Galactic cut is applied. Exactly how this correlation arises is an issue for further study, but it may provide an insight into the possible role of spinning dust (Draine & Lazarian, 1998) in Galactic foregrounds (de Oliveira-Costa *et al.*, 1999, 2004a) as this may align with the local magnetic field. Clearly much more detailed modelling is needed to understand these correlations theoretically, but the empirical approach we have adopted still provides a useful consistency check on foreground

analysis even if the origin of the correlation is not well understood.

The correlations between the temperature strength of the DMR and WMAP data at the location of sources and the RM values were then studied using the Spearman rank-order correlation coefficient. All 15 maps compiled from the temperature field measured by the DMR instrument were found to be uncorrelated with the rotation measurements. Correlations were found with the uncut WMAP frequency maps and the cut K and Ka -band maps. However, the maps used by the WMAP team to extract cosmological information were found to be uncorrelated. Furthermore, two foreground-subtracted CMB-only maps were found to be uncorrelated with the rotation measure catalogue. The results of this analysis provide no evidence of residual foregrounds in the COBE–DMR maps or the WMAP ILC map, but do yield a positive correlation for the TOH Wiener–filtered map. Owing to the small size of our RM sample these results are only suggestive, but they do demonstrate the virtue of looking for independent probes of Galactic foreground contamination. Much larger compilations of RM values would be needed to make more definite statements about contamination in temperature maps. It is also very likely that much could be learnt about polarised foregrounds using a similar approach.

Chapter 6

A Faraday rotation template for the Galactic sky

6.1 Introduction

The control of foreground emission is a critical part of CMB analysis. One of the major problems is building accurate templates of the foregrounds at the frequencies where CMB measurements are made. Not only does the strength of the foreground signal vary with frequency, but also the signal varies spatially. This makes it a challenging task to extrapolate foreground measurements of synchrotron and dust from outside frequencies. Even then, we are ignoring the intrinsic uncertainties in the original measurements, ranging from zero-level problems to scanning errors (Barreiro, 2000). The situation is even more bleak regarding free-free emission: the emission only becomes stronger than synchrotron and dust at the very frequencies where the CMB is dominant, $\sim 25\text{--}70$ GHz. Consequently, there are no direct templates of free-free emission available. We have already seen evidence of possible foreground contamination in WMAP-derived data in chapters 3 and 5. Future CMB experiments with higher sensitivity and polarisation measurements will only increase the demand for better foreground controls. Independent tracers could aid in the compilation of these foreground templates. In Section 5.5.1, we found the rotation measures of extragalactic radio sources to be correlated with all three known Galactic foreground components. Ideally, we would like to take a rotation measure and predict the strength of foregrounds emission at a

given frequency. The first step towards such a goal is to build a template for the RM across the whole sky. From this, we can envisage the possible construction of separate templates for the individual components with more sophisticated modelling.

So, what do we intend to do? In this chapter, we attempt to map the RM values as a function of angular position giving $\mathcal{R}(\Omega)$, where we use \mathcal{R} to denote the Faraday rotation measure and Ω for the angular position. Catalogues containing RM values of extragalactic sources are used to construct the function. The observed spatial distribution of the RM values can be expanded over a set of orthogonal basis functions. For analysis of data distributed on the sky, expansion over spherical harmonics seems natural

$$\mathcal{R}(\Omega) = \sum_{l=1}^{\infty} \sum_{m=-l}^{m=+l} a_{l,m} Y_{l,m}(\Omega), \quad (6.1)$$

where the $a_{l,m}$ are the spherical harmonic coefficients and the $Y_{l,m}$ are the spherical harmonics. The properties of the spherical harmonics are well understood and the calculation of the $a_{l,m}$ will allow us to utilise routines within the HEALPix package for visualisation purposes and further analysis. However, a non-uniform distribution of data points compromises spherical harmonic analysis due to the loss of orthogonality (Gorski, 1994). It is more fruitful to analyse a system using orthogonal functions: the statistical properties of the coefficients are simplified. If nonorthogonal functions are used, the properties of the system and the basis are confused. Therefore, we would like to construct an orthonormal basis with functions closely related to those of the spherical harmonics. The spherical harmonic coefficients can then be obtained from the resultant coefficients of the orthogonal basis.

Spherical harmonic analysis of extragalactic sources has been previously performed by Seymour (1966, 1984). However, the analysis was carried out using a different form of orthogonalisation and only on a set of 65 sources.

The RM map resulting from our method will be a useful tool for probing Galactic magnetic structure. Crucially, the map will also be a valuable point of reference when investigating mechanisms that involve the Galactic magnetic field. This includes the CMB foregrounds (synchrotron, dust, free-free emission) that we have already shown to be correlated with rotation measures. There is evidence of another foreground component (de Oliveira-Costa *et al.*, 2004a), labelled foreground X, that is spatially correlated with $100\mu\text{m}$ dust emission. Spinning dust grains (Draine & Lazarian, 1998)

are the most popular candidates for causing this anomalous emission. A RM map can provide insight into the role of these grains as they may align with the local magnetic field. Foreground removal will be particularly challenging in CMB polarisation studies as foregrounds are more dominant than in the temperature anisotropies. Another aspect of CMB research where a RM map would be beneficial is in single frequency polarisation measurements. These measurements will not be able to remove the effects of Faraday rotation through the Galactic magnetic field. Thus, the extent to which the results have been affected by the *E*-mode signal rotating into the *B*-mode signal (and vice versa) is unknown.

The layout of the chapter is as follows. I sketch in the next section the current views and methods used to explore large-scale magnetic fields. In section 6.3, I describe the three rotation measure catalogues used in our analysis. In Section 6.4, I illustrate a method to generate orthonormal basis functions for each catalogue. From the coefficients of the new basis, the spherical harmonic coefficients are calculated. In Section 6.5, I present the resulting RM maps and discuss the observed features. A brief application of the maps is given in Section 6.6. Correlations are sought between the RM maps and cleaned CMB-only maps. The conclusions are presented and discussed in Section 6.7.

6.2 Large-scale magnetic fields

In this chapter, we aim to generate rotation measure maps that hopefully trace the Galactic magnetic field. However, first of all, I wish to outline our current understanding of large-scale magnetic fields.

The origin of large-scale magnetic fields observed on galactic and cluster scales is unknown. The magnetic fields, with observed strengths of $\sim 10^{-6}$ G, could be the consequence of an amplification of a tiny seed ($\lesssim 10^{-20}$ G) by a dynamo mechanism. Alternatively, the compression of a primordial seed ($\sim 10^{-9}$ G) by protogalactic collapse could lead to the fields we see today. Both scenarios require an initial primordial field. Furthermore, the two mechanisms need to explain the high redshift magnetic fields observed in galaxies (Kronberg, Perry & Zukowski, 1992) and damped Lyman- α clouds (Wolfe, Lanzetta & Oren, 1992). Magnetic fields play a crucial role in star formation as well as possibly playing an active role in galaxy formation as a whole (Wasserman, 1978; Widrow, 2002). Thus, one of the most significant tasks in cosmol-

ogy is unravelling the mystery behind magnetic fields; from the primordial field to our own Galactic field.

The CMB provides us with the most distant and extensive probe of the early universe. A primordial magnetic field will leave an imprint in this radiation. Various methods have been developed that seek these signatures. Barrow, Ferreira & Silk (1997) use the anisotropic expansion caused by the presence of a homogeneous primordial field to place limits on its size from large-angle CMB measurements. Others have sought correlation between different scales in the temperature anisotropies (Chen *et al.*, 2004; Naselsky *et al.*, 2004) or computed the effects the field has on the polarisation–temperature cross–correlation (Scannapieco & Ferreira, 1997; Lewis, 2004). The existence of a magnetic field at last–scattering also leads to a possible measurable Faraday rotation of the polarised CMB light (Kosowsky & Loeb, 1996).

At the other end of the scale, investigation of our own Galaxy’s magnetic field has led to the development of a number of different techniques; Han (2004) provides a concise review of the subject. Techniques include observing Zeeman splitting, polarised starlight, synchrotron radiation, Faraday rotated light and polarised dust emission. However, even with all these methods, there are still outstanding problems. This has led to a lack of consensus on key issues: from the number of spiral arms; how the arms are connected; to the direction the field takes along the arms (Vallee, 1997; Han, 2004).

To fully understand magnetic fields, we need a coherent picture throughout different epochs. Theories and models can then be tested against this observational picture. A rotation measure map of the full sky has the potential to fulfil such a goal. RM values probe the integral of the magnetic field from the radiation source to the observer. Obviously, the information encoded in such a map depends on the location of the radiation that is rotated. Faraday rotated polarised CMB radiation will offer both a picture of the primordial field (at the surface of last scattering) and that of our Galaxy. The recent detection of CMB polarisation by DASI (Kovac *et al.*, 2002) and confirmation of this via the WMAP (Kogut *et al.*, 2003), have opened up a new avenue in CMB research. Future results from WMAP and Planck satellites will offer polarised data covering the full-sky over a range of frequencies (seven in the case of Planck). By forming a RM map with the data and looking at differing scales, we should be able to untangle the information in the data; on the largest scales the local magnetic field can be studied,

whereas the primordial field can be studied on the smaller scales.

On the other hand, one of the main tools for probing local magnetic fields (such as our Galaxy's) involves utilising RM values from extragalactic sources. Catalogues containing RM values of extragalactic sources have been used to map the Galactic field (eg. Frick *et al.* (2001)). Combining this data with rotation measures from pulsars that are located within our Galaxy, it is conceivable that a 3-dimensional image of the Galactic magnetic field can be built. However, current RM catalogues are both sparsely populated and unevenly sampled. Thus, astute methods are required to produce a RM map with the data at hand. It is with this in mind, that we proceed with the development of a technique for generating RM maps.

6.3 Rotation measure catalogues

Faraday rotation measures of extragalactic radio sources are direct tracers of the Galactic magnetic field. The nature and uses of rotation measures are described in detail in Section 5.2. In what follows we shall use RM values obtained from three catalogues in an attempt to map $\mathcal{R}(\Omega)$ over the whole sky. All three catalogues are sparsely populated and have non-uniform distributions. It is essential to remove the structure due to the spatial distribution of the sources. This structure is unique to each catalogue. Therefore, for each catalogue a new set of orthonormal functions has to be generated.

The three catalogues used are those of Simard-Normandin, Kronberg & Button (1981, hereafter S81), Broten, MacLeod & Vallee (1988, updated 1991, B88) and Frick *et al.* (2001, F01). S81 present an all-sky catalogue of rotation measures for 555 extragalactic radio sources (ie. galaxies and quasars). B88 and F01 contain 674 and 800 sources respectively. B88 was used in chapter 5 to look for statistical correlations between CMB observations and a RM sample. In F01, the two other catalogues are combined with smaller studies of specific regions in the sky (see paper for details). They also provide slightly reduced versions of the other two catalogues. Sources with significantly larger RM values than those in the other studies are removed, leaving catalogues of 551 sources for S81 and 663 for B88. In our analysis we will use these versions of the two catalogues.

Finally, we reject sources with $\mathcal{R} > 300 \text{ rad m}^{-2}$. Such large RM values are unlikely to

represent real features of the Galactic magnetic field: they perhaps arise from incorrect determination of \mathcal{R} due to the $n\pi$ ambiguity in polarisation angle; magnetic fields within the sources; Equation (5.1) being incorrect; and so on. This final selection criteria reduces the catalogues to 540 sources for S81, 644 for B88, and 744 for F01.

6.4 Generating a new basis

We can only observe RM values where there happens to be a line of sight. This means we see the RM sky through a peculiar “mask”. We wish to generate a new orthogonal basis that takes account of the spatial structure of this mask. In particular, we need to find a set of functions that are orthogonal on the incomplete sphere. Ideally, these new functions should be related to the spherical harmonics (which are orthogonal functions on a complete sphere). This will enable us to determine the spherical harmonic coefficients from the new functions and their coefficients.

Gorski (1994) tackles the problem from the point of view of CMB analysis. The determination of the angular power spectrum is a crucial element of much work in the field. If the temperature anisotropies form a Gaussian random field then they can be completely characterised by the angular power spectrum. In order to obtain the angular power spectrum, one needs to estimate the spherical harmonic coefficients. At low Galactic latitudes ($b < 20^\circ$) foreground contamination is severe. Therefore, it is preferable to obtain an estimate of the spherical harmonic coefficients outside this region. Gorski (1994) calculates a new set of functions that are orthogonal to this cut sphere. These functions are used to calculate the spherical harmonic coefficients and thus estimate the angular power spectrum from the two–year COBE–DMR data (Bennett *et al.*, 1994).

In order to see how the method works it is prudent to look at the definition of orthogonal functions. Let us consider two complex functions $A(x)$ and $B(x)$. If

$$\int_a^b A^*(x)B(x) dx = 0, \quad (6.2)$$

then $A(x)$ and $B(x)$ are orthogonal over on the interval $\{a, b\}$. If we incorporate these two functions into a vector $\mathbf{v}=[A(x), B(x)]$, the orthogonality of the functions can be

expressed through the scalar product

$$\langle \mathbf{v} \cdot \mathbf{v}^T \rangle_{\{a,b\}} = \mathbf{I}. \quad (6.3)$$

We shall now look at orthogonal functions in the context of a complete sphere. A function can be described by spherical harmonics $Y_{l,m}(\Omega)$ up to an order l_{\max} . We can form an $(l_{\max}+1)^2$ -dimensional vector $\mathbf{y} = [Y_{0,0}(\Omega), Y_{1,-1}(\Omega), Y_{1,0}(\Omega), Y_{1,1}(\Omega), \dots, Y_{l_{\max},l_{\max}}(\Omega)]$. The scalar product is then defined as

$$\langle \mathbf{y} \cdot \mathbf{y}^T \rangle_{\{\text{full sky}\}} = \mathbf{I}. \quad (6.4)$$

The sky can therefore be fully described by

$$\mathcal{R}(\Omega) = \sum_{i=1}^{(l_{\max}+1)^2} a_i Y_i(\Omega) \equiv \mathbf{a}^T \cdot \mathbf{y}. \quad (6.5)$$

However, when the sphere is incomplete due to a Galaxy cut or a more complex mask being applied, we have

$$\langle \mathbf{y} \cdot \mathbf{y}^T \rangle_{\{\text{cut sky}\}} = \mathbf{W} \neq \mathbf{I}, \quad (6.6)$$

where \mathbf{W} is the coupling matrix. A new basis, where the equality is true, can be constructed in the following manner. The procedure is a type of Gram–Schmidt orthogonalisation. \mathbf{W} can be Choleski-decomposed into a product of a lower triangular matrix \mathbf{L} and its transpose

$$\mathbf{W} = \mathbf{L} \cdot \mathbf{L}^T. \quad (6.7)$$

The inverse matrix $\Gamma = \mathbf{L}^{-1}$ is then computed. The new set of functions on the cut sky is

$$\psi = \langle \Gamma \cdot \mathbf{y} \rangle_{\{\text{cut sky}\}}. \quad (6.8)$$

By construction, we have

$$\begin{aligned} \langle \psi \cdot \psi^T \rangle_{\{\text{cut sky}\}} &= \Gamma \cdot \mathbf{y} \cdot \mathbf{y}^T \cdot \Gamma^T \\ &= \Gamma \cdot \mathbf{L} \cdot \mathbf{L}^T \cdot \Gamma^T \\ &= \mathbf{L}^{-1} \cdot \mathbf{L} \cdot \mathbf{L}^T \cdot (\mathbf{L}^{-1})^T \\ &= \mathbf{I}. \end{aligned} \quad (6.9)$$

This can be a useful cross-check for testing the code. Finally, the new basis functions can be used to describe \mathcal{R}

$$\mathcal{R}(\Omega) = \sum_{i=1}^{(l_{\max}+1)^2} c_i \Psi_i(\Omega) \equiv \mathbf{c}^T \cdot \psi. \quad (6.10)$$

At this point, only the angular positions Ω_n of the sources have been required. In order to obtain the coefficients c_i of the new basis, the rotation measure \mathcal{R}_n themselves are required. It is worth putting it into the context of the data we have. Let the number of sources in our catalogue be N and let $(l_{\max} + 1)^2 = M$. It should be evident that we have a set of simultaneous equations which have to be solved in order to obtain the coefficients of the new basis functions

$$\begin{aligned}\mathcal{R}(\Omega_1) &= c_1\psi_1(\Omega_1) + c_2\psi_2(\Omega_1) + \dots + c_M\psi_M(\Omega_1) \\ \mathcal{R}(\Omega_2) &= c_1\psi_1(\Omega_2) + c_2\psi_2(\Omega_2) + \dots + c_M\psi_M(\Omega_2) \\ &\vdots \quad \vdots \\ \mathcal{R}(\Omega_N) &= c_1\psi_1(\Omega_N) + c_2\psi_2(\Omega_N) + \dots + c_M\psi_M(\Omega_N).\end{aligned}\tag{6.11}$$

So, as long as $N > M$, these equations should be solvable. Ultimately, we wish to obtain the spherical harmonic coefficients $a_{l,m}$. Using Equation (6.8), we see

$$\mathcal{R} = \mathbf{a}^T \cdot \mathbf{y} = \mathbf{c}^T \cdot \boldsymbol{\psi} = \mathbf{c}^T \cdot \boldsymbol{\Gamma} \cdot \mathbf{y}\tag{6.12}$$

and therefore

$$\mathbf{a}^T = \mathbf{c}^T \cdot \boldsymbol{\Gamma} \rightarrow \mathbf{a} = \boldsymbol{\Gamma}^T \cdot \mathbf{c}.\tag{6.13}$$

So, we have obtained the spherical harmonic coefficients.

There are some practical points that have been glossed over in the above description of the method. Firstly, the RM values in the catalogues need to be smoothed. Otherwise, as the series in Equation (6.10) is finite, we will be attempting to fit large-scale waves to small-scale features. Ideally, the smoothing will take place in the new basis, however, this is impractical. Therefore, we chose to smooth in harmonic space. Around each source, a hoop of 20° is thrown and the average RM value is taken of the sources within the hoop. This could have been done via a more sophisticated method, say a Gaussian-weighted mean of RM values. However, we chose to use the simple approach. The size of the hoop was chosen to match l_{\max} (~ 16) closely in angular size. Furthermore, it coincided with the limiting resolution of the wavelet method used in Frick *et al.* (2001) on the same catalogues.

Secondly, we need to determine to what order we take the series up to, i.e. the value of l_{\max} . We do this through trial and error. As we will expand upon in the next section, RM maps were generated for l_{\max} values of 8, 10, 15, 16, 17 and 18. The power spectrum for each map was studied. At some limiting value of l_{\max} the shape at low l

alters as features become unstable. Maxima and minima points explode since we are trying to fit more and more function to the same amount of data. That is to say, N is getting too similar to M .

Finally, the convention for spherical harmonics has to be chosen carefully. The new basis functions were calculated using the convention of Gorski (1994) where

$$Y_{l,m}(\theta, \phi) = \sqrt{\left(\frac{2l+1}{2}\right)} \sqrt{\left(\frac{(l-|m|)!}{(l+|m|)!}\right)} P_l^{|m|}(\cos \theta) f(\phi) \quad (6.14)$$

and $f(\phi) = \pi^{-1/2} \cos(m\phi)$, $(2\pi)^{-1/2}$, or $\pi^{-1/2} \sin(|m|\phi)$ for $m > 0$, $= 0$, or < 0 . The spherical harmonic coefficients can then be trivially converted into those that adhere to the HEALPix definition of the harmonics where now $f(\phi) = (2\pi)^{-1/2}[\cos(m\phi) + i \sin(m\phi)]$ or $(-1)^m (2\pi)^{-1/2}[\cos(m\phi) + i \sin(m\phi)]$ for $m \geq 0$ or < 0 . The convention of Gorski (1994) was chosen since the information within the coefficients is more highly compressed. Whereas in the HEALPix definition, the coefficient are complex with a symmetry between $+m$ and $-m$, those following the convention of Gorski (1994) are real and contain no such symmetry. The redundant information in the HEALPix coefficients leads to confusion when solving Equation (6.11).

6.5 All-sky RM maps and their interpretation

For all three catalogues, sets of spherical harmonic coefficients were calculated with l_{\max} being set to 8, 10, 15, 16, 17 and 18. From these coefficients, RM maps were produced using the 'synfast' routine in the HEALPix package. To see whether a RM map was displaying real features or whether the series expansion had been extended too far, we looked at the angular power spectrum of each map. The angular power spectrum is the harmonic space equivalent of the autocovariance function in real space. It is defined as

$$C_l = \frac{1}{2l+1} \sum_m |a_{l,m}|^2. \quad (6.15)$$

The spectra of the RM maps are shown in Figure 6.1. For all three catalogues, it is clear that the shape of the spectra is consistent up to $l_{\max} = 16$. Extending the series expansion to higher values of l_{\max} leads to fluctuations in the power on the largest-scales (low l). The method finds it harder to reconcile the data with the increasing number of basis functions. The result is that maxima and minima explode as too much

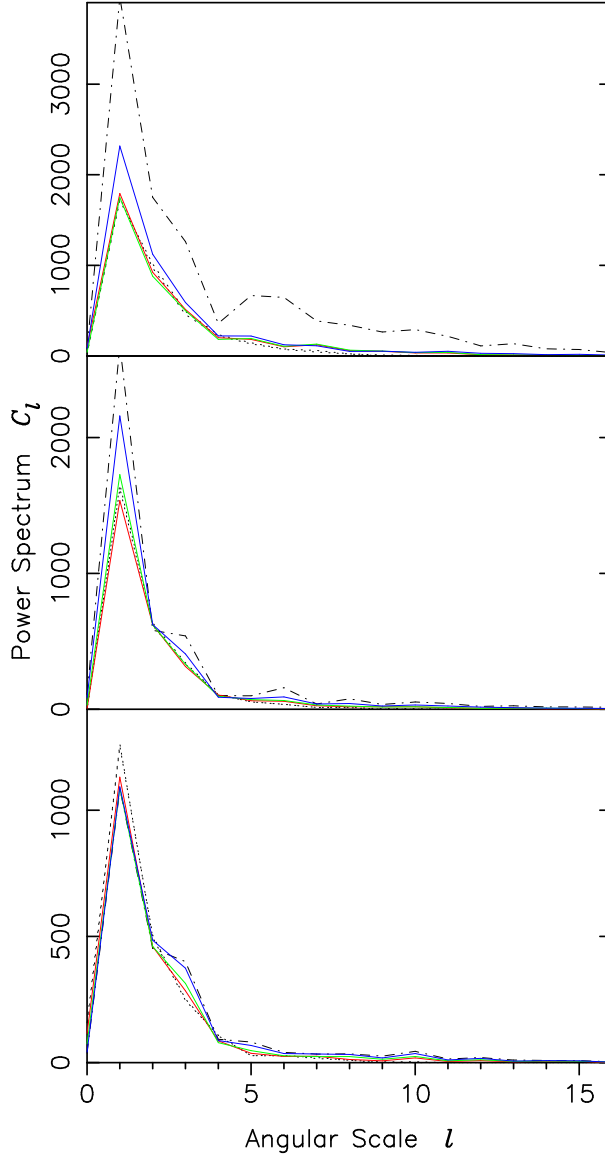


Figure 6.1: Power spectra. Red $l_{\max}=15$, green $l_{\max}=16$, blue $l_{\max}=17$, dotted $l_{\max}=8$ and 10, and dash-dot $l_{\max}=18$. From *top* to *bottom*: S81, B88 and F01 catalogues.

freedom is given. This is clearly visible in the maps for $l_{\max}=17$ and 18 (not displayed). Although looking at the bottom sets of spectra for F01, we see the spectra for $l_{\max}=17$ is consistent until the octopole ($l=3$) where it spikes. This suggest that due to the larger data size of F01 it is more able to cope with the demands of increasing the series expansion. Therefore, at times throughout this section, we will focus our analysis on the RM map from the F01 catalogue with $l_{\max}=16$.

In Figures 6.2, 6.3 and 6.4, we show the RM maps for the S81, B88 and F01 catalogues, respectively. We display only the $l_{\max}=10$ and 16 maps in order not to overload

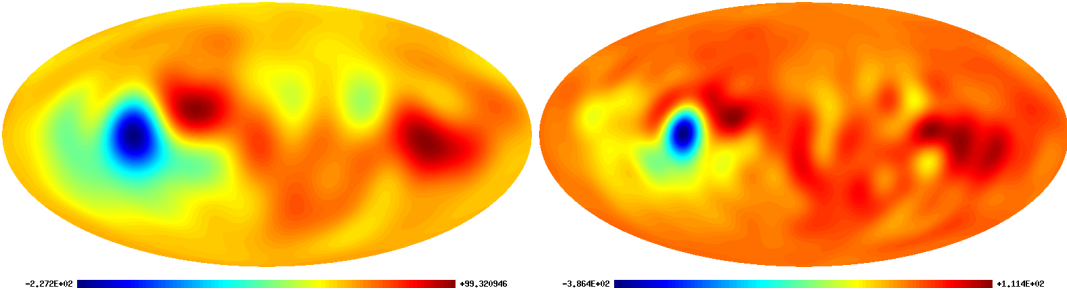


Figure 6.2: S81 catalogue with 540 sources. (Left) $l_{\max} = 10$. (Right) $l_{\max} = 16$.

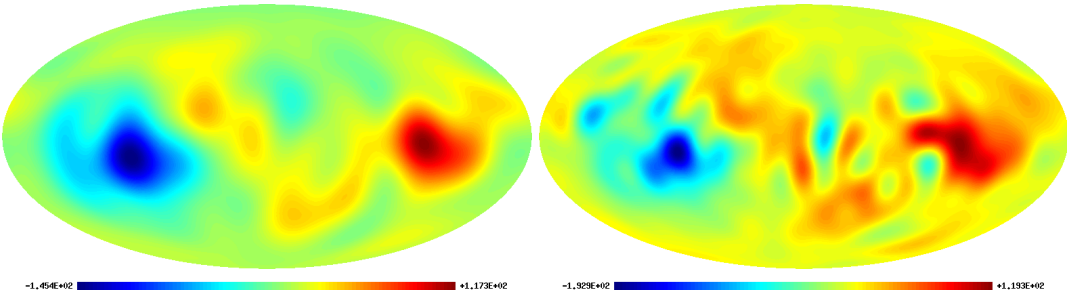


Figure 6.3: B88 catalogue with 644 sources. (Left) $l_{\max} = 10$. (Bottom) $l_{\max} = 16$.

the reader with information. The r.m.s. values of \mathcal{R} for the S81, B88 and F01 RM maps ($l_{\max}=16$) are 26.4, 23.5 and 21.5 rad m⁻², respectively. Maxima (large positive \mathcal{R}) are red, whereas, minima (large negative \mathcal{R}) are blue. The two limiting scales enable us to see the progress of structure as the series expansion is extended to include higher modes. We can observe how feature at small l develop as the series extends. Reassuringly, the main features in the $l_{\max}=16$ maps are also present in the $l_{\max}=10$ maps. The positions of the maxima and minima remain roughly unchanged. This is compelling evidence that the observed features are real. However, comparison of the maps from the three catalogues is inhibited by the temperature-colour scale varying from map to map. Therefore, for the $l_{\max}=16$ maps, we force the maximum and minimum scale to

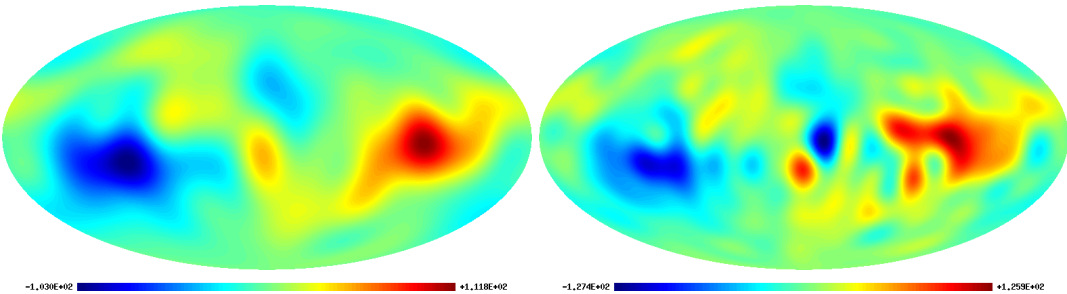


Figure 6.4: F01 catalogue with 744 sources. (Left) $l_{\max} = 10$. (Bottom) $l_{\max} = 16$.

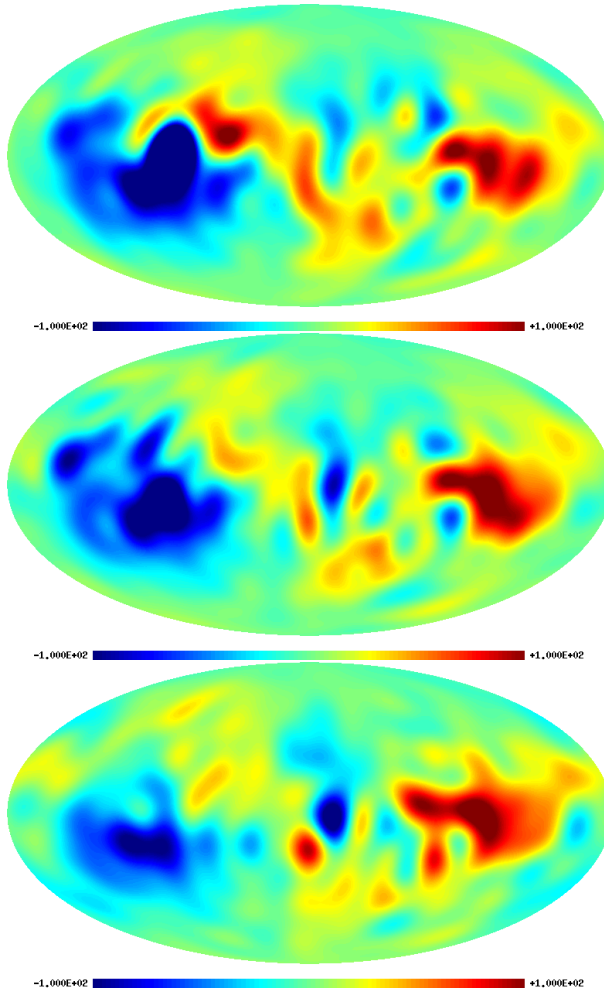


Figure 6.5: RM maps with identical temperature–colour scaling ($l_{\max} = 16$). From *top* to *bottom*: S81, B88 and F01 catalogues.

be $|\mathcal{R}| = 100 \text{ rad m}^{-2}$; the results of which are shown in Figure 6.5.

From Figure 6.5, it is clear that the maxima at $l^{\text{II}} \sim 270^\circ$ and minima at $l^{\text{II}} \sim 90^\circ$ are the dominant features in all three plots (again we use l^{II} to denote Galactic longitude to avoid confusion with the angular scale l). This maxima/minima pair corresponds to the large-scale magnetic field in the local Orion spur (sometimes referred to as an arm). These two spots are displaced from the equator to negative Galactic coordinates. This asymmetry between the two hemispheres has been widely reported before (eg. Vallee & Kronberg, 1975; Frick *et al.*, 2001); it is usually attributed to the local radio Loop I (the North Galactic spur). Such local distortions are associated with interstellar magnetised superbubbles with typical diameters of 200 pc (Vallee, 1997). There is also a prominent maxima/minima pair towards the Galactic centre in the RM map formed

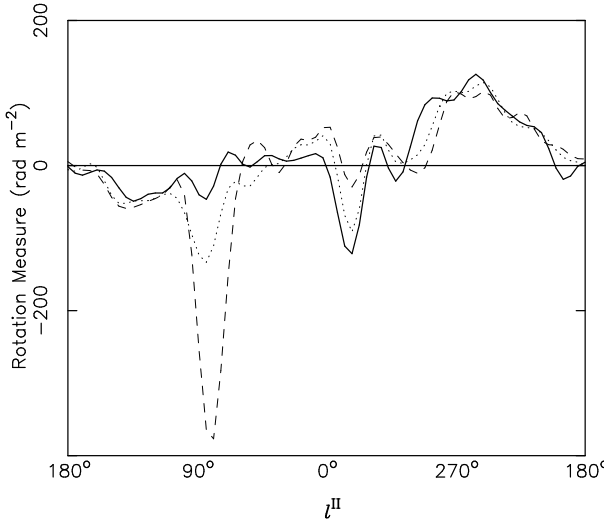


Figure 6.6: Galactic equator cross-section ($l_{\max} = 16$). *Dashed*: S81 catalogue; *Dotted*: B88 catalogue; and *Solid line*: F01 catalogue

from the F01 catalogue. The centres of the maxima and minima are at $l^{\text{II}} = 1^\circ$ and $l^{\text{II}} = 346^\circ$, respectively. On closer inspection, this feature is present in the RM maps from the other two catalogues. Finally, in the S81 RM map, there is a strong maxima at $l^{\text{II}} \sim 50^\circ$ in the northern hemisphere. This feature is only suggested in the other two maps.

Cross-sections, along the Galactic equator, were taken of the RM maps ($l_{\max}=16$) in order to further understand the features. These are shown in Figure 6.6. Ideally, with such a slice, maxima/minima locations should indicate the tangential direction to spiral arms and directional field changes should correspond to $\mathcal{R} = 0$. However, local distortions and flaws in the map-making process, make this not entirely true. The Orion spur location is clear for all three maps. Furthermore, the maxima/minima pair towards the Galactic centre (described in the previous paragraph) is evident in all three cross-sections. However, the picture is hazy from $l^{\text{II}}=30-50^\circ$: there is clear field reversal in S81 map; a hint of a reversal in F01 map; and none in B88 map. The maxima and minima in the cross-sections could be attributed to the named inner arms (eg. the minima near the Galactic centre to the Norma arm), however, this seems quite speculative given the variation from catalogue to catalogue.

It is clear that the Orion spur is the dominant feature. Since the associated maxima/minima pair is separated by 180° , it will be the main source of the dipole ($l=1$). Moreover, we see from the spectra that the quadrupole ($l=2$) is also strong. There-

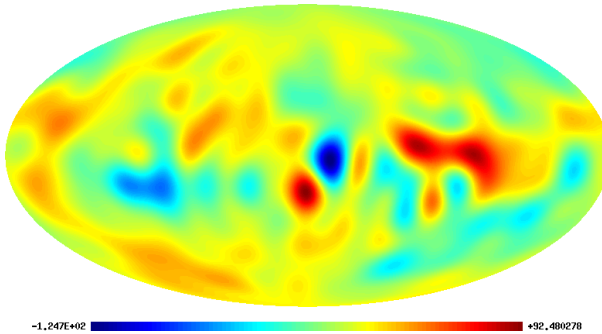


Figure 6.7: F01 catalogue with both the dipole and quadrupole removed ($l_{\max} = 16$).

fore, we remove both the dipole and quadrupole from the RM map ($l_{\max}=16$) compiled from the F01 data. The results of which are displayed in Figure 6.7. This enable us to view some of the smaller scale features. These details will be hard to explain solely from Galactic magnetic field models. It will be interesting to see, if these small-scale features persist with larger data sets.

A study of the global Galactic magnetic field structure would benefit from the removal of local distortions. Consequently, we applied the method with the region containing Loop I removed ($b > 0^\circ$, $0 < l^{\text{II}} < 40^\circ$, $270 < l^{\text{II}} < 360^\circ$) (Ruzmaikin & Sokolov, 1977). However, the removed segment was too large to successfully reconstruct the sky given the remaining sources. The lack of restrictions in the segment meant large maxima/minima formed there. This highlights one disadvantage of spherical harmonic analysis over wavelet analysis that can be localised in both physical and wavenumber spaces. The removal of these local structures is useful for getting a clear picture of the Galactic magnetic field. In CMB foreground studies, however, these structures are essential components of a template.

6.6 Correlations with CMB maps

As mentioned in the introduction to this chapter, RM maps have a general importance beyond trying to map the Galactic magnetic field. In what follows, we hope to display one particular function. In this section, we focus solely on the RM map produced from the F01 catalogue with l_{\max} set to 16. In chapter 5 we developed a diagnostic of foreground contamination in CMB maps. The method measured the cross-correlation between the RM of extragalactic sources and the observed microwave signals at the

same angular position. In what follows, we seek correlations between the spherical harmonic modes of the RM map and CMB–only maps. In doing so, we shall look at the phases of the coefficients of the modes from $l=2$ to $l=16$. Phase correlations were used in chapter 3 to hunt for evidence of departures in the CMB temperature field from a Gaussian random field. In chapter 4.1 a certain form of phase correlation was found to be associated with non–trivial topologies. Phase correlations between CMB and foreground maps have been sought before (Naselsky, Doroshkevich & Verkhodanov, 2003; Chiang & Naselsky, 2004), however, here we wish to emphasise the virtue of having independent probes of Galactic foreground contamination.

In order to seek evidence of phase correlations between the RM map and CMB data, we turned to two WMAP–derived maps. Both maps’ construction are outlined in Section 3.3.4. The ultimate goal of these maps is to build an accurate image of the last scattering surface that captures the detailed morphology. We use the WMAP team’s internal linear combination (ILC) map and the Wiener–filtered map of Tegmark, de Oliveira-Costa & Hamilton (2003, TOH). The latter was chosen since the map was found to be correlated with RM values in chapter 5.

Two measures of phase association were used: the circular cross–correlation coefficient R and Kuiper’s statistic V . Both statistics will be evaluated at each scale l from 2 to 16. If we let Φ_{RM} and Φ_{CMB} be the phases of the RM and CMB maps, respectively. Then, following Fisher (1993), R is defined as:

$$R(l) = l^{-1} \sum_{m=1}^l \cos(\Phi_{m,\text{RM}} - \Phi_{m,\text{CMB}}). \quad (6.16)$$

The expectation value of R is 0, and hence highly correlated phases are associated with large values of $|R|$. Kuiper’s statistic is calculated from the available set of phase differences $(\Phi_{m,\text{RM}} - \Phi_{m,\text{CMB}})$ at a given scale. Kuiper’s statistic is comprehensively described in Section 3.2.1. First, the phase differences are sorted into ascending order, to give the set $\{\Theta_1, \dots, \Theta_p\}$. Each angle Θ_j is divided by 2π to give a set of variables X_j , where $j = 1 \dots p$. From the set of X_j we derive two values S_p^+ and S_p^- (see Equations (3.2) and (3.3)). Kuiper’s statistic is then defined as

$$V(l) = (S_p^+ + S_p^-) \cdot \left(\sqrt{p} + 0.155 + \frac{0.24}{\sqrt{p}} \right). \quad (6.17)$$

Again, the form of V is chosen so that it is approximately independent of sample size for large p . Anomalously large values of V indicate a distribution that is more

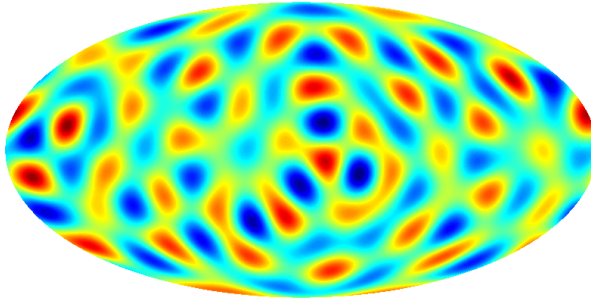


Figure 6.8: Internal linear combination map constructed with $a_{l,m}$ for $l=11$ only.

clumped than a uniformly random distribution, while low values mean that angles are more regular.

To access the significance of the values of R and V obtained from the comparison of the RM map with the two CMB maps, we make use of Monte Carlo skies with uniformly random phases. The statistics were calculated for 10,000 MC skies contrasted with a further 10,000 MC skies. Thus, we are left with 10,000 values of R and V for each scale.

The results from both CMB maps suggests that there is strong correlations between the phases at $l=11$. For the ILC, the values of $R(11)$ and $V(11)$ are greater than 99 percent of the MC values. Whereas, the values of $R(11)$ and $V(11)$ corresponding to the TOH Wiener–filtered map are greater than 97 and 98 percent of the MC skies, respectively. In Figure 6.8 we plot the ILC map constructed with the $a_{l,m}$ for $l=11$. Overlapping this image with that of the RM in Fig 6.4, we can see that the central maxima/minima pair in the RM map are similar in location, size and shape to structure in the ILC image (but with colours reversed). This is probably what determines the specific scale $l=11$. Interestingly, $l=11$ corresponds to the scale that Naselsky, Doroshkevich & Verkhodanov (2003) found the greatest level of correlation between the ILC phases and those of the foreground maps.

6.7 Conclusions

In this chapter, a new method was presented to generate all-sky RM maps from uneven and sparsely populated data samples. The method calculates a set of functions orthonormal to the data set. With these basis functions, the spherical harmonic coef-

ficients are calculated and converted into sky maps using the HEALPix package. The method was applied to three catalogues; S81, B88 and F01 catalogues. Maps from each catalogue showed evidence of the magnetic field in our local Orion spur, the North-South asymmetry attributed to radio Loop I and a maxima/minima pair close to the Galactic centre that possibly corresponds to the magnetic field of two inner Galactic arms. A RM map constructed from the S81 catalogue also had a prominent maxima at $l^{\text{II}} \sim 50^\circ$ in the northern hemisphere.

In Section 6.6, we showed the benefits a RM map has to CMB foreground analysis. Phase correlations were sought between RM maps and those of CMB-only maps derived from the WMAP data. For both the WMAP team's ILC map and the Wiener-filtered map of TOH, phases corresponding to $l=11$ were found to be highly correlated. Naselsky, Doroshkevich & Verkhodanov (2003) found the same scale to display phase correlations when carrying out a similar analysis on the ILC map and foreground maps. Their detection of correlations at the same scale as our analysis, reaffirms the conclusion drawn in chapter 5 that the RM catalogues are valuable independent tracers of CMB foregrounds.

Modelling foregrounds will play a crucial role in CMB polarisation studies. Foreground contamination is expected to be more severe than in the temperature measurements (Kosowsky, 1999). Consequently, superior templates for the individual foreground components are required. RM maps will help trace these components. Besides this, extrapolation of low frequency measurement of synchrotron polarisation to CMB frequencies has been shown to be complicated by Faraday rotation (de Oliveira-Costa *et al.*, 2003). Again, this underlines the importance of developing templates of the Faraday rotation of the Galactic sky. Efforts to map the RM sky will be greatly enhanced by increased source catalogues for both extragalactic sources and pulsars within our Galaxy. This may enable the formation of a 3-dimensional image of the Galactic magnetic field. Furthermore, attempts to map the RM sky will be enhanced by upcoming satellite CMB polarisation experiments which present unprecedented sky-coverage and resolution.

Chapter 7

Problems and future extensions

In this thesis, I have developed a number of diagnostics capable of identifying non-standard behaviour in the CMB temperature field. Chapters 2–4 focused on the development of a statistic that utilised the phase information of the spherical harmonic coefficients. The technique was found to compliment more traditional measures of non-Gaussianity. A rather simple and obvious extension to this work, is to apply the phase statistic to forthcoming 2nd-year WMAP data with a Galactic cut incorporated into the MC simulations. It will be interesting to see if the observed peculiar features seen in chapter 3 remain. Incorporating the Galactic cut will allow us to directly analyse the data set used to establish the key parameters. The individual frequency maps of WMAP are used in the computation of the angular power spectrum. The establishment of key cosmological parameters relies on Gaussian statistics to hold for this data.

Equally, it should be rewarding to use the phase technique to explore multipoles beyond $l=20$. Two factors inhibit this: Kuiper’s statistic is a general test that is suited to a small number of data points and secondly the computational time needed to generate the Wigner D -function significantly increases with increasing l . The first point may be tackled by the development of a more tailored statistic. In Section 2.3.3, we found phases were separated by $\pm\pi$ when forming particular band-shapes and structure in the southern hemisphere. It has been claimed that there is a North-South asymmetry in the WMAP data (eg. Eriksen *et al.*, 2004b). Is this type of phase coupling hinting at a method to use the phases to probe this? Clearly, it is vital to understand the origin of these phase correlations. Matsubara (2003) found a relation between the distribution of a specific form of associated phases and the hierarchy of polyspectra in the context

of structure formation. Finding links between the phase information and other traditional non-Gaussian measures such as the genus (which is also a valuable tracer of morphology) will allow us to get a better handle on the source of these correlations.

The second aspect requires advancements in the generation of the Wigner D -function. Alternatively, we could find a new method for rotating the coordinate frame. This may mean tailoring the method around the HEALPix pixelisation scheme. For example, we could create a grid of rotation vectors in real space that shuffle the pixels around. The problem is that we have to evenly sample the sphere. Uniformly rotating the sky along the polar angle ϕ is trivial, but due to the shape of the individual pixels, uniformly sampling the azimuthal angle θ is more challenging. Other pixelisation schemes may be more suited to rotating the sky in real-space.

The issue of studying high multipoles can be simply solved by taking a small patch of the sky and assuming the surface is flat. One can then work in the Fourier domain and make use of phase techniques already developed in the context of structure formation.

Beyond this, the phase analysis needs to be extended in such a way that we can probe more complex forms of phase correlations. A large-scale homogeneous primordial magnetic field would induce correlations between $a_{l-1,m}$ and $a_{l+1,m}$ at fixed m . Our current methods are not sensitive to this kind of correlation. It will also be enlightening to combine the phases with the amplitudes, in the spirit of Stannard & Coles (2004), to look for anomalies. Ultimately, it will be important to develop similar tools that can untangle phase information encoded in other classes of cosmic fields such as those seen in gravitational lensing studies.

One of the key questions that arose from the release of the WMAP data was the issue of the missing power at large scales. A possible explanation is that we inhabit a small universe. This was investigated in chapter 4. The issue of the topology of the universe is important in its own right. The standard concordance model places us in a universe with Euclidean geometry. If simply-connected, then the universe is infinite in size. Is it then sensible to make claims about the nature of an infinite universe from a finite observable patch? A more complete view of the universe would be offered by knowing its topology. Methods need to be developed that can explore beyond the limits of the circles in the sky method (Cornish, Spergel & Starkman, 1998). We have shown that the phases have the potential to do just that. However, we need to verify this by applying the method to more simulations. Coupled to this, we need to seek these

correlations in data where the issue of foreground contamination is less significant. Incorporating the Galactic cut into the MC simulations, as already suggested, will enable us to probe cleaner maps.

The significance of the absent power at large scales appears to depend on the analysis performed on the data. It has been claimed that the discrepancy from the concordance model is less statistically significant than originally thought (Efstathiou, 2003). Nevertheless, there is still mystery surrounding the planar nature of the low multipoles (see Section 3.3.4). Evidently, further investigation of these low multipoles is required and in particular their phases. It would be surprising if the phases were not a key component in forming the multipoles' planar shape. It has already been found that certain map-making-processes lead to a poor reconstruction of the cosmological phases (Eriksen *et al.*, 2004a).

The issue of foreground contamination of CMB data was touched upon during the work on the phase statistic. In chapter 5, we dealt with this issue in detail. We developed an independent tracer of the Galactic foregrounds from a catalogue of rotation measures of extragalactic radio sources. A better understanding of the frequency dependence of the correlations is required. Data from a wider frequency range will aid this. For example, the recent Archeops data (Tristram *et al.*, 2004) that covers 20% of the sky is compiled from frequency bands centered at 143 and 217 GHz. At these frequencies dust is the sole foreground contaminant. A comparison of the same sections of the sky from the WMAP data would give us a better handle on how the strength of the correlations varies with frequency for dust. This could aid in the separation of the contribution of the different components. Again, this may give us a helping hand in understanding the mechanism causing the anomalous emission at ~ 20 GHz.

In chapter 6, we developed a template of the RM sky. This is the first step in developing templates of the foreground components that incorporate information from rotation measures. Applying constraints on the electron density and Galactic magnetic field, it is conceivable that predictions can be made for the signals from the foreground components. Furthermore, the RM maps can be integrated into methods for generating CMB-only maps. For example, maximum entropy methods use templates of foreground components from outside frequencies to generate CMB-only maps. The RM map could be added as another constraint in the calculation of the CMB signal from such a method. Other potential uses for the RM map have already been listed in

chapter 6, although, it is worth pointing out that the orthogonalisation scheme could be used on other incomplete astronomical data sets.

Finally, on a more general note, high quality CMB–only maps will eventually be constructed due to decreases in instrument noise and better foreground control. One of the motivations for producing these CMB–only sky maps is to perform joint data analysis. Boughn & Crittenden (2004) show the importance of this type of analysis: they use CMB data and the X-ray background to show evidence of dark energy. Cross-correlating X-ray data, large-scale-structure data and the CMB, or the fusion of CMB data sets requires specific statistical analysis tools. Perhaps some of the statistics developed in this thesis can be applied when evaluating the detailed structure of these projected data sets. For example, studying the phase difference of the data sets should provide another method for performing joint analyse. After WMAP and Planck, it is likely that polarisation studies will provide the main emphasis in CMB physics. Although the detection and measurement of primordial polarisation (especially *B*-mode fluctuations) promises a wealth of cosmological information, this may be rendered impossible if there are complicated foreground polarisation patterns. The development of polarisation tools will be essential. The work on rotation measures could be used to make predictions of the polarisation signal from foreground sources. The phase studies can be extended from scalar temperature maps to maps of the polarisation which are vector fields.

Bibliography

- Adler R. J., 1981. *The Geometry of Random Fields*, Chichester: Wiley.
- Aghanim N., Forni O., 1999. *Astron. Astrophys.*, **347**, 409. *Searching for the non-Gaussian signature of the CMB secondary anisotropies*.
- Albrecht A., Steinhardt P. J., 1982. *Physical Review Letters*, **48**, 1220. *Cosmology for grand unified theories with radiatively induced symmetry breaking*.
- Banday A. J., Gorski K. M., Bennett C. L., Hinshaw G., Kogut A., Lineweaver C., Smoot G. F., Tenorio L., 1997. *Ap. J.*, **475**, 393. *Root Mean Square Anisotropy in the COBE DMR Four-Year Sky Maps*.
- Banday A. J., Dickinson C., Davies R. D., Davis R. J., Górska K. M., 2003. *MNRAS*, **345**, 897. *Reappraising foreground contamination in the COBE-DMR data*.
- Bardeen J. M., Bond J. R., Kaiser N., Szalay A. S., 1986. *Ap. J.*, **304**, 15. *The statistics of peaks of Gaussian random fields*.
- Barreiro R. B., 2000. *New Astronomy Review*, **44**, 179. *The cosmic microwave background State of the art*.
- Barrow J. D., Ferreira P. G., Silk J., 1997. *Phys. Rev. Lett.*, **78**, 3610. *Constraints on a Primordial Magnetic Field*.
- Bennett C. L., Kogut A., Hinshaw G., Banday A. J., Wright E. L., Gorski K. M., Wilkinson D. T., Weiss R., Smoot G. F., Meyer S. S., Mather J. C., Lubin P., Loewenstein K., Lineweaver C., Keegstra P., Kaita E., Jackson P. D., Cheng E. S., 1994. *Ap. J.*, **436**, 423. *Cosmic temperature fluctuations from two years of COBE differential microwave radiometers observations*.
- Bennett C. L., Halpern M., Hinshaw G., Jarosik N., Kogut A., Limon M., Meyer S. S., Page L., Spergel D. N., Tucker G. S., Wollack E., Wright E. L., Barnes C., Greason M. R., Hill R. S., Komatsu E., Nolta M. R., Odegard N., Peiris H. V., Verde L., Weiland J. L., 2003a. *Ap. J. Suppl.*, **148**, 1. *First-Year Wilkinson Microwave Anisotropy Probe (WMAP) Observations: Preliminary Maps and Basic Results*.

- Bennett C. L., Hill R. S., Hinshaw G., Nolta M. R., Odegard N., Page L., Spergel D. N., Weiland J. L., Wright E. L., Halpern M., Jarosik N., Kogut A., Limon M., Meyer S. S., Tucker G. S., Wollack E., 2003b. *Ap. J. Suppl.*, **148**, 97. *First-Year Wilkinson Microwave Anisotropy Probe (WMAP) Observations: Foreground Emission.*
- Bond J. R., Efstathiou G., 1987. *MNRAS*, **226**, 655. *The statistics of cosmic background radiation fluctuations.*
- Boughn S., Crittenden R., 2004. *Nature*, **427**, 45. *A correlation between the cosmic microwave background and large-scale structure in the Universe.*
- Bromley B. C., Tegmark M., 1999. *Ap. J. Lett.*, **524**, L79. *Is the Cosmic Microwave Background Really Non-Gaussian?*
- Broten N. W., MacLeod J. M., Vallee J. P., 1988. *Astrophys. Space Sci.*, **141**, 303. *Catalogue of unambiguous (Faraday-thin, one-component, spectrum-selected) rotation measures for galaxies and quasars.*
- Burles S., Nollett K. M., Turner M. S., 2001. *Ap. J. Lett.*, **552**, L1. *Big Bang Nucleosynthesis Predictions for Precision Cosmology.*
- Chen G., Mukherjee P., Kahnashvili T., Ratra B., Wang Y., 2004. *Ap. J.*, **611**, 655. *Looking for Cosmological Alfvén Waves in Wilkinson Microwave Anisotropy Probe Data.*
- Chiang L., Coles P., 2000. *MNRAS*, **311**, 809. *Phase information and the evolution of cosmological density perturbations.*
- Chiang L.-Y., Naselsky P. D., 2004. preprint (*astro-ph/0407395*). *Auto and cross correlation of phases of the whole-sky CMB and foreground maps from the 1-year WMAP data.*
- Chiang L., Coles P., Naselsky P., 2002. *MNRAS*, **337**, 488. *Return mapping of phases and the analysis of the gravitational clustering hierarchy.*
- Chiang L., Naselsky P. D., Verkhodanov O. V., Way M. J., 2003. *Ap. J. Lett.*, **590**, L65. *Non-Gaussianity of the Derived Maps from the First-Year Wilkinson Microwave Anisotropy Probe Data.*
- Chiang L., 2001. *MNRAS*, **325**, 405. *The importance of Fourier phases for the morphology of gravitational clustering.*
- Coles P., Chiang L., 2000. *Nature*, **406**, 376. *Characterizing the nonlinear growth of large-scale structure in the Universe.*
- Coles P., Dineen P., Earl J., Wright D., 2004. *MNRAS*, **350**, 989. *Phase correlations in cosmic microwave background temperature maps.*

- Coles P., 1988. *MNRAS*, **234**, 509. *Statistical geometry and the microwave background.*
- Cornish N. J., Spergel D. N., Starkman G. D., Komatsu E., 2004. *Physical Review Letters*, **92(20)**, 201302. *Constraining the Topology of the Universe.*
- Cornish N. J., Spergel D. N., Starkman G. D., 1998. *Class. Quant. Grav.*, **15**, 2657. *Circles in the sky: finding topology with the microwave background radiation .*
- Davies R., Wilkinson A., 1998. *Synchrotron Emission from the Galaxy*, In: *J.Tran Thanh Van, Y.Giraoud-Heraud, F. Bouchet, T. Damour & Y.Mellier (Eds.)*, *Fundamental Parameters in Cosmology, Proc. of the XXXIIIrd Rencontres de Moriond*, *Editions Frontieres*, p. 175.
- Davies R. D., Watson R. A., Gutierrez C. M., 1996. *MNRAS*, **278**, 925. *Galactic synchrotron emission at high frequencies.*
- de Oliveira-Costa A., Tegmark M., Gutierrez C. M., Jones A. W., Davies R. D., Lasenby A. N., Rebolo R., Watson R. A., 1999. *Ap. J. Lett.*, **527**, L9. *Cross-Correlation of Tenerife Data with Galactic Templates-Evidence for Spinning Dust?*
- de Oliveira-Costa A., Tegmark M., O'dell C., Keating B., Timbie P., Efstathiou G., Smoot G., 2003. *Phys. Rev. D*, **68(8)**, 083003. *Large-scale polarization of the microwave background and foreground.*
- de Oliveira-Costa A., Tegmark M., Davies R. D., Gutiérrez C. M., Lasenby A. N., Rebolo R., Watson R. A., 2004a. *Ap. J. Lett.*, **606**, L89. *The Quest for Microwave Foreground X.*
- de Oliveira-Costa A., Tegmark M., Zaldarriaga M., Hamilton A., 2004b. *Phys. Rev. D*, **69(6)**, 063516. *Significance of the largest scale CMB fluctuations in WMAP.*
- de Oliveira-Costa A., 2004. preprint (*astro-ph/0406358*). *The Cosmic Microwave Background and Its Polarization.*
- Dekel A., West M. J., 1985. *Ap. J.*, **288**, 411. *On percolation as a cosmological test.*
- Dineen P., Coles P., 2004a. *MNRAS*, **347**, 52. *Faraday rotation as a diagnostic of Galactic foreground contamination of cosmic microwave background maps.*
- Dineen P., Coles P., 2004b. preprint (*astro-ph/0410636*). *A Faraday Rotation Template for the Galactic Sky.*
- Dineen P., Rocha G., Coles P., 2004. preprint (*astro-ph/0404356*). *Non-Random Phases in Non-Trivial Topologies.*
- Draine B. T., Lazarian A., 1998. *Ap. J. Lett.*, **494**, L19. *Diffuse Galactic Emission from Spinning Dust Grains.*

- Edmonds A., 1960. *Quantum theory of angular momentum*, Princeton: Princeton University Press.
- Edwards M. O., 1989. *Global gridded elevation and bathymetry on 5-minute geographic grid, (ETOPO5)*, NOAA National Geophysical Data Center, Boulder, Colorado, USA.
- Efstathiou G., 2003. *MNRAS*, **346**, L26. *The statistical significance of the low cosmic microwave background multipoles*.
- Eriksen H. K., Banday A. J., Górski K. M., Lilje P. B., 2004a. *Ap. J.*, **612**, 633. *On Foreground Removal from the Wilkinson Microwave Anisotropy Probe Data by an Internal Linear Combination Method: Limitations and Implications*.
- Eriksen H. K., Hansen F. K., Banday A. J., Gorski K. M., Lilje P. B., 2004b. *Ap. J.*, **605**, 14. *Asymmetries in the Cosmic Microwave Background Anisotropy Field*.
- Ferreira P. G., Magueijo J., 1997a. *Phys. Rev. D*, **55**, 3358. *Non-Gaussian spectra in cosmic microwave background temperature anisotropies*.
- Ferreira P. G., Magueijo J., 1997b. *Phys. Rev. D*, **56**, 4578. *Closest non-Gaussianity of anisotropic Gaussian fluctuations*.
- Ferreira P. G., Magueijo J., Gorski K. M., 1998. *Ap. J. Lett.*, **503**, L1. *Evidence for Non-Gaussianity in the COBE DMR 4 Year Sky Maps*.
- Finkbeiner D. P., Davis M., Schlegel D. J., 1999. *Ap. J.*, **524**, 867. *Extrapolation of Galactic Dust Emission at 100 Microns to Cosmic Microwave Background Radiation Frequencies Using FIRAS*.
- Finkbeiner D. P., 2003. *Ap. J. Suppl.*, **146**, 407. *A Full-Sky H α Template for Microwave Foreground Prediction*.
- Fisher N. I., 1993. *Statistical Analysis of Circular Data*, Cambridge: Cambridge University Press.
- Fixsen D. J., Cheng E. S., Gales J. M., Mather J. C., Shafer R. A., Wright E. L., 1996. *Ap. J.*, **473**, 576. *The Cosmic Microwave Background Spectrum from the Full COBE FIRAS Data Set*.
- Freedman W. L., Madore B. F., Gibson B. K., Ferrarese L., Kelson D. D., Sakai S., Mould J. R., Kennicutt R. C., Ford H. C., Graham J. A., Huchra J. P., Hughes S. M. G., Illingworth G. D., Macri L. M., Stetson P. B., 2001. *Ap. J.*, **553**, 47. *Final Results from the Hubble Space Telescope Key Project to Measure the Hubble Constant*.
- Frick P., Stepanov R., Shukurov A., Sokoloff D., 2001. *MNRAS*, **325**, 649. *Structures in the rotation measure sky*.

- Gamow G., 1948. *Phys. Rev.*, **74**, 505. *The Origin of Elements and the Separation of Galaxies*.
- Gawiser E., Silk J., 2000. *Phys. Rep.*, **333**, 245. *The cosmic microwave background radiation*.
- Gorski K. M., Hivon E., Wandelt B., 1999. *Analysis issues for large CMB data sets*, In: *Evolution of Large Scale Structure : From Recombination to Garching*, p. 37.
- Gorski K. M., 1994. *Ap. J. Lett.*, **430**, L85. *On determining the spectrum of primordial inhomogeneity from the COBE DMR sky maps: Method*.
- Gott J. R., Dickinson M., Melott A. L., 1986. *Ap. J.*, **306**, 341. *The sponge-like topology of large-scale structure in the universe*.
- Gott J. R. I., Park C., Juszkiewicz R., Bies W. E., Bennett D. P., Bouchet F. R., Stebbins A., 1990. *Ap. J.*, **352**, 1. *Topology of microwave background fluctuations - Theory*.
- Guth A. H., Pi S.-Y., 1982. *Physical Review Letters*, **49**, 1110. *Fluctuations in the new inflationary universe*.
- Guth A. H., 1981. *Phys. Rev. D*, **23**, 347. *Inflationary universe: A possible solution to the horizon and flatness problems*.
- Han J. L., Manchester R. N., Berkhuijsen E. M., Beck R., 1997. *Astron. Astrophys.*, **322**, 98. *Antisymmetric rotation measures in our Galaxy: evidence for an A0 dynamo*.
- Han J. L., 2004. *The Large-Scale Magnetic Field Structure of Our Galaxy: Efficiently Deduced from Pulsar Rotation Measures*, In: *The Magnetized Interstellar Medium*, p. 3.
- Hansen F. K., Marinucci D., Vittorio N., 2003. *Phys. Rev. D*, **67(12)**, 123004. *Extended empirical process test for non-Gaussianity in the CMB, with an application to non-Gaussian inflationary models*.
- Haslam C. G. T., Stoffel H., Salter C. J., Wilson W. E., 1982. *Astron. Astrophys. Suppl.*, **47**, 1. *A 408 MHz all-sky continuum survey. II - The atlas of contour maps*.
- Hawking S. W., 1982. *Physics Letters B*, **115**, 295. *The development of irregularities in a single bubble inflationary universe*.
- Heavens A. F., 1998. *MNRAS*, **299**, 805. *Estimating non-Gaussianity in the microwave background*.
- Hikage C., Matsubara T., Suto Y., 2004. *Ap. J.*, **600**, 553. *The Distribution Function of the Phase Sum as a Signature of Phase Correlations Induced by Nonlinear Gravitational Clustering*.

- Hinshaw G., Spergel D. N., Verde L., Hill R. S., Meyer S. S., Barnes C., Bennett C. L., Halpern M., Jarosik N., Kogut A., Komatsu E., Limon M., Page L., Tucker G. S., Weiland J. L., Wollack E., Wright E. L., 2003. *Ap. J. Suppl.*, **148**, 135. *First-Year Wilkinson Microwave Anisotropy Probe (WMAP) Observations: The Angular Power Spectrum.*
- Hobson M. P., Jones A. W., Lasenby A. N., 1999. *MNRAS*, **309**, 125. *Wavelet analysis and the detection of non-Gaussianity in the cosmic microwave background.*
- Hu W., Dodelson S., 2002. *Ann. Rev. Astron. Astrophys.*, **40**, 171. *Cosmic Microwave Background Anisotropies.*
- Hu W., White M., 1997. *New Astronomy*, **2**, 323. *A CMB polarization primer.*
- Inoue K. T., Sugiyama N., 2003. *Phys. Rev. D*, **67(4)**, 043003. *How large is our Universe?*
- Jain B., Bertschinger E., 1996. *Ap. J.*, **456**, 43. *Self-similar Evolution of Gravitational Clustering: Is $N = -1$ Special?*
- Jain B., Bertschinger E., 1998. *Ap. J.*, **509**, 517. *Self-Similar Evolution of Gravitational Clustering. II. N-Body Simulations of the $N = -2$ Spectrum.*
- Kibble T. W. B., 1976. *J. Phys.*, **A9**, 1387. *Topology of cosmic domains and strings.*
- Kim K.-T., Tribble P. C., Kronberg P. P., 1991. *Ap. J.*, **379**, 80. *Detection of excess rotation measure due to intracluster magnetic fields in clusters of galaxies.*
- Knop R. A., Aldering G., Amanullah R., Astier P., Blanc G., Burns M. S., Conley A., Deustua S. E., Doi M., Ellis R., Fabbro S., Folatelli G., Fruchter A. S., Garavini G., Garmond S., Garton K., Gibbons R., Goldhaber G., Goobar A., Groom D. E., Hardin D., Hook I., Howell D. A., Kim A. G., Lee B. C., Lidman C., Mendez J., Nobili S., Nugent P. E., Pain R., Panagia N., Pennypacker C. R., Perlmutter S., Quimby R., Raux J., Regnault N., Ruiz-Lapuente P., Sainton G., Schaefer B., Schahmaneche K., Smith E., Spadafora A. L., Stanishev V., Sullivan M., Walton N. A., Wang L., Wood-Vasey W. M., Yasuda N., 2003. *Ap. J.*, **598**, 102. *New Constraints on Ω_m , Ω_λ and w from an Independent Set of 11 High-Redshift Supernovae Observed with the Hubble Space Telescope.*
- Kogut A., Banday A. J., Bennett C. L., Gorski K. M., Hinshaw G., Smoot G. F., Wright E. L., 1996. *Ap. J. Lett.*, **464**, L29. *Tests for Non-Gaussian Statistics in the DMR Four-Year Sky Maps.*
- Kogut A., Spergel D. N., Barnes C., Bennett C. L., Halpern M., Hinshaw G., Jarosik N., Limon M., Meyer S. S., Page L., Tucker G. S., Wollack E., Wright E. L., 2003. *Ap. J. Suppl.*, **148**, 161. *First-Year Wilkinson Microwave Anisotropy Probe (WMAP) Observations: Temperature-Polarization Correlation.*

- Kosowsky A., Loeb A., 1996. *Ap. J.*, **469**, 1. *Faraday Rotation of Microwave Background Polarization by a Primordial Magnetic Field.*
- Kosowsky A., 1999. *New Astronomy Review*, **43**, 157. *Introduction to microwave background polarization.*
- Kovac J. M., Leitch E. M., Pryke C., Carlstrom J. E., Halverson N. W., Holzapfel W. L., 2002. *Nature*, **420**, 772. *Detection of polarization in the cosmic microwave background using DASI.*
- Kronberg P. P., Perry J. J., Zukowski E. L. H., 1992. *Ap. J.*, **387**, 528. *Discovery of extended Faraday rotation compatible with spiral structure in an intervening galaxy at Z = 0.395 - New observations of PKS 1229 - 021.*
- Kuiper N., 1960. *Proceedings of the Koninklijke Nederlandse Akademie Van Wetenschappen Series A*, **63**, 38. *Tests concerning random points on a circle.*
- Land K., Magueijo J., 2004. preprint (*astro-ph/0405519*). *Cubic anomalies in WMAP.*
- Lawson K. D., Mayer C. J., Osborne J. L., Parkinson M. L., 1987. *MNRAS*, **225**, 307. *Variations in the Spectral Index of the Galactic Radio Continuum Emission in the Northern Hemisphere.*
- Levin J., Scannapieco E., Silk J., 1998. *Phys. Rev. D*, **58(10)**, 103516. *Is the Universe infinite or is it just really big?*
- Lewin A., Albrecht A., Magueijo J., 1999. *MNRAS*, **302**, 131. *A new statistic for picking out non-Gaussianity in the CMB.*
- Lewis A., 2004. *Phys. Rev. D*, **70(4)**, 043011. *CMB anisotropies from primordial inhomogeneous magnetic fields.*
- Liguori M., Matarrese S., Moscardini L., 2003. *Ap. J.*, **597**, 57. *High-Resolution Simulations of Non-Gaussian Cosmic Microwave Background Maps in Spherical Coordinates.*
- Linde A. D., 1982. *Physics Letters B*, **108**, 389. *A new inflationary universe scenario: A possible solution of the horizon, flatness, homogeneity, isotropy and primordial monopole problems.*
- Luminet J., Roukema B. F., 1999. *Topology of the Universe: Theory and Observation*, In: *NATO ASIC Proc. 541: Theoretical and Observational Cosmology*, p. 117.
- Luminet J., Weeks J. R., Riazuelo A., Lehoucq R., Uzan J., 2003. *Nature*, **425**, 593. *Dodecahedral space topology as an explanation for weak wide-angle temperature correlations in the cosmic microwave background.*
- Luo X., Schramm D. N., 1993a. *Ap. J.*, **408**, 33. *Kurtosis, skewness, and non-Gaussian cosmological density perturbations.*

- Luo X., Schramm D. N., 1993b. *Phys. Rev. Lett.*, **71**, 1124. *Testing for the Gaussian nature of cosmological density perturbations through the three-point temperature correlation function.*
- Luo X., 1994. *Ap. J. Lett.*, **427**, L71. *The angular bispectrum of the cosmic microwave background.*
- Matsubara T., 2003. *Ap. J. Lett.*, **591**, L79. *Phase Correlations in Non-Gaussian Fields.*
- McEwen J., Hobson M., Lasenby A., Mortlock D., 2004. preprint (*astro-ph/0406604*). *A 6 sigma detection of non-Gaussianity in the WMAP 1-year data using directional spherical wavelets.*
- Mecke K. R., Buchert T., Wagner H., 1994. *Astron. Astrophys.*, **288**, 697. *Robust morphological measures for large-scale structure in the Universe.*
- Naselsky P. D., Doroshkevich A. G., Verkhodanov O. V., 2003. *Ap. J. Lett.*, **599**, L53. *Phase Cross-Correlation of the Wilkinson Microwave Anisotropy Probe Internal Linear Combination Map and Foregrounds.*
- Naselsky P. D., Verkhodanov O. V., Chiang L.-Y., Novikov I. D., 2003. preprint (*astro-ph/0310235*). *Phase analysis of the 1-year WMAP data and its application for the CMB foreground separation.*
- Naselsky P. D., Chiang L.-Y., Olesen P., Verkhodanov O. V., 2004. preprint (*astro-ph/0405181*). *Primordial magnetic field and non-Gaussianity of the 1-year Wilkinson Microwave Anisotropy Probe (WMAP) data.*
- Ostriker J. P., Cowie L. L., 1981. *Ap. J. Lett.*, **243**, L127. *Galaxy formation in an intergalactic medium dominated by explosions.*
- Pando J., Valls-Gabaud D., Fang L. Z., 1998. *Phys. Rev. Lett.*, **81**, 4568. *Evidence for scale-scale correlations in the cosmic microwave background radiation.*
- Peebles P. J. E., 1980. *The large-scale structure of the universe*, Princeton: Princeton University Press.
- Penzias A. A., Wilson R. W., 1965. *Ap. J.*, **142**, 419. *A Measurement of Excess Antenna Temperature at 4080 Mc/s.*
- Percival W. J., Baugh C. M., Bland-Hawthorn J., Bridges T., Cannon R., Cole S., Colless M., Collins C., Couch W., Dalton G., De Propris R., Driver S. P., Efstathiou G., Ellis R. S., Frenk C. S., Glazebrook K., Jackson C., Lahav O., Lewis I., Lumsden S., Maddox S., Moody S., Norberg P., Peacock J. A., Peterson B. A., Sutherland W., Taylor K., 2001. *MNRAS*, **327**, 1297. *The 2dF Galaxy Redshift Survey: the power spectrum and the matter content of the Universe.*

- Perlmutter S., Aldering G., Goldhaber G., Knop R. A., Nugent P., Castro P. G., Deustua S., Fabbro S., Goobar A., Groom D. E., Hook I. M., Kim A. G., Kim M. Y., Lee J. C., Nunes N. J., Pain R., Pennypacker C. R., Quimby R., Lidman C., Ellis R. S., Irwin M., McMahon R. G., Ruiz-Lapuente P., Walton N., Schaefer B., Boyle B. J., Filippenko A. V., Matheson T., Fruchter A. S., Panagia N., Newberg H. J. M., Couch W. J., The Supernova Cosmology Project, 1999. *Ap. J.*, **517**, 565. *Measurements of Omega and Lambda from 42 High-Redshift Supernovae.*
- Phillips N. G., Kogut A., 2004. preprint (*astro-ph/0404400*). *Constraints On The Topology Of The Universe From The WMAP First-Year Sky Maps.*
- Riazuelo A., Uzan J., Lehoucq R., Weeks J., 2004. *Phys. Rev. D*, **69(10)**, 103514. *Simulating cosmic microwave background maps in multiconnected spaces.*
- Rocha G., Cayón L., Bowen R., Canavezes A., Silk J., Banday A. J., Górski K. M., 2004. *MNRAS*, **351**, 769. *Topology of the Universe from COBE-DMR - a wavelet approach.*
- Roukema B. F., Lew B., Cechowska M., Marecki A., Bajtlik S., 2004. *Astron. Astrophys.*, **423**, 821. *A hint of Poincaré dodecahedral topology in the WMAP first year sky map.*
- Ruzmaikin A. A., Sokoloff D. D., 1979. *Astron. Astrophys.*, **78**, 1. *The calculation of Faraday rotation measures of cosmic radio sources.*
- Ruzmaikin A. A., Sokolov D. D., 1977. *Astron. Astrophys.*, **58**, 247. *The interpretation of rotation measures of extragalactic radio sources.*
- Ryden B. S., Gramann M., 1991. *Ap. J. Lett.*, **383**, L33. *Phase shifts in gravitationally evolving density fields.*
- Sachs R. K., Wolfe A. M., 1967. *Ap. J.*, **147**, 73. *Perturbations of a Cosmological Model and Angular Variations of the Microwave Background.*
- Sazhin M., Sironi G., Khovanskaya O., 2002. preprint (*astro-ph/0209400*). *Galactic Synchrotron Foreground and the CMB Polarization Measurements.*
- Scannapieco E. S., Ferreira P. G., 1997. *Phys. Rev. D*, **56**, 7493. *Polarization-temperature correlation from a primordial magnetic field.*
- Scherrer R. J., Melott A. L., Shandarin S. F., 1991. *Ap. J.*, **377**, 29. *A quantitative measure of phase correlations in density fields.*
- Schmalzing J., Gorski K. M., 1998. *MNRAS*, **297**, 355. *Minkowski functionals used in the morphological analysis of cosmic microwave background anisotropy maps.*
- Schwarzschild K., 1900. *Vierteljahrsschrift der Ast. Ges.*, **35**, 337. *On the permissible curvature of space.*

- Scoccola C., Harari D., Mollerach S., 2004. preprint (*astro-ph/0405396*). *B polarization of the CMB from Faraday rotation.*
- Seymour P. A. H., 1966. *MNRAS*, **134**, 389. *Models of the galactic magnetic field.*
- Seymour P. A. H., 1984. *Quar. J. R. astr. Soc.*, **25**, 293. *Faraday Rotation and the Galactic Magnetic Field - a Review.*
- Silk J., 1968. *Ap. J.*, **151**, 459. *Cosmic Black-Body Radiation and Galaxy Formation.*
- Simard-Normandin M., Kronberg P. P., Button S., 1981. *Ap. J. Suppl.*, **45**, 97. *The Faraday rotation measures of extragalactic radio sources.*
- Smoot G. F., Bennett C. L., Kogut A., Wright E. L., Aymon J., Boggess N. W., Cheng E. S., de Amici G., Gulkis S., Hauser M. G., Hinshaw G., Jackson P. D., Janssen M., Kaita E., Kelsall T., Keegstra P., Lineweaver C., Loewenstein K., Lubin P., Mather J., Meyer S. S., Moseley S. H., Murdock T., Rokke L., Silverberg R. F., Tenorio L., Weiss R., Wilkinson D. T., 1992. *Ap. J. Lett.*, **396**, L1. *Structure in the COBE differential microwave radiometer first-year maps.*
- Smoot G. F., Gorenstein M. V., Muller R. A., 1977. *Phys. Rev. Lett.*, **39**, 898. *Detection of anisotropy in the cosmic blackbody radiation.*
- Soda J., Suto Y., 1992. *Ap. J.*, **396**, 379. *Nonlinear gravitational evolution of phases and amplitudes in one-dimensional cosmological density fields.*
- Sofue Y., Fujimoto M., 1983. *Ap. J.*, **265**, 722. *A bisymmetric spiral magnetic field and the spiral arms in our Galaxy.*
- Spergel D. N., Verde L., Peiris H. V., Komatsu E., Nolta M. R., Bennett C. L., Halpern M., Hinshaw G., Jarosik N., Kogut A., Limon M., Meyer S. S., Page L., Tucker G. S., Weiland J. L., Wollack E., Wright E. L., 2003. *Ap. J. Suppl.*, **148**, 175. *First-Year Wilkinson Microwave Anisotropy Probe (WMAP) Observations: Determination of Cosmological Parameters.*
- Stannard A., Coles P., 2004. preprint (*astro-ph/0410633*). *Random-Walk Statistics and the Spherical Harmonic Representation of CMB Maps.*
- Starobinsky A. A., 1982. *Physics Letters B*, **117**, 175. *Dynamics of phase transition in the new inflationary universe scenario and generation of perturbations.*
- Sugino T., Suto Y., 1991. *Ap. J.*, **371**, 470. *Statistics of peaks in cosmological nonlinear density fields.*
- Sunyaev R. A., Zeldovich Y. B., 1970. *Astrophys. Space Sci.*, **7**, 3. *Small-Scale Fluctuations of Relic Radiation.*
- Tegmark M., de Oliveira-Costa A., Hamilton A. J., 2003. *Phys. Rev. D*, **68(12)**, 123523. *High resolution foreground cleaned CMB map from WMAP.*

- Tristram M., et al., 2004. preprint (*astro-ph/0411633*). *The CMB temperature power spectrum from an improved analysis of the Archeops data.*
- Uzan J.-P., Riazuelo A., Lehoucq R., Weeks J., 2003. preprint (*astro-ph/0303580*). *Cosmic microwave background constraints on multi-connected spherical spaces.*
- Vallee J. P., Kronberg P. P., 1975. *Astron. Astrophys.*, **43**, 233. *The rotation measures of radio sources and their interpretation.*
- Vallee J. P., 1997. *Fundamentals of Cosmic Physics*, **19**, 1. *Observations of the Magnetic Fields Inside and Outside the Milky Way, Starting with Globules (~1 parsec), Filaments, Clouds, Superbubbles, Spiral Arms, Galaxies, Superclusters, and Ending with the Cosmological Universe's Background Surface (at ~8 Teraparsecs).*
- Varshalovich D., Moskalev A., Khersonskii V., 1988. *Quantum theory of angular momentum*, Singapore: World Scientific.
- Vilenkin A., Shellard E. P. S., 1994. *Cosmic strings and other topological defects*, Cambridge: Cambridge University Press.
- Vittorio N., Juszkiewicz R., 1987. *Ap. J. Lett.*, **314**, L29. *Hot spots in the microwave sky.*
- Wasserman I., 1978. *Ap. J.*, **224**, 337. *On the origins of galaxies, galactic angular momenta, and galactic magnetic fields.*
- Watts P., Coles P., 2003. *MNRAS*, **338**, 806. *Statistical cosmology with quadratic density fields.*
- Watts P., Coles P., Melott A., 2003. *Ap. J. Lett.*, **589**, L61. *The Universal Behavior of Phase Correlations in Nonlinear Gravitational Clustering.*
- Weeks J., Luminet J.-P., Riazuelo A., Lehoucq R., 2004. *MNRAS*, **352**, 258. *Well-proportioned universes suppress the cosmic microwave background quadrupole.*
- White S. D. M., 1979. *MNRAS*, **186**, 145. *The hierarchy of correlation functions and its relation to other measures of galaxy clustering.*
- Widrow L. M., 2002. *Reviews of Modern Physics*, **74**, 775. *Origin of galactic and extragalactic magnetic fields.*
- Winitzki S., Kosowsky A., 1998. *New Astronomy*, **3**, 75. *Minkowski functional description of microwave background Gaussianity.*
- Wolfe A. M., Lanzetta K. M., Oren A. L., 1992. *Ap. J.*, **388**, 17. *Magnetic fields in damped Ly-alpha systems.*
- Wright D., Earl J., 2002. MSci Project Report. *Phase correlations in the CMB.*

Acknowledgements

The bulk of chapter 3 is published in Coles, Dineen, Earl & Wright (2004). Chapter 4 is based around Dineen, Rocha & Coles (2004) which has recently been accepted for publication. Chapter 5 is based on the published article – Dineen & Coles (2004a). Finally, chapter 6 is based on Dineen & Coles (2004b) which has been submitted to *MNRAS*.

I thank my supervisor, Peter Coles, for his guidance and supervision over the course of my studies. Also, I thank Graca Rocha for her collaboration in the work contained in chapter 4. Dr Rocha provided the simulations of the universes with non-trivial topologies. In chapter 3, the spherical harmonic coefficients for the COBE–DMR 4–year data were provided by Joao Magueijo and Michele Liguori provided the non-Gaussian simulations. Tony Banday supplied me with the COBE–DMR data and Haslam map used in chapter 5. I thank Anvar Shukurov and Rodion Stepanov for supplying me with the rotation measure catalogues used in chapters 5 and 6.

In the early part of my PhD, I was aided by helpful comments provided by Ed Hawkins, Rob Smith and Pete Watts. Simon Coggins and Phil Couch solved numerous computational problems for me. Recently, I have been assisted by useful comments made by Arfon Smith and Laura Whyte during my write-up. The astronomy group in Nottingham has been a great environment to carry out my research and I have benefited from help from all the members of the group. Finally, it goes without saying, I am grateful to the support of all my family and friends.